

TANDEM SOLAR CELLS DEPOSITED USING HOT-WIRE CHEMICAL VAPOR DEPOSITION

Cover:

Cross sectional transmission electron microscopy (X-TEM) micrographs of two *n-i-p* structured solar cells, based on figures 4.4 and 6.10(b) of this thesis.

CIP-GEGEVENS KONINKLIJKE BIBLIOTHEEK, DEN HAAG

Veen, Marieke Katherine van

Tandem Solar Cells deposited using Hot-Wire Chemical Vapor Deposition
(Tandemzonnecellen gedeponerd via gasontleding aan een heet filament)/

Marieke Katherine van Veen - Utrecht: Universiteit Utrecht,

Faculteit Natuur- en Sterrenkunde, Debye Instituut

Proefschrift Universiteit Utrecht. Met samenvatting in het Nederlands.

ISBN 90-393-3336-X

TANDEM SOLAR CELLS DEPOSITED USING
HOT-WIRE CHEMICAL VAPOR DEPOSITION

TANDEMZONNECELLEN GEDEPONEERD VIA
GASONTLEDING AAN EEN HEET FILAMENT

(met een samenvatting in het Nederlands)

PROEFSCHRIFT

ter verkrijging van de graad van doctor aan de Universiteit Utrecht
op gezag van de Rector Magnificus, prof. dr. W. H. Gispen,
ingevolge het besluit van het College voor Promoties in het open-
baar te verdedigen op woensdag 28 mei 2003 des middags te 2.30
uur

door

MARIEKE KATHERINE VAN VEEN

geboren op 25 augustus 1976, te Vught

Promotor: prof. dr. R. E. I. Schropp

Faculteit Natuur- en Sterrenkunde
Universiteit Utrecht

The work presented in this thesis was made possible by financial support from the “Netherlands Agency for Energy and the Environment” (NOVEM).

Contents

1	Introduction	9
1.1	Solar energy	9
1.2	Hydrogenated amorphous silicon	10
1.3	Polycrystalline and microcrystalline silicon	12
1.4	Thin-film silicon solar cells	13
1.5	Plasma-enhanced chemical vapor deposition	17
1.6	Hot-wire chemical vapor deposition	18
1.7	Previous work	19
1.8	Aim of this work	21
1.9	Outline of this thesis	21
2	Experimental techniques	23
2.1	Hot-wire chemical vapor deposition	23
2.2	Deposition equipment	24
2.3	Material characterization techniques	26
2.3.1	Optical and electrical measurements	26
2.3.2	Structural measurements	32
2.4	Solar cell characterization	36
2.4.1	Current-voltage measurements	36
2.4.2	Spectral response measurements	40
2.4.3	Degradation of solar cells	42
3	Hot-wire deposited intrinsic amorphous silicon	45
3.1	Introduction	45
3.2	Influence of the substrate temperature	46
3.2.1	Role of hydrogen	48
3.2.2	Filament aging	50
3.2.3	Epitaxial growth	51
3.3	Influence of silicide formation	53
3.4	Deposition pressure	56
3.5	Hydrogen dilution	60
3.6	Deposition rate and bandgap variation	60
3.7	Conclusions	61

4	Amorphous silicon solar cells	63
4.1	Introduction	63
4.2	<i>n-i-p</i> structured solar cells	64
4.2.1	Experimental details	64
4.2.2	Results and discussion	66
4.3	<i>p-i-n</i> structured solar cells	71
4.3.1	Experimental details	71
4.3.2	Results and discussion	72
4.4	Conclusions	75
5	Shunting of hot-wire deposited amorphous silicon solar cells	77
5.1	Introduction	77
5.2	Experimental details	77
5.3	Results and discussion	79
5.4	Conclusions	84
6	Polycrystalline and microcrystalline silicon	85
6.1	Introduction	85
6.2	Polycrystalline silicon	86
6.3	Microcrystalline silicon	87
6.3.1	Experimental details	87
6.3.2	Results and discussion	89
6.3.3	Solar cells	93
6.3.4	Microstructure	95
6.3.5	Thickness dependence	99
6.4	Conclusions	101
7	Hot-wire deposited <i>n</i>-doped microcrystalline silicon	103
7.1	Introduction	103
7.2	Experimental details	104
7.3	Results and discussion	105
7.4	Influence on plasma-enhanced deposition	111
7.5	Conclusions	112
8	Tandem solar cells	115
8.1	Introduction	115
8.2	Experimental details	116
8.3	Results and discussion	117
8.3.1	<i>a</i> -Si:H/poly-Si tandem solar cells	118
8.3.2	<i>a</i> -Si:H/ <i>a</i> -Si:H tandem solar cells	122
8.3.3	<i>a</i> -Si:H/ μ c-Si:H tandem solar cells	123

8.3.4	<i>a</i> -Si:H/ μ c-Si:H/ μ c-Si:H triple solar cells	125
8.3.5	Tandem solar cells with <i>p-i-n/p-i-n</i> structure	129
8.4	Conclusions	133
9	General conclusions and perspectives	135
	References	137
	Summary	145
	Samenvatting	149
	List of publications	155
	Dankwoord	157
	Curriculum Vitae	159

1

Introduction

This chapter provides a general background on solar cells. In particular, the necessity of developing thin-film silicon tandem solar cells is discussed. The working principles of two different solar cell types are explained, namely crystalline silicon wafer-based solar cells and thin-film silicon solar cells. Furthermore, the material properties of different thin-film silicon materials are discussed. In this thesis, the deposition of silicon thin films and solar cells is done using the hot-wire chemical vapor deposition technique. A comparison is given between this technique and the commonly used plasma-enhanced chemical vapor deposition technique. The chapter ends with a brief overview of previous work on hot-wire deposited amorphous silicon, and with the aim and outline of this thesis.

1.1 Solar energy

The enormous increase in the demand for energy worldwide has resulted in an ever growing need for renewable energy sources, such as wind energy, hydrodynamical energy and solar energy. All of these forms of energy are in principle capable of producing large quantities of electricity for present as well as for future use. A strong point of these forms of energy production is that they have an environmentally-friendly nature, as they do not contribute to the production of carbon dioxide or other greenhouse gasses. Furthermore, the sources for these types of energy production are available in nearly ever-lasting abundance. For instance, the amount of solar energy reaching the earth every year is roughly 10^{24} J. This is more than a thousand times more than the annual energy consumption of the entire world, indicating that (in principle) the worldwide requirement for energy could be supplied by solar energy. Conversion of this type of energy into electrical energy is achieved using solar cells. The principle of this energy conversion is based on the photovoltaic (PV) effect: if the energy of an incident photon is larger than the bandgap E_g of a semiconductor, an electron can be excited from the valence band to the conduction band, leaving behind a hole in the valence band. Thus, free charge carriers are generated, which can be collected in an external circuit so that the electrical energy can be used. Unfortunately, as the price of solar energy is currently much higher than that of fossil energy, the market share of solar energy is limited.

At the moment, the solar energy market is dominated by crystalline and multicrystalline silicon wafer-based solar cells. A wafer-based cell consists of a double-

layer structure of a *p*-type and an *n*-type region, where one of the two regions is much thicker than the other. An electric field is generated over the *p-n* junction. Charge carriers are mainly generated in the field free region in the thick lightly doped layer. They diffuse towards the electric field region, where they are separated. Finally, they are collected in an external circuit. As a result, crystalline silicon solar cells are diffusion-type devices. Although the energy conversion efficiency of these solar cells can be almost 25 % [1], a major drawback of crystalline silicon is the fact that the bandgap of 1.1 eV is an indirect bandgap. This means that also a phonon is needed for the photoexcitation of an electron from the valence band to the conduction band. As a consequence, the absorption in the material is low, and thick layers are needed for efficient light absorption. Thus, the material costs are high, and even dominant for crystalline silicon wafer-based solar cells.

Thin-film solar cell materials are investigated worldwide as an alternative for crystalline silicon. The main feature of thin-film materials is that they are made via deposition on a substrate, either by physical vapor deposition (PVD), or chemical vapor deposition (CVD). As a consequence, thin-film materials and solar cells can be produced at much lower costs, which can result in a better price-performance ratio. Furthermore, thin-film solar cells can be deposited on cheap, flexible, substrates. Typical thin-film materials are cadmium telluride, copper-indium diselenide, cadmium sulfide, and thin-film silicon (e.g. amorphous silicon) and its alloys (e.g. silicon germanium (SiGe) and silicon carbide (SiC)).

At present, the material most widely used for thin-film solar cells is hydrogenated amorphous silicon. Advantages of silicon are the fact that it is abundant, and also non-toxic. Usually, the material is made using CVD, where a silicon-containing gas (e.g. silane) is used as source gas. Adding boron- or phosphorous-containing gasses during deposition results in *p*- or *n*-doped material, respectively.

1.2 Hydrogenated amorphous silicon

Hydrogenated amorphous silicon (*a*-Si:H) consists of a covalent random network of Si-Si and Si-H bonds. The material does not have a long-range order, in contrast to its counterpart, crystalline silicon. However, short-range order is present, as the silicon atoms are mainly positioned in tetrahedral coordination with an average Si-Si bond length of 0.235 nm. This configuration is similar to the tetrahedral structure present in crystalline silicon. As there is no long-range periodicity in *a*-Si:H, variations in Si-Si bond angles and Si-Si bond lengths exist, which are in the order of 8 % and 1 %, respectively. Therefore, amorphous silicon has different (opto-)electronic properties than crystalline silicon.

Due to the distribution in bond angles and bond lengths, a considerably high density of strained Si-Si bonds is present. The energy levels associated with the elec-

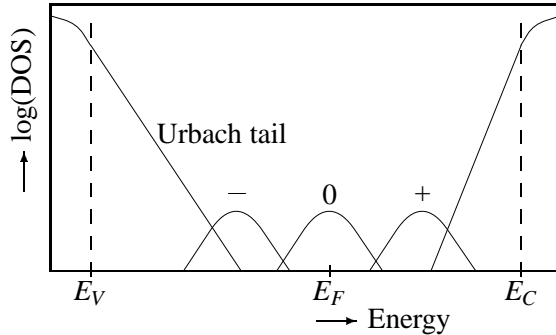


Figure 1.1: Schematic diagram of the distribution of the density of states (DOS) in intrinsic amorphous silicon: $-$, 0 , and $+$ refer to the charge of the defect states [2]. E_V and E_C denote the position of the valence band edge and conduction band edge, respectively. E_F denotes the position of the Fermi level.

tronic states of these strained or weak bonds are located in the band tails. The density of states (DOS) of these tail states decreases exponentially towards the middle of the bandgap. For amorphous silicon, typical values for the inverse slopes of these tails are ~ 50 meV for the valence band tail or Urbach tail, and ~ 25 meV for the conduction band tail. In addition to these strained bonds, also voids and threefold coordinated silicon atoms are present. The latter means that unterminated or dangling bonds are present, with electronic states located near the center of the bandgap, where they act as effective recombination centers for free carriers. Dangling bonds can be occupied by zero, one or two electrons, which results in a positive, neutral, or negative charge, respectively. In pure, non-hydrogenated silicon, produced e.g. by sputtering, the dangling bond density is about 10^{19} - 10^{20} cm^{-3} , which is much too high for application of this material in conventional electronic devices. In hydrogenated amorphous silicon, which contains typically 10 at.% of hydrogen, the majority of the dangling bonds is passivated by hydrogen. In this case, the defect density is greatly reduced to typically 10^{16} cm^{-3} . The presence of hydrogen is thus important for the opto-electronic properties of amorphous silicon. Figure 1.1 shows a schematic overview of the distribution of the density of states in intrinsic amorphous silicon.

Amorphous silicon has several advantages over crystalline silicon. The lack of periodicity in a -Si:H implies a relaxation of the requirement of conservation of the wavevector for interband transitions in opto-electronic processes. Thus, amorphous silicon behaves as a direct-bandgap material and its red-light absorption is much higher than that of crystalline silicon. Therefore, amorphous silicon solar cells can be made much thinner than crystalline silicon solar cells, and the material costs can be kept low. Furthermore, it is possible to tune the bandgap between 1.6 eV and 2

eV, depending on the deposition conditions.

Unfortunately, the electronic properties of amorphous silicon degrade when the material is illuminated [3]. This phenomenon was discovered in 1977 and is called the Staebler-Wronski effect (SWE), after its discoverers. Due to the illumination the density of dangling bonds increases drastically, and saturates only after a long time. This light-induced increase in the defect density results in a reduced lifetime of the free carriers. The additional dangling bonds can be annealed out completely by heating the material to about 150 °C for a few hours. Although the effect has been known for more than 25 years, it is still unclear what the exact origin of this behavior is. The energy for this process is most likely provided by the recombination of electron-hole pairs, but also the hydrogen concentration and the medium-range order in the material appear to play an important role in the process. Obviously, the presence of these additional defects has a large and undesired influence on the material properties.

1.3 Polycrystalline and microcrystalline silicon

Dilution of the silicon-containing (e.g. SiH₄) source gas with hydrogen during deposition results in the deposition of silicon thin films with different morphologies and textures than amorphous silicon. For low hydrogen dilutions, a material is deposited which has a higher medium-range structural order than standard amorphous silicon. This material also has a higher stability against light-induced changes than amorphous silicon, and it is often referred to as protocrystalline silicon [4]. For increasing hydrogen dilution during deposition, a transition from amorphous to crystalline growth is observed. Materials are referred to as polymorphous silicon (pm-Si:H) [5], (hydrogenated) microcrystalline silicon (μ c-Si:H) [6], heterogeneous silicon (*het*-Si:H) [7], or polycrystalline silicon (poly-Si) [7], depending on the amorphous fraction of the material. The increasing crystalline character of these materials results in an improved stability against light-soaking. Although the exact mechanism for silicon crystalline growth is not known, it is generally accepted that atomic hydrogen etches away weak bonds, leaving behind only strong bonds in a crystalline environment [8]. These crystalline regions act as nucleation centers for further crystalline growth. As a consequence, the structure of a thin-film crystalline layer evolves as a function of the thickness of the layer [6]. The size of the crystallites is mainly dependent on the hydrogen dilution during deposition, but also other deposition conditions, like the deposition rate, play a role. At a low hydrogen dilution, the (small) crystallites are embedded in an amorphous matrix. However, at a certain hydrogen dilution, the crystallites become so large that they coalesce. The grain boundaries between these crystallites are known to be defect-rich regions, in which impurities like oxygen can be present. These defects have a great influence on the (opto-)electronic

properties of the material. Passivation of these grain boundaries with hydrogen results in a strong improvement of the material quality.

Thin-film polycrystalline silicon (poly-Si) is a material that consists of completely coalescent crystallites, without any amorphous phase between them. The material can be deposited by various techniques, which can be divided into two categories. In the high temperature approach ($> 600\text{ }^{\circ}\text{C}$), techniques such as liquid phase epitaxy (LPE) or high temperature CVD can be used to produce large grains ($> 10\text{ }\mu\text{m}$). In the low temperature regime ($< 600\text{ }^{\circ}\text{C}$), techniques like very high frequency CVD (VHF-CVD) or hot-wire CVD are used to deposit material with crystallites typically smaller than 100 nm in the lateral dimension [9]. Due to its complete crystallinity, polycrystalline silicon has an indirect bandgap of 1.1 eV.

Microcrystalline silicon ($\mu\text{c-Si:H}$), also referred to as nanocrystalline silicon [10], is a two-phase material which consists of small crystallites, which are embedded in an amorphous silicon matrix. The size of the crystallites is generally smaller than 20 nm [9]. The bandgap of microcrystalline silicon can be tuned from about 1.1 to 1.6 eV, depending on the amorphous fraction present in the material.

1.4 Thin-film silicon solar cells

The working principle of a thin-film silicon solar cell is very different from that of a crystalline wafer-based solar cell. As was already mentioned in section 1.1, the crystalline silicon p - n device is of *diffusion*-type. In contrast to this, the application of a p - n -structure would not work in the case of thin-film silicon solar cells, as the high density of dopant-induced defects in the doped layers would destroy the electric field. Instead, a thick intrinsic layer is deposited between the p - and n -layer to avoid any dopant diffusion. The doped layers generate an electric field over the intrinsic layer. Charge carriers are generated in the photoactive undoped i -layer, after which they are separated and move in opposite directions under the influence of the electric field. The electrons drift towards the n -doped layer and the holes to the p -layer, where they are collected and a current is generated in an external circuit. This process is schematically illustrated in figure 1.2(a). As the diffusion length of the charge carriers is small (typically 150-200 nm) compared to that of crystalline silicon ($\sim 1\text{ mm}$), the charge collection is dominated by drift transport. A thin-film silicon solar cell is therefore a *drift*-type device. The reason for the small diffusion length is the high defect density in the material, compared to crystalline silicon. Charge carriers are trapped by these defects, which results in a high recombination rate. The presence of an electric field in a solar cell increases the drift velocity of the charge carriers. As a consequence, the rate of charge carrier trapping in deep centers and the recombination rate are lowered. Thus, to avoid recombination of the charge carriers, the electric field should be as high as possible, which means that the intrinsic or absorbing layer should

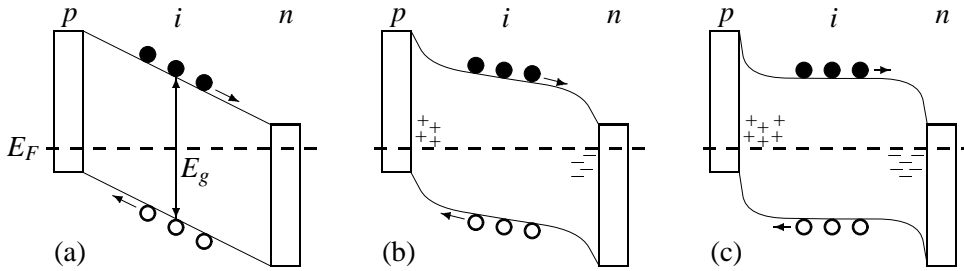


Figure 1.2: Schematic energy band diagram of (a) an ideal thin-film solar cell, (b) a realistic solar cell, and (c) a light-soaked solar cell. Short-circuit conditions are depicted, and the dimensions are not to scale. E_g represents the bandgap of the material. The arrows indicate the transport direction of the electrons (●) and holes (○).

be as thin as possible. On the other hand, the thicker the i -layer is, the more light is absorbed, resulting in a higher generated current. These two opposite requirements result in an optimal thickness of the intrinsic layer. For amorphous silicon, an optimal i -layer thickness of 200-500 nm is found. This thickness is much smaller than the thickness of crystalline silicon solar cells, which is typically 200 μm . As a result, the material costs for thin-film silicon solar cells are much lower than those for crystalline silicon solar cells.

The presence of defects in the intrinsic layer results in an increase in the density of space-charges close to the p - i - and i - n -interfaces [11]. In a realistic solar cell, the electric field in the bulk of the intrinsic layer decreases, and it increases at the p - i - and i - n -interfaces due to the charged defects at these interfaces. The resulting band diagram is schematically drawn in figure 1.2(b). Unfortunately, thin-film silicon solar cells also show degradation due to the Staebler-Wronski effect. The effect depends on the amorphous fraction of the material of the intrinsic layer, and can result in a decrease in efficiency of up to $\sim 30\%$, depending on the thickness of the intrinsic layer. As was mentioned in section 1.2, illumination or light-soaking of the device results in the creation of extra dangling bonds. As a consequence, the electric field in the bulk of the intrinsic layer is reduced further, as shown in figure 1.2(c). Due to this low electric field, the dangling bonds act as efficient recombination centers. Due to this enhanced recombination rate, the charge carrier collection efficiency, and thus the device efficiency, is reduced. Possible options for improving the stability of the solar cell efficiency are the use of thinner intrinsic layers, films with a lower hydrogen concentration, or films with an improved structural order, like protocrystalline or microcrystalline silicon.

For most silicon thin films, the drift mobility of the holes is smaller than that of electrons. In order to collect as many charge carriers as possible, most photocarriers

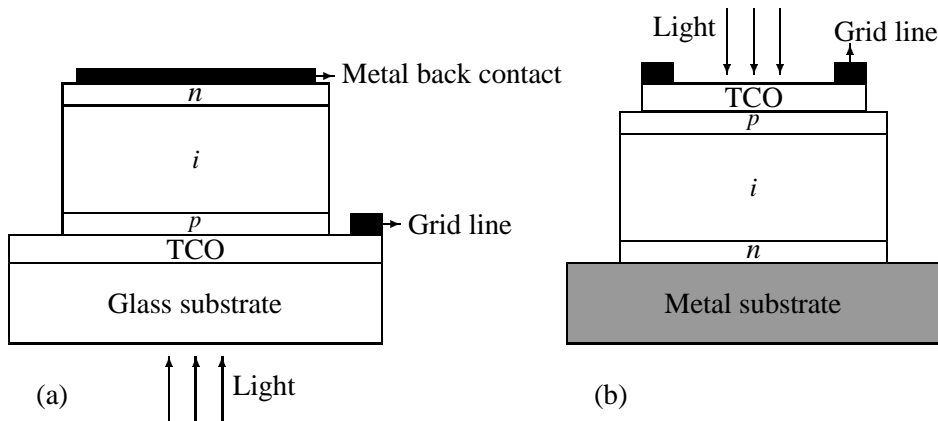


Figure 1.3: Schematic cross section of (a) a *p-i-n* structured solar cell and (b) an *n-i-p* structured solar cell. The dimensions are not to scale.

should therefore be generated close to the *p*-layer, so that the transport length of the holes is kept as small as possible. As most of the light is absorbed in the front part of the solar cell, illumination through the *p*-layer is preferred. The *p*-layer should thus be as transparent as possible, while its good electronic properties should be maintained. For optimal current collection, the solar cell is sandwiched between two electrodes. The front electrode, where the light enters the solar cell, must be conductive and transparent. For this reason, transparent conductive oxide (TCO) layers are used, such as zinc oxide, either doped or undoped (ZnO or ZnO:Al), indium-tin oxide or ITO (In₂O₃:Sn), or tin oxide (SnO₂:F). Metal grid lines can be used to improve the conductivity of the front contact. The back contact consists of a metal, or a highly reflecting TCO/metal combination.

Two structures are commonly used for thin-film silicon solar cells, namely the superstrate or *p-i-n* configuration, and the substrate or *n-i-p* configuration. The difference between these structures is determined by the order in which the different layers are deposited. A *p-i-n* solar cell is deposited on a TCO-coated glass, whereas an *n-i-p* cell is deposited on a metal back contact, such as stainless steel, which can be coated with a highly reflecting TCO-layer. The two solar cell structures are schematically shown in figure 1.3(a) and (b).

Application of textured layers and highly reflective back contact layers results in an enhancement of the light absorption in the solar cell. In a *p-i-n* structured solar cell, this is achieved by using a textured TCO front contact and applying a silver or TCO/silver back contact, which has a high reflectivity. However, these silver back contacts have to be covered with aluminum or an encapsulating polymer to prevent oxidation. In *n-i-p* structured cells, a textured, highly reflecting, layer is deposited as a back contact on the metal substrate before *n*-layer deposition. This can for instance

be a combination of a textured silver layer with a zinc oxide layer.

As the deposition order of the two solar cell structures is different, each cell structure has specific issues which have to be dealt with. By application of a reflective, conducting, back contact, the *n-i-p* cell performance is largely independent of the type of substrate. Therefore, the substrate costs for this type of solar cell can in principle be lower than for *p-i-n* solar cells. Furthermore, the diffusion coefficient of boron is much larger than that of phosphorous in amorphous silicon [12]. Thus, when using high deposition temperatures for the intrinsic layer, the *n-i-p* structure is preferred over the *p-i-n* structure. Another advantage of the *n-i-p* structure over the *p-i-n* structure can be seen when one realizes that the TCO-layer can be chemically reduced by atomic hydrogen, which can be present during the deposition of the intrinsic layer. This process is undesired, as it will result in a reduced transparency of the TCO-layer [13]. In the case of *p-i-n* solar cells, the *p*-doped layer is too thin and too void-rich to act as a hydrogen diffusion barrier. A disadvantage of the *n-i-p* structure is that the deposition temperature of the TCO-layer on top of the cell has to be sufficiently low in order to avoid changes to the silicon layers that are deposited at temperatures below 250 °C. At present, the most widely used solar cell structure is the *p-i-n* configuration.

Solar cells, which consist of a single *n-i-p* or *p-i-n* structure are referred to as single-junction devices. Multijunction solar cells are created by stacking two or more single-junction thin-film silicon cells. These multijunction cells are referred to as tandem solar cells, when two subcells are used, or triple solar cells, when three subcells are used. In multijunction cells, the absorption of light is split over the different subcells. The top cell absorbs mainly the short wavelengths of the solar spectrum, while the subsequent subcells absorb the longer wavelengths. As a consequence, the thicknesses of the intrinsic layers can be reduced, which has a positive influence on the stability of the device. Multijunction cells have an open-circuit voltage, which is ideally equal to the sum of the open-circuit voltages of the single component cells. As the component cells are connected in series, the generated photocurrent of a tandem cell is limited by the minimum of the currents generated in the component cells. Therefore, special attention must be paid to so-called current matching, which basically means adapting the thicknesses of the single cells to each other so that the currents generated in each subcell are equal. A schematic cross section of a *n-i-p/n-i-p* tandem solar cell is shown in figure 1.4(a). From the figure, it can be seen that a reverse (*p-n*) junction is present between the two subcells. This junction is usually called the tunnel-recombination junction (TRJ). Electrons generated in the top cell and holes generated in the bottom cell recombine at this junction. The holes generated in the top cell, and the electrons generated in the bottom cell are collected at the electrodes, which results in a complete current loop. This is schematically depicted in the energy band diagram in figure 1.4(b).

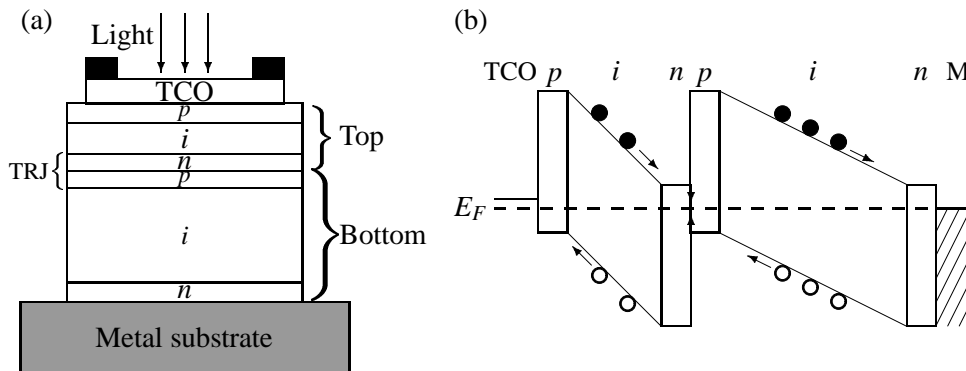


Figure 1.4: Schematic cross section of (a) an n-i-p/n-i-p structured tandem solar cell and (b) the energy band diagram of an ideal tandem solar cell on a metal substrate (M) under short-circuit conditions. The two intrinsic layers have the same bandgap. The arrows indicate the transport direction of the charge carriers. Electrons generated in the top cell recombine with holes generated in the bottom cell. The dimensions are not to scale.

Multibandgap solar cells, where the intrinsic layers of the separate subcells are made of materials with different bandgaps, are used to absorb a larger part of the energy per photon throughout the solar spectrum. In this case, the top cell has the highest bandgap, which results in absorption of the short wavelengths of the solar spectrum. The bottom cell has the lowest bandgap, which results in absorption of the long wavelengths of the spectrum that are not absorbed by the top cell. A high-quality tunnel-recombination junction is a key ingredient for a high-efficiency multibandgap solar cell. Problems that are often encountered in tunnel-recombination junctions are the efficiency of charge carrier recombination, the reverse photovoltage, and the transparency. Therefore, it is straightforward that there can be a number of absorption losses in a tandem cell, but the minimization of these losses is complex. At the moment, the highest measured energy conversion efficiency for a thin-film silicon tandem solar cell is 14.5 % initially [14]. The highest triple cell efficiency is 15.2 % initially for an a-Si:H/a-SiGe:H/a-SiGe:H cell, made in the n-i-p/n-i-p/n-i-p configuration [15]. It is generally believed that a multijunction solar cell structure is required in order to obtain 15 % stabilized efficiency for a silicon thin-film solar cell [16].

1.5 Plasma-enhanced chemical vapor deposition

At present, the plasma-enhanced chemical vapor deposition (PECVD) or glow discharge technique is the most widely used method to deposit silicon-based thin films and solar cells. The technique is based on the dissociation of silicon-containing

gasses in a radio-frequency (rf) plasma, usually at a frequency of 13.56 MHz. The plasma is generated between two electrodes, and the substrate is attached to the grounded electrode. Inelastic collisions of energetic free electrons in the plasma with the source gas molecules result in the production of silicon-containing radicals (Si_xH_y) and hydrogen radicals, but also ions are produced. These species can react further with other radicals, ions and molecules in the gas phase. Radicals that diffuse to the substrate can contribute to the film growth. For the growth of a compact layer, it is important that the surface mobility of the growth precursors is high. This surface mobility is greatly improved by passivation of the already present surface dangling bonds by hydrogen [17]. A growth radical which reaches the surface of a growing film attaches to one of the hydrogen passivated surface silicon dangling bonds. In order to find an energetically favorable position, the radical can diffuse over the surface by hopping over the surface hydrogen atoms. Cross-linking with the neighboring silicon atoms finally results in film growth, under the release of molecular hydrogen. For the deposition of device quality *a*-Si:H, SiH_3 radicals are the main growth precursors [17].

The ions that are produced in the plasma are accelerated under the influence of the electric field between the electrodes. The resulting ion bombardment on the growing surface strongly affects the material properties. The energy which is released when an ion is stopped and neutralized at the film surface improves the surface mobility of the growth precursors and also the cross-linking process, resulting in a denser silicon network. Therefore, the ions are commonly believed to be necessary for the growth of device quality thin-film silicon. On the other hand, energetic ions, with a kinetic energy higher than 20 eV, are thought to cause defects in the material [18].

Although it is possible to deposit high-quality material and solar cells with the PECVD technique, the technique has some serious drawbacks for industrial applications. The main issues are the low deposition rate (typically a few Å/s for amorphous silicon), and the thickness inhomogeneity over large areas, in particular when the plasma frequency is increased to the (very) high frequency region. Therefore, alternative deposition methods are under investigation worldwide, such as hot-wire chemical vapor deposition, very high frequency chemical vapor deposition (VHF-CVD) [19], or deposition using an expanding thermal plasma (ETP) [20].

1.6 Hot-wire chemical vapor deposition

Since its discovery in 1979, the hot-wire chemical vapor deposition (HWCVD) technique has been developed as a promising method for the deposition of silicon-based thin films and solar cells [21–24]. The technique is based on the decomposition of silicon-containing gasses at a catalytic hot surface. Therefore, the method is often referred to as thermo-catalytic CVD (TCCVD) [25] or catalytic CVD (Cat-CVD) [26].

Usually, tungsten or tantalum filaments are used as catalyst, with filament temperatures roughly between 1400 °C and 2100 °C. Depending on the filament material and temperature, silane (SiH_4) gas can be entirely dissociated into atomic Si and H at the catalyst surface. The created species react further in the gas phase, where growth precursors are formed. As there are no ions present during deposition, the gas phase species and reactions that occur are different from those in the PECVD process. Furthermore, the absence of negative ions during deposition ensures that no dust is formed. The gas phase reactions and deposition process of HWCVD will be discussed in more detail in section 2.1.

Advantages of the hot-wire CVD technique over the PECVD method are the high deposition rate, the unlimited scalability to large areas, and the low equipment costs, as no expensive rf-generators and matching networks are needed. Ultrahigh deposition rates of well over 10 nm/s have been obtained in the case of *a*-Si:H [27]. In addition, it is possible to deposit amorphous silicon films with a low defect density and a low hydrogen content below 1 at.% [23]. These layers show reduced degradation upon light-soaking compared to cells with a conventional PECVD deposited layer [28, 29]. This reduced Staebler-Wronski effect is attributed to the very low hydrogen content of these hot-wire deposited layers (1-4 at.%). Solar cells incorporating a hot-wire deposited absorbing layer show improved stability upon light-soaking compared to plasma deposited cells [30]. Furthermore, the absence of ions has the advantage that no defects are created that are a result of energetic ion bombardment. However, as there are no low-impact species to densify the layer, it is still unclear how it is possible that low hydrogen content, device quality amorphous silicon can be deposited with the hot-wire CVD method. One aspect is however that the substrate temperature during hot-wire deposition is higher (by ~ 100 -150 °C) than that commonly used in the PECVD process.

Another possible drawback of the HWCVD method in comparison to PECVD is the control of the substrate temperature. Due to the heat radiation from the filaments, it is difficult to use substrate temperatures below 200 °C. Furthermore, reactions of the source gasses with the filaments result in the formation of silicides on the filaments. These silicides change the catalytic properties and cause aging of the filaments. As a result, the filaments become brittle, which in the past has resulted in breakage of the filaments. Fortunately, by choosing appropriate designs for both the deposition chamber geometry as well as the catalyst geometry, and by an appropriate (pre-)treatment of the filaments, these issues can be overcome [31–33].

1.7 Previous work

At Utrecht University, the hot-wire CVD technique has been applied for the fabrication of amorphous and polycrystalline silicon layers and solar cells. Previously,

amorphous silicon was deposited at high substrate temperatures, using tungsten filaments [34]. Optimum material quality was found at a substrate temperature of 430 °C. The deposition rate of this material was more than 2 nm/s. Unfortunately, amorphous silicon deposited at this temperature still contained a rather high hydrogen concentration of about 8 at.%. Application of this material in an *n-i-p* structured solar cell on plain stainless steel resulted in an initial energy conversion efficiency of 5.5 %. In order to achieve this efficiency, the use of a special thermally stable *n*-layer was necessary. In addition, due to the high substrate temperature, hydrogen in the material diffused out from the top region of the intrinsic layer, resulting in a deterioration of the fill factor. Therefore, special rehydrogenation procedures were necessary after *i*-layer deposition. The stability of these hot-wire deposited solar cells was equal to that of PECVD deposited solar cells. Therefore, a lower hydrogen concentration in the absorbing layer was needed to improve the solar cell stability. It was speculated that the hydrogen concentration was high due to subsurface defect creation followed by passivation of the defects by atomic hydrogen. The high light intensity from the filaments during deposition might play a role in the process of hydrogen incorporation during growth due to light-induced diffusion. Also the high deposition rate could prevent a low hydrogen concentration. Both issues could be solved by reducing the filament temperature. However, tungsten silicides are formed easily at low temperature, resulting in a reduction of the filament lifetime [35]. Therefore, the tungsten filament temperature has to be high to prevent any silicide formation. The use of tantalum as filament material was expected to overcome this problem. Tantalum also acts as a catalyst for the silane dissociation reaction, but the formation of tantalum silicides is much less than the formation of tungsten silicides [35]. As a result, the filament lifetime can be longer, and the filament can be operated at a low filament temperature.

Not only amorphous silicon, but also intrinsic polycrystalline silicon has been developed using the hot-wire CVD method. Two main types of polycrystalline silicon have been made: one with randomly oriented small crystals (*Poly1*) and the other with columnar (220) oriented crystals, with a thickness dependent texture (*Poly2*). *Poly1* is deposited with high hydrogen dilution of the silane and does not show any incubation phase. The deposition rate of this material is about 1 Å/s. *Poly2* is deposited at low hydrogen dilution, at a deposition rate of 5-10 Å/s. However, *Poly2* shows an incubation layer before nucleation with a thickness in the order of 50 nm. For the polycrystalline material used in solar cells, a profiled layer consisting of 15 nm of *Poly1* is deposited with *Poly2* on top of this. As a result, the crystalline volume fraction of the entire structure is larger than 90 %. These depositions are done with two tungsten filaments. The substrate temperature during deposition is about 500 °C. Application of a profiled polycrystalline silicon layer in an *n-i-p* structured cell resulted in an initial efficiency of 4.41 % [36].

1.8 Aim of this work

The primary aim of this work was the further development of hot-wire deposited amorphous silicon using tantalum as filament material. As was indicated in the previous section, the use of tantalum allows a decrease of the filament temperature with respect to commonly used filament temperatures for tungsten. As a result, the substrate temperature and the deposition rate can be lowered, which opens the possibility of a lower hydrogen concentration in the material. Doing so, the aim was to deposit material with a hydrogen concentration lower than 5 at.%, with a bandgap of 1.6-1.65 eV, and with an improved stability upon light-induced defect creation compared to PECVD deposited amorphous silicon.

Furthermore, improvements to the *n-i-p* structured solar cell on stainless steel were investigated. Using amorphous silicon deposited at low temperature, the aim was to improve the initial conversion efficiency to 7 %. This solar cell could then be applied as the top cell of a multibandgap tandem *n-i-p/n-i-p* structured solar cell, where the absorbing layer of the bottom cell is made of polycrystalline silicon. As polycrystalline material has a bandgap of 1.1 eV, optimized tandem cell absorption can be obtained when the bandgap of the top cell amorphous silicon is 1.65 eV. Next to optimization of hot-wire deposited intrinsic amorphous silicon for solar cells, also the possibility of depositing *n*-doped layers using the hot-wire CVD technique has been investigated.

1.9 Outline of this thesis

The subject of this thesis is hot-wire chemical vapor deposition of thin-film silicon tandem solar cells. In total, the thesis consists of nine chapters. Chapter 1 provides a general introduction on solar cells and silicon thin films.

In chapter 2, details of the hot-wire chemical vapor deposition technique are explained. Furthermore, the experimental setups for the deposition of silicon thin films, and for the characterization of the thin-film materials and solar cells are described.

Chapter 3 addresses the deposition and characterization of hot-wire deposited hydrogenated amorphous silicon layers, where tantalum is used as the filament material. The influence of specific deposition parameters on the material properties was investigated. It is shown that both the filament history and the deposition pressure are crucial parameters for the material quality and that both can be controlled.

Chapter 4 deals with the incorporation of hot-wire deposited amorphous silicon as the absorbing layer in thin-film solar cells. For this purpose, both the *n-i-p* and *p-i-n* structures were investigated. It is shown that the application of the hot-wire CVD method for the deposition of solar cells can result in a high initial energy conversion efficiency.

In chapter 5, the reproducibility of *n-i-p* structured solar cells with a hot-wire deposited amorphous silicon absorbing layer is discussed. Although it is possible to make high-quality solar cells, many cells occasionally have shown shunting behavior, and (part of) the photogenerated current is lost. This behavior is shown to be directly correlated with the filament age and different successful methods for avoiding shunted cells and for improving the reproducibility of cell performance are presented.

Chapter 6 deals with the deposition and characterization of hot-wire deposited polycrystalline and microcrystalline silicon layers. It is shown that the reproducibility of high-quality polycrystalline silicon is difficult. Therefore, microcrystalline silicon was developed as an alternative narrow-bandgap material. The influence of different deposition conditions on the material properties is discussed. Furthermore, results are presented on high-quality solar cells with a microcrystalline silicon intrinsic layer.

In chapter 7, the applicability of the hot-wire CVD method for the deposition of *n*-doped layers is investigated. The influence of different deposition conditions on the electronic properties was investigated. Results on solar cells, incorporating these *n*-doped layers, are presented.

Chapter 8 gives an overview of different preliminary multibandgap tandem solar cells that have been made with hot-wire deposited amorphous silicon, microcrystalline silicon, and polycrystalline silicon. Results on a triple-junction cell with amorphous and microcrystalline silicon absorbing layers are presented.

Finally, in chapter 9 the main conclusions of this thesis are summarized.

2

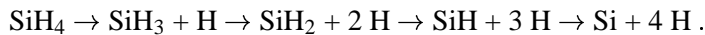
Experimental techniques

In this chapter, details on the hot-wire chemical vapor deposition technique are presented. Furthermore, the experimental setup for the deposition of silicon thin films is described. All important material and solar cell parameters are discussed, and the experimental techniques for the characterization of the thin-film materials and solar cells are presented.

2.1 Hot-wire chemical vapor deposition

As was already mentioned in section 1.6, the hot-wire chemical vapor deposition (HWCVD) technique is based on the decomposition of silicon-containing gasses at a catalytic hot surface. The created radicals react further in the gas phase, where growth precursors are formed. As the properties of the deposited film depend strongly on the type of growth precursors, it is essential to understand the gas phase chemistry in order to optimize the deposition process. For this, it is necessary to identify the reactive species in the growth process. Therefore, recently more research is performed worldwide to investigate the dissociation reactions at the catalyst surface, the gas phase reactions, and the film growth reactions.

Usually, tungsten or tantalum filaments are used as catalyst material, but also other materials like molybdenum and graphite can be used. According to Tange *et al.* [37], the silane dissociation process at the filament is based on a hydrogen-abstraction mechanism via



At filament temperatures above about 1800 °C, silane is fully decomposed into one silicon and four hydrogen radicals. At lower temperatures, also SiH₂ and SiH₃ radicals are created at the filament [37]. As the energy needed for silicon atom production (~ 300 kJ/mol [38]) is much lower than four times the Si-H bond dissociation energy (4 × 300 kJ/mol [39]), the dissociation process is proven to be catalytic. Different catalytic properties are found for different catalytic materials [37]. Doyle *et al.* found that the silane decomposition is actually a two-step process [40]. The silane, which collides with the catalytic filament, reacts with the filament and a silicide (W_xSi_y or Ta_xSi_y, etc.) is formed at the surface. The highly reactive hydrogen atoms subsequently evaporate from the filaments. Depending on the filament temperature, the silicon can also be evaporated from the filaments. For a tungsten filament temperature of about 1700 K, the silane decomposition rate is approximately equal to the silicon

evaporation rate [40]. At lower temperatures, the silane dissociation rate is larger than the silicon evaporation rate, so that more silicides are formed on the filament surface. As a consequence, the filament surface changes with the total deposition time. Aged wires show strikingly different radical desorption kinetics, which are related to silicide formation [41].

Radicals that are created at the filament can react further in the gas phase. At low pressures, the mean free path length of the radicals is larger than the distance between the filament and the substrate. As a consequence, the radicals can diffuse thermally to the substrate, with minor or no gas phase reactions. At higher pressures, gas phase reactions take place. Using a filament temperature in the order of 2000 K, the thermal energy of the radicals is only about 0.25 eV. As this energy is low, it is unlikely that endothermic reactions between the radicals occur and only exothermic reactions need to be taken into account [42]. Important exothermic reactions are the reaction of hydrogen with silane, the reaction of silicon with silane, reactions of SiH_3 , and possibly also reactions of Si_2H_2 [43]. From a theoretical point of view, the main gas reaction species are SiH_3 , Si_2H_6 , Si_3H_6 and Si_2H_4 .

Due to the absence of ions and the abundance of atomic hydrogen during the hot-wire CVD process, the growth mechanism is expected to be different from that of the PECVD process [22]. When a growth precursor with a low sticking coefficient arrives at the film surface, it diffuses over the surface until it finds an energetically favorable position. The precursor reacts with the surface and contributes to film growth. There are two types of growth precursors, namely precursors like Si, that insert into a Si-H bond, and precursors like SiH_3 , that react with a dangling bond on the surface. The surface mobility depends on the hydrogenation of the surface, on the number of dangling bonds of the radical arriving at the surface and on the substrate temperature. The hydrogen coverage is determined on the one hand by the hydrogenation by atomic hydrogen or hydrogenated radicals, and on the other hand by the hydrogen abstraction by SiH_3 and by atomic hydrogen, and, in the PECVD process, also by ions. The most likely growth precursors for hot-wire growth are Si, SiH_3 and Si_2H_4 , depending on the filament temperature and the pressure. Finally, the silicon network is constructed via cross-linking: neighboring Si-H bonds combine into a Si-Si bond under the release of molecular hydrogen. Atomic hydrogen diffuses to a large depth (~ 100 nm) into the silicon network and may play an important role in subsurface reactions [34, 44].

2.2 Deposition equipment

All silicon layers are deposited in the multi-chamber high vacuum deposition system PASTA (process equipment for amorphous silicon thin-film applications) [45, 46]. This system consists of five deposition chambers, which are interconnected via an in-

Table 2.1: Characteristics of the different hot-wire deposition chambers.

	#3	#4	#5
Filament material	Ta	W or Ta	Ta
Number of filaments	2	2	2
Filament diameter (mm)	0.3	0.5	0.5
Distance substrate-filament* (cm)	1.5	4	4
Distance between filaments (cm)	4	4	4

* This distance can increase somewhat due to sagging of the wires during deposition.

ternal transport chamber. The background pressure in all chambers is $\sim 10^{-8}$ mbar. Substrates with an area up to 4" by 4" can be used. In deposition chambers #1 to #3 *p*-type, intrinsic, and *n*-type PECVD layers are deposited, respectively. Additionally, chamber #3 is equipped with a removable hot-wire assembly in order to make *n*-doped HWCVD layers. Chamber #4 and #5 are used for hot-wire depositions of intrinsic layers. Details of the three hot-wire deposition chambers are given in table 2.1. In chamber #3, the filaments are positioned parallel to the gas flow direction. In deposition chambers #4 and #5, the filaments are positioned perpendicular to the gas flow direction.

The substrate is heated by radiation from the filaments and, if desired, also by radiation from an external heater. In figure 2.1(a) the filament temperature of tantalum is plotted as a function of the filament current for deposition chambers #4 and #5. All filament temperature measurements were done in vacuum, using a pyrometer with a cut-off filter at 650 nm. During deposition, the presence of the gasses will decrease the filament temperature due to convection and mainly to energy losses due to dissociation of the gas molecules [47]. The substrate temperature in chamber #5 is plotted as a function of the filament current in figure 2.1(b). In this case, no external heating is used.

Before deposition, the filaments and the substrate are preheated with a closed shutter to the desired deposition temperature. Deposition gasses are injected into the chamber and, when an equilibrium temperature is reached, the shutter is opened, so that the deposition on the substrate starts. Silane (SiH_4) gas is used as the main source gas, but sometimes hydrogen (H_2) gas is added. The hydrogen dilution of the silane gas is defined as $\Phi_{\text{H}_2}/(\Phi_{\text{SiH}_4} + \Phi_{\text{H}_2})$, where Φ_x indicates the flow rate of gas *x*. During deposition, the filament current is kept constant to make sure that the layers are reproducible. Silicon films are simultaneously deposited on Corning 1737 glass and on polished, highly resistive ($\rho \sim 20 \text{ } \Omega\text{cm}$), *p*-type crystalline silicon wafer substrates with (100) orientation. The crystalline wafers are cleaned for one minute in an 0.5 % HF-solution in ultrapure water ($\rho = 18.2 \text{ M}\Omega\text{cm}$), followed by an in-situ atomic HWCVD hydrogen treatment to completely hydrogenate the surface.

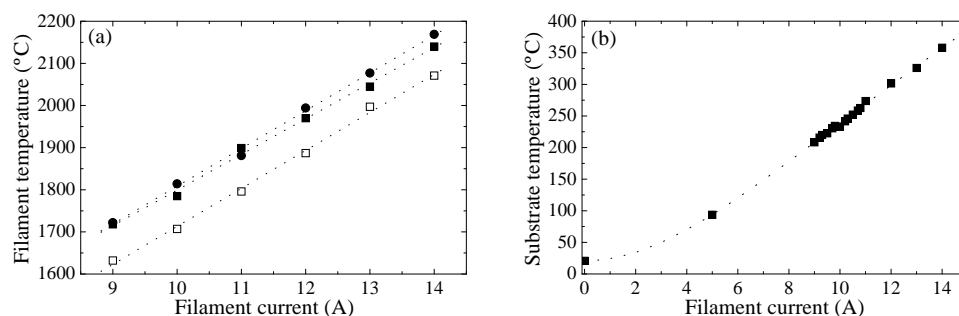


Figure 2.1: (a) Tantalum filament temperature as a function of the filament current for deposition chambers #4 (■) and #5 (●). Also the filament temperature of an aged wire in chamber #4 is shown (□). (b) Substrate temperature in chamber #5 as a function of the filament current when no external heating is used. The temperature is measured with a thermocouple, attached to a Corning substrate. All dotted lines are drawn as a guide to the eye.

The latter treatment results in an improvement of the film adhesion. The thickness of films deposited on Corning glass was measured using a DEKTAK 3030ST surface profilometer. In the case of thin layers (20-250 nm), the thickness can also be determined from reflection/transmission measurements.

In hot-wire CVD, the filaments form the source of the growth precursors. As the deposition occurs primarily via the line-of-sight principle, there is some thickness inhomogeneity of the deposited layers when only two filaments are used. An example of this can be seen in figure 2.2. The thickness uniformity is $\pm 5\%$ over an area of approximately 25 cm^2 . For laboratory experiments, the present thickness distribution is adequate. In a large area production environment, the uniformity can be optimized by using distributed multiple filaments [32]. Unless indicated otherwise, the material properties were measured in the region where the layer is thickest.

2.3 Material characterization techniques

2.3.1 Optical and electrical measurements

Reflection/transmission

The optical properties of the films were determined from reflection and transmission measurements in the wavelength regime of 420-1035 nm (3-1.2 eV). With the computer code 'Optics' [48], the Fresnel equations for the reflectance and transmittance of a light beam at an interface were solved as a function of the photon energy E by an iterative procedure. From these calculations, the real and imaginary part of the com-

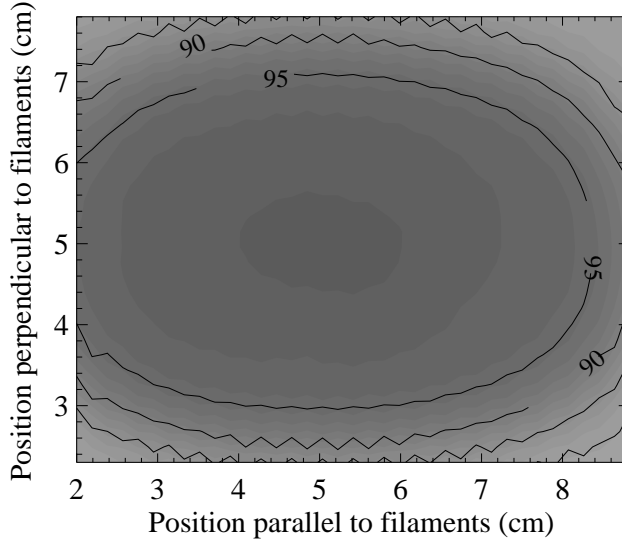


Figure 2.2: Thickness profile of (part of) an amorphous silicon layer deposited in deposition chamber #5. The numbers indicate the thickness percentage relative to the maximum thickness.

plex refractive index $\hat{n}(E)$, and the layer thickness d can be derived. The complex refractive index is defined as $\hat{n}(E) = n(E) - ik(E)$, where n is the refractive index and k the extinction coefficient. The absorption coefficient α is defined as $4\pi k/\lambda$. The value of the refractive index at zero photon energy, n_0 , was determined by extrapolating the $1/(n(E)^2 - 1)$ data to $E = 0$. In the high absorption region ($\alpha \geq 10^4 \text{ cm}^{-1}$), the optical bandgap can be determined from

$$(\alpha n E) = c(E - E_g^{\text{opt}})^{r_1 + r_2 + 1}, \quad (2.1)$$

where c is a constant, and r_1 and r_2 are parameters to describe the shape of the band edges [49]. In literature usually Tauc's convention, where parabolic band edges are assumed ($r_1 = r_2 = 0.5$), is used to deduce the so-called Tauc bandgap from the absorption spectra. However, when linear band edges are assumed ($r_1 = r_2 = 1$), the so-called cubic gap is obtained from a better fit over a larger energy interval. The cubic gap has a value that is ~ 0.2 eV lower than the Tauc bandgap. In an alternative method to measure the bandgap, the energy value E_{04} , where α equals 10^4 cm^{-1} , is determined. The latter value is independent of the band edge model, and can therefore be obtained with the smallest error.

Conductivity and activation energy

Two coplanar metal electrodes were deposited on the layers on Corning glass for all electrical measurements. The dark conductivity and activation energy for electric conduction were measured in vacuum, after annealing at 160 °C for at least 90 minutes to make sure that all moisture had evaporated from the films. During the cooling period the dark current $I_d(T)$ was measured. The dark conductivity σ_d is calculated from

$$\sigma_d(T) = \frac{I_d(T)l}{Vwd}, \quad (2.2)$$

in which l is the distance between the electrodes (~ 0.5 mm), V the applied voltage, w the width of the electrodes (~ 2 cm) and d the thickness of the film. From the slope of the Arrhenius plot of the dark conductivity versus the reciprocal temperature T , the activation energy E_{act} is determined.

The photocurrent I_{ph} was measured using a WACOM dual source solar simulator, which provides an AM1.5 spectrum with an illumination intensity of 100 mW/cm². The photoconductivity σ_{ph} was calculated from the photocurrent, similarly to equation (2.2). The ratio of the photoconductivity and the dark conductivity at room temperature is defined as the photoresponse S , which should be as high as possible for device quality material (e.g. $S > 10^5$ for amorphous silicon and $S > 10^2$ for microcrystalline and polycrystalline silicon [18]).

Constant photocurrent method

To determine the defect density N_d of amorphous silicon layers, the sub-bandgap absorption was measured with the constant photocurrent method (CPM). This technique is based on the measurement of the photoconductivity at low photon energies. The photoconductivity can be written as

$$\sigma_{ph} = e\mu\tau G, \quad (2.3)$$

where e is the electronic charge unit, μ the mobility of the conducting electrons, τ the carrier lifetime, and G the generation rate, representing the density of charge carriers which are generated per second by the illumination. When a sample is illuminated with monochromatic light at a photon flux $\phi_{ph}(E)$, the photon flux ϕ at a depth x in the material is equal to

$$\phi(x) = (1 - R)\phi_{ph}(E) \exp[-\alpha(E)x], \quad (2.4)$$

in which R is the reflectance of the sample, and α is the absorption coefficient. The generation rate is proportional to the photon flux via

$$G(x) = \eta\alpha(E)\phi(x), \quad (2.5)$$

in which η is the quantum efficiency, or the fraction of absorbed photons that generate free carriers. In the energy regime where the absorption coefficient is small ($\alpha d \ll 1$), the average generation rate over the whole thickness d of the layer can be approximated by

$$G = \eta \alpha(E) \phi_{ph}(E) (1 - R). \quad (2.6)$$

In combination with equation (2.2), the photocurrent is now given by

$$I_{ph}(E) = \frac{e V w d (1 - R) \alpha(E) \phi_{ph}(E) \eta \mu \tau(E)}{l} \propto \phi_{ph} \alpha \eta \mu \tau. \quad (2.7)$$

The lifetime τ of the charge carriers is dependent on the recombination rate of the free carriers. However, when the photocurrent is kept constant for all monochromatic photon energies E , the carrier lifetime is, in good approximation, also constant. Furthermore, the mobility μ is assumed to be constant. Due to the optical thickness of the thin films, interference fringes appear in the experimental absorption spectrum. As the intensity of the transmitted light and reflected light was not measured, the term $(1 - R)$ in equation (2.7) is assumed to be constant, and no correction is made for the presence of the interference fringes [50]. These fringes can, in first approximation, be averaged out from the absorption spectrum. The resulting absorption coefficient is dependent only on the incident photon flux by

$$\alpha(E) = \frac{C_\alpha}{\phi_{ph}(E)}, \quad (2.8)$$

where C_α is an energy independent constant. This constant, and thus the absorption coefficient α , is calibrated with the absolute absorption coefficient obtained from reflection/transmission measurements or from PDS measurements (see next item). The exponential region of the absorption in the valence band tail is also referred to as the Urbach regime, as was already indicated in section 1.2. The inverse logarithmic slope of the absorption coefficient in this regime is denoted as the Urbach energy E_0 . The defect density is calculated from the value of α at the intersection of the weakly increasing contribution of the deep defect states, and the exponentially increasing contribution of the valence band tail states. For this, a proportionality constant of 10^{16} cm^{-2} is used [51].

CPM measurements were performed on intrinsic amorphous silicon films with a thickness around $1 \mu\text{m}$. The measurements were done in vacuum, at room temperature. A halogen lamp was used to illuminate the sample, and one of 25 different band pass filters was used to obtain monochromatic light with photon energies in the range of 0.8-2.2 eV, to allow absorption measurements deeply into the bandgap. For the lowest photon energy, where the absorption is lowest, the light intensity was chosen such that the photocurrent was equal to a few times the dark current. The photocurrent at all other energies was kept constant by adjusting the power to the halogen lamp. A calibrated photodiode was used to measure the photon flux.

Photothermal deflection spectroscopy

Another method to measure the sub-bandgap absorption is the photothermal deflection spectroscopy (PDS) technique. With this technique it is possible to measure the absorption in the deposited layers to values of αd down to 10^{-5} . This allows the determination of the density of mid-gap states in amorphous silicon, as well as the determination of the indirect bandgap of microcrystalline and polycrystalline films, which have a low absorption coefficient. The technique is based on the dissipation of absorbed energy into heat. The sample is immersed in an optically transparent and thermally conductive liquid (Fluorinert FC-40, supplied by 3M) and is illuminated by a chopped, monochromatic pump beam. Depending on the wavelength of the incident light, absorption may occur. The absorbed energy is subsequently dissipated into heat in the surrounding liquid, which results in a change in the refractive index of the liquid near the sample surface. As a consequence, a laser beam directed parallel to the sample surface is deflected. The deflection signal is measured by a position-sensitive detector, which is connected to a lock-in amplifier. The experimental setup is described in more detail by Ullersma [52]. The angle of deflection $\Delta\Phi$ of the probe beam is found to be proportional to the absorption coefficient α [53]:

$$\Delta\Phi \propto L \frac{dn}{dT} I_0 \alpha d , \quad (2.9)$$

in which L is the width of the pump beam spot parallel to the direction of the laser beam, $\frac{dn}{dT}$ is the derivative of the refractive index of the liquid with respect to the temperature, I_0 is the pump beam intensity, and d the thickness of the sample. Measuring both the deflection of the laser beam and the intensity of the monochromatic pump beam at different wavelengths thus yields a relative absorption spectrum of the material. For short wavelengths, where $\alpha d \geq 1$, all light is absorbed in the film and the absorption spectrum becomes flat. To obtain absolute absorption spectra, the data were scaled either to the $\alpha(E)$ data from reflection/transmission measurements, or to the region where αd equals 1. The indirect optical bandgap of microcrystalline and polycrystalline silicon can be derived from a plot of $\sqrt{\alpha}$ versus E .

Although the CPM and PDS techniques are both used to measure the sub-bandgap absorption, the defect absorption measured in the case of PDS is significantly larger than in the case of CPM. The Urbach tail, however, is identical for both techniques. The difference in defect absorption has often been attributed to the contribution of surface defect states or of the layer/substrate interface [51]. However, it seems more likely that the difference is due to different sensitivities of the techniques to charged and neutral defect states [54], as the CPM technique is only sensitive to charged defect states, and the PDS technique is sensitive to both charged and neutral states. In this thesis, each time the technique applied to measure the defect density is indicated.

Steady-state photocarrier grating technique

In the absence of an electric field, the photogenerated electrons and holes in a semiconductor diffuse away from locally high concentrations. The effective mobility of the charge carriers during this so-called ‘‘ambipolar transport’’ is dominated by the mobility of the less mobile charge carrier, or, usually, the minority carrier. In intrinsic amorphous silicon, the holes are the minority carriers in the material. Therefore, the ambipolar diffusion in this material is limited by the diffusivity of the holes. As was already mentioned in section 1.4, the electric field in a solar cell can be small in the bulk of the intrinsic layer due to the presence of charged dangling bonds at the interfaces. Transport in this region of the solar cell is therefore dominated by diffusive transport, and the diffusion of the minority carriers becomes the current-limiting process. Thus, the solar cell performance is correlated to the minority carrier mobility. Information about the minority carrier mobility is obtained using the steady-state photocarrier grating (SSPG) technique. In an SSPG experiment, the sample, on which two coplanar electrodes are deposited, is illuminated by two interfering laser beams with intensities I_0 and I_1 ($I_0 \gg I_1$), such that the interference fringes are parallel to the electrodes. The resulting light intensity pattern I_x on the sample is equal to

$$I_x = (I_0 + I_1) \left[1 + f_0 \frac{2\sqrt{I_0 I_1}}{I_0 + I_1} \cos\left(\frac{2\pi x}{\Lambda}\right) \right]. \quad (2.10)$$

Here, $\Lambda = \lambda / (2 \sin(\delta/2))$ is the grating period, λ the wavelength of the laser light, δ the angle between the two light beams, x the coordinate perpendicular to the electrodes (and thus perpendicular to the direction of the grating fringes), and f_0 an experimental quality factor indicating the reduction in the fringe visibility due to e.g. partial coherence between the laser beams or light scattering ($0 < f_0 \leq 1$). As the generation rate G of the charge carriers is proportional to the light intensity given in equation (2.10), the carrier concentration N , proportional to G^γ , will show a non-uniform distribution as induced by the grating pattern. Therefore, the electrical conductivity of the sample will also not be uniform, and is dependent on the period Λ of the grating pattern. Thus, the ambipolar diffusion length L_{amb} can be obtained from a measurement of the modulated part of the photoconductivity as a function of Λ [55]. During an SSPG experiment the weak excitation beam I_1 is chopped and the photoconductivity is measured using a lock-in amplifier. Thus, the obtained signal is $\sigma_g - \sigma(I_0)$, where σ_g indicates the photoconductivity in the presence of the light interference pattern. The measurement is repeated with the coherent beam I_0 replaced by an incoherent beam with the same intensity I_0 . This is achieved by a rotation of the polarization of I_0 perpendicular to I_1 . In this case, the signal is $\sigma(I_0 + I_1) - \sigma(I_0)$. The ratio between these two signals defines the parameter β :

$$\beta = \frac{\sigma_g - \sigma(I_0)}{\sigma(I_0 + I_1) - \sigma(I_0)}. \quad (2.11)$$

It can then be derived [55] that the parameter β depends on the ambipolar diffusion length via

$$\frac{1}{\Lambda^2} = \frac{f_0 \sqrt{2\gamma}}{(2\pi L_{amb})^2} \sqrt{\frac{1}{1-\beta}} - \frac{1}{(2\pi L_{amb})^2}. \quad (2.12)$$

Therefore, a plot of Λ^{-2} versus $(1 - \beta)^{-0.5}$ (the so-called ‘‘Balberg’’-plot) results in a straight line. The ambipolar diffusion length can be directly obtained either from the slope of the plot, or from the intersection of the line with the Λ^{-2} axis. With the use of this particular representation, the error in the determination of the ambipolar diffusion length is minimized. The value for γ is derived from a plot of the photoconductivity versus the light intensity, which is varied using neutral density filters.

The experimental setup that was used for the experiments is explained in detail in reference [34]. A 5 mW HeNe laser was used, which generates light with a wavelength of 632.8 nm, and a polarization ratio of 500:1. The light beam is split into two coherent beams at a BK7 glass window. The intensity ratio I_0/I_1 between the two beams is equal to 15. A DC voltage of 10 V is applied to the electrodes on the sample, corresponding to an electric field strength of about 200 V/cm. This field strength is low enough to be in the regime of ambipolar diffusion [56]. The polarization of beam I_0 can be changed with a $\lambda/2$ -plate. Two rotatable mirrors are used to direct the two beams onto the sample. The x -position of the sample corresponds with the distance between the sample and the mirrors, which is varied in order to change the grating period Λ .

Due to the presence of surface recombination [57], as well as the small contribution of non-ambipolar transport of carriers [58], and the dependence of L_{amb} on the illumination intensity [34], the shape of the Balberg-plot will become slightly non-linear. However, the slope at a certain value of Λ describes the linear relation of Λ^{-2} versus $(1 - \beta)^{-0.5}$ at the corresponding illumination intensity I_Λ . Unless indicated otherwise, the values of the ambipolar diffusion length reported in this thesis were determined at a light intensity I_Λ of 10 mW/cm². An example of a non-linear ‘‘Balberg’’-plot is shown in figure 2.3.

2.3.2 Structural measurements

Fourier-transform infrared spectroscopy

The hydrogen concentration and bonding configuration of the layers deposited on crystalline silicon were determined using Fourier-transform infrared (FTIR) absorption spectroscopy. For this purpose a Digilab FTS-40 spectrometer is used, equipped with a liquid-nitrogen cooled HgCdTe detector. This spectrometer basically works as a Michelson interferometer [59]. The measured interference signal is Fourier-transformed to give a transmittance ($T(\lambda)$) spectrum. The absorption in the films is then calculated as $\alpha(\lambda) = -\ln(T(\lambda))/d$. The thickness d of these films was deduced

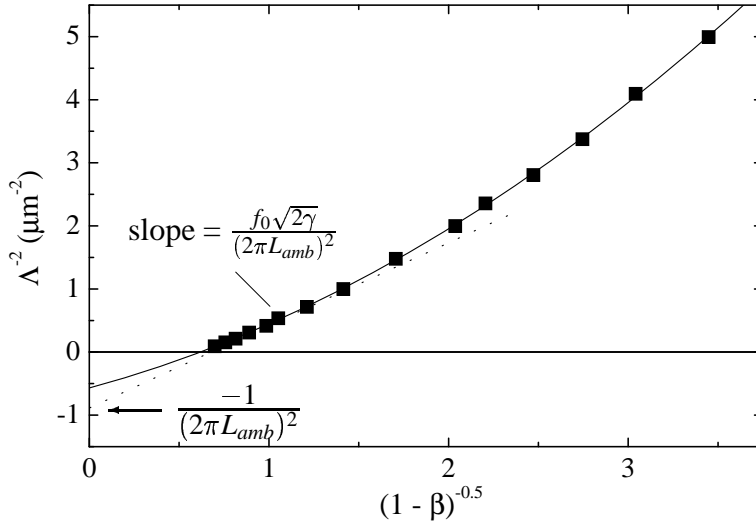


Figure 2.3: Example of an SSPG measurement plot or “Balberg”-plot. The value of the ambipolar diffusion length can be derived from the slope of the plot, or from the intersection of the line with the Λ^{-2} axis. In this case, the ambipolar diffusion length is equal to 170 nm.

from interference fringes in the infrared spectra via

$$d = \frac{1}{2n(\lambda)\Delta\nu}, \quad (2.13)$$

in which $n(\lambda)$ is the refractive index of the material, and $\Delta\nu$ the interference period. As $n(\lambda)$ is approximately constant in the infrared region, only a small error is made when replacing $n(\lambda)$ by n_0 . The measured spectra were then corrected for both incoherent and coherent multiple reflections in the films [60, 61]. The transmittance of the layers was measured in the region $400\text{-}4000\text{ cm}^{-1}$, which corresponds to the wavelength region of $25\text{-}2.5\text{ }\mu\text{m}$. In this region, all relevant Si-H_x and possible silicon-oxide bonding configurations are probed. These peaks are fitted with Gaussians. The integrated absorption of a peak corresponding to a certain absorption mode k is defined as

$$I_k = \int_{-\infty}^{+\infty} \frac{\alpha_k(\omega)}{\omega} d\omega. \quad (2.14)$$

The bonded hydrogen concentration is defined as $[\text{H}] = N_H / (N_{\text{Si}} + N_H) \times 100\%$, and is determined from the absorption around 630 cm^{-1} , which corresponds to the rocking modes of SiH, SiH₂ and SiH₃ [62]. Here, N_H represents the silicon-hydrogen bond density in the material, which is calculated from $N_H = A_{630} \times I_{630}$,

with I_{630} the integrated absorption strength of the rocking modes, as calculated from equation (2.14). N_{Si} is the density of silicon atoms in the material, which is equal to $5 \times 10^{22} \text{ cm}^{-3}$. A proportionality constant $A_{630} = 2.1 \times 10^{19} \text{ cm}^{-2}$ is used, according to Langford *et al.* [61].

The hydrogen bonding configuration is an important parameter for the structure and stability of the material. When only isolated, monohydride (SiH) bonds are present, the layer has a dense structure, which is characteristic for device quality amorphous silicon. These monohydride bonds have a resonance frequency of 2000 cm^{-1} . Less dense material also contains a certain amount of hydrogen that is not bonded in an isolated mode. This hydrogen can be bonded in multihydrides (SiH₂ and SiH₃) or be present at the internal surfaces of voids in the material. These bonds have a stretching mode resonance frequency around 2090 cm^{-1} . In general, material with a considerable amount of hydrogen that is not present in the form of monohydride bonds shows a reduced resistance against photoinduced structural changes [63, 64]. The hydrogen bonding configuration is characterized by the microstructure parameter R^* , defined as

$$R^* = \frac{I_{2090}}{I_{2000} + I_{2090}}. \quad (2.15)$$

Inferior quality amorphous silicon with a high microstructure parameter often has a high void density, resulting in a porous material. If the voids are interconnected, the material oxidizes in air, so that silicon-oxide bonds are formed. These bonds have a resonance frequency around 1100 cm^{-1} , which can easily be probed by FTIR.

Raman spectroscopy

Raman spectroscopy was used to determine the short-range structural order in the silicon films. These measurements are based on the inelastic or Raman scattering of laser light on phonons in the material. This results in a shift in the wavelength of the scattered light, equal to the energy of the phonon that has been created (Stokes scattering) or annihilated (anti-Stokes scattering). For the measurements present in this thesis, the Stokes scattering in the wavenumber region $100\text{-}900 \text{ cm}^{-1}$ was recorded. In this region the relevant phonon modes of crystalline and amorphous silicon are visible. The sharp transverse optical (TO) mode of single-crystalline silicon lies at 520 cm^{-1} . For amorphous silicon, the characteristic modes are the longitudinal acoustic (LA) mode centered around 330 cm^{-1} , the longitudinal optical (LO) mode centered around 445 cm^{-1} , the transverse optical (TO) mode around 480 cm^{-1} , and the hydrogen-associated mode due to Si-H bonds around 630 cm^{-1} . The linewidth of the 480 cm^{-1} mode in amorphous silicon is proportional to the root-mean-squared (rms) bond angle deviation, and is therefore a useful indication of the short-range structural order [65]. The width of this peak is normally larger than $\sim 60 \text{ cm}^{-1}$ [65]. A mixed-phase material, such as microcrystalline silicon, contains small crystalline regions, which give rise to a dispersion of the crystalline TO mode to lower frequen-

cies. This dispersion is dependent on the size of the crystallites [66], and results in a broad mode around 510 cm^{-1} . Quantitative analysis of the Raman spectra was done by fitting the measured spectra with 3 Gaussians at the position of the amorphous LA, LO, and TO mode. The background due to the Rayleigh scattered laser light was subtracted with a Lorentzian fit. If a crystalline fraction is present in the material, two additional peaks, around 510 cm^{-1} and around 520 cm^{-1} , were included in the fit. For a mixed-phase material it is possible to give an estimation of the crystalline volume fraction X_c by comparing the crystalline modes at 510 cm^{-1} and 520 cm^{-1} to the amorphous TO mode at 480 cm^{-1} . To do this, not only the different absorption strengths for amorphous and crystalline silicon should be taken into account, but also the influence of the sizes of the crystallites, and the weighted contributions from various depths in case of a non-uniform distribution. Therefore, this calculation is complex. As an alternative, the crystalline ratio R_c is defined as

$$R_c = \frac{I_{510} + I_{520}}{I_{480} + I_{510} + I_{520}}, \quad (2.16)$$

where I_x is the integrated Gaussian corresponding to mode x . This parameter can then be used to compare the crystallinity of different materials, within the penetration depth of the laser beam.

Raman measurements were performed using the 514.5 nm line of a Spectra-Physics Ar⁺ laser, a Spex triple-grating monochromator, and a liquid nitrogen cooled CCD detector (Roper Scientific). The probing depth with this wavelength is typically 60 nm in the case of amorphous silicon, and is larger in crystalline material, and dependent on the crystalline volume fraction.

X-ray diffraction

X-ray diffraction (XRD) was used to obtain information about the orientation of the crystallites present in the microcrystalline layers. This technique is based on the diffraction of a monochromatic X-ray beam on a crystal lattice. During an XRD measurement, the intensity of the diffracted radiation is measured as function of 2θ , where θ is the angle between the sample surface and the incident X-ray beam (θ - 2θ configuration). Intensity peaks appear at specific angles according to Bragg's law:

$$2d \sin \theta = \lambda_{\text{X-ray}}, \quad (2.17)$$

in which d is the distance between the crystal planes, and $\lambda_{\text{X-ray}}$ the X-ray wavelength. The X-ray beam used for these measurements is the K_α radiation from the copper anode, which has a wavelength of 1.542 \AA [†]. Under the geometrical configuration of the θ - 2θ scan, only the crystal planes which are parallel to the sample

[†]In fact, this beam is not completely monochromatic, but consists of two lines: $K_{\alpha 1}$ and $K_{\alpha 2}$, which have wavelengths of 1.540562 \AA and 1.544390 \AA , respectively.

Table 2.2: Crystal orientations of silicon and corresponding XRD peak positions using copper K_α radiation.

Crystal orientation (hkl)	Lattice spacing (Å)	Peak position 2θ (°)
111	3.135	28.47
220	1.920	47.35
311	1.637	56.20

surface can contribute to constructive interference of the reflected X-ray beam. A list of different silicon crystal orientations is given in table 2.2, together with the corresponding peak angles.

The width of the measured XRD peaks is determined by the size of the crystallites. The average diameter of the crystallites with a certain orientation can therefore be estimated from the corresponding XRD peak using Scherrer's formula [67]:

$$t = \frac{0.9\lambda_{\text{X-ray}}}{B \cos \theta_B}, \quad (2.18)$$

where B is the full width at half maximum of the measured peak in radians, and θ_B the peak angle.

2.4 Solar cell characterization

A thin-film solar cell basically consists of three layers and two contacts, as was already explained in section 1.4. The most important layer is the intrinsic or absorbing layer, in which the light is absorbed and electron-hole pairs are created. The intrinsic layer is sandwiched between a p - and an n -type layer, which build up an electric field. The charge carriers are transported under the influence of this electric field and are collected at the contacts. The contacts to the cell are made from a transparent conductive oxide (TCO) at the top and from a metal at the back of the solar cell. Solar cells are characterized by current-voltage and spectral response measurements.

2.4.1 Current-voltage measurements

A solar cell can ideally be seen as the combination of a diode or p -(i)- n -structure and a photoactive current source I_{ph} . However, current leakage paths, like pinholes and edges, and resistances at the interfaces or at the front and back contacts of the cell give rise to parallel and series resistances. A schematic overview of the electrical equivalent circuit is shown in figure 2.4, in which R_p and R_s represent the parallel and series resistances, respectively. With this model, the total current density J through a

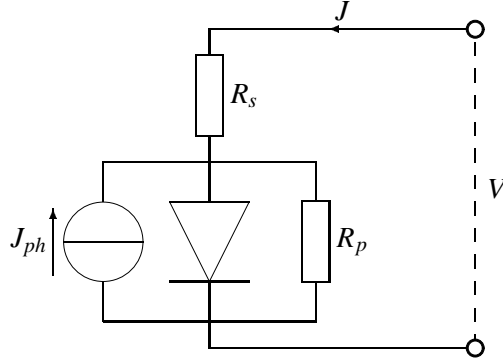


Figure 2.4: Electrical equivalent circuit of a solar cell.

solar cell can be written as

$$J = J_0(\exp[e(V - JR_s)/nk_B T] - 1) + \frac{V - JR_s}{R_p} - J_{ph}, \quad (2.19)$$

in which J_{ph} is the photogenerated current density when the cell is illuminated, J_0 the reverse-bias saturation current density, n the diode quality factor, k_B Boltzmann's constant, T the absolute temperature, e the elementary charge, and V the applied voltage. The value of the diode quality factor n is 1 in the case of diffusion-driven current, and is 2 for pure recombination-driven current. A combination of these different current modes results in a value for the diode quality factor between 1 and 2. The current density at zero voltage defines the short-circuit current density J_{sc} , and the voltage at zero current density is called the open-circuit voltage V_{oc} . In figure 2.5(a) the AM1.5 current density of an amorphous silicon solar cell is plotted as a function of the applied voltage. In this figure also the above discussed cell parameters are indicated. From the J - V curve measured under illumination, the parallel and series resistance are calculated from the slopes of the curve [68]:

$$\left. \frac{dJ}{dV} \right|_{V=0} \approx \frac{1}{R_p}, \quad (2.20)$$

$$\left. \frac{dJ}{dV} \right|_{J=0} \approx \frac{1}{R_s}. \quad (2.21)$$

These resistances affect the current, and cause a further deviation of the J - V curve from the ideal shape. The degree of deviation from a rectangular shape is then expressed in the fill factor FF , defined as the ratio between the power at the maximum power point (mpp) and the product of J_{sc} and V_{oc} :

$$FF = \frac{J_{mpp} V_{mpp}}{J_{sc} V_{oc}}. \quad (2.22)$$

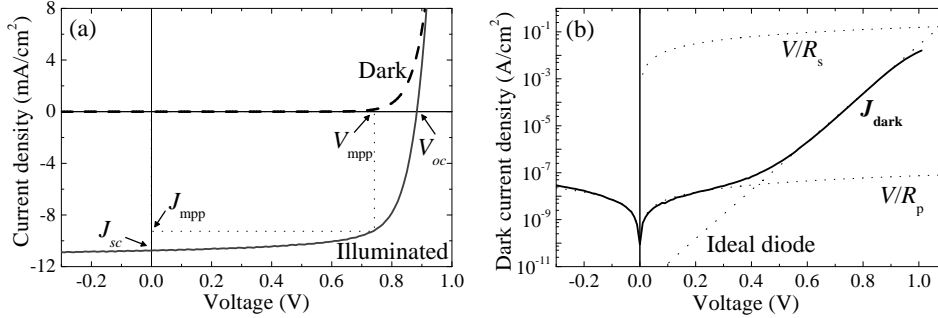


Figure 2.5: (a) AM1.5 and dark J - V characteristics of an amorphous silicon solar cell. (b) Logarithmic plot of the dark J - V characteristics.

The energy conversion efficiency η of a solar cell is then defined as:

$$\eta = \frac{P_{\text{mpp}}}{P_{\text{in}}} = \frac{J_{\text{mpp}}V_{\text{mpp}}}{P_{\text{in}}} = \frac{V_{\text{oc}}J_{\text{sc}}FF}{P_{\text{in}}}. \quad (2.23)$$

In equation (2.19), the collection efficiency does not depend on the applied voltage, which is correct for crystalline silicon cells. However, in drift-type devices like amorphous silicon cells, the photogenerated current I_{ph} , and therefore the collection efficiency, does depend on the voltage due to the large density of defect states within the bandgap. As a result, the diffusion free path length of the photoexcited charge carriers is decreased to values smaller than the geometrical thickness [68]. Although the present model is therefore not completely correct for amorphous silicon based solar cells, the basic idea behind it is well applicable. For $V < V_{\text{mpp}}$, J_{ph} is practically independent of V .

In the dark, the current through a solar cell is given by equation (2.19), but without the photogenerated term J_{ph} . In figure 2.5(b) a schematic logarithmic plot is made of the dark current density of a solar cell versus the applied voltage. It is clear that three regimes can be appointed, in which different mechanisms control the dark current density, as shown in the figure. At low voltages ($V < 0.3$ V in figure 2.5(b)), the dark current density of this solar cell is dominated by the current density V/R_p through the parallel resistance. At voltage above ~ 0.4 V the current density behavior corresponds with exponential, diode-like behavior. At sufficiently high voltages ($V > 0.9$ V), the J - V curve starts to deviate from the diode line, due to the increasing influence of the series resistance and space charges. At even higher voltages, the behavior of the cell becomes ohmic, and the current density approaches V/R_s .

Multijunction or tandem solar cells consist of two or more solar cells, which are stacked on top of each other and are thus connected in series. As the top cell absorbs mainly the short wavelengths of the solar spectrum, the illumination of the bottom

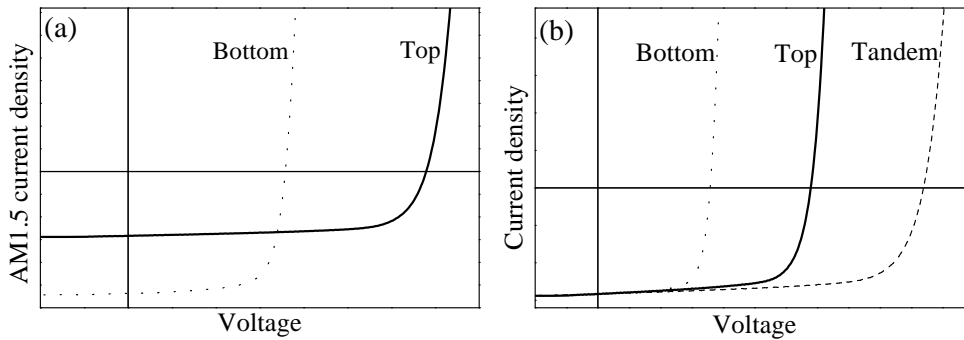


Figure 2.6: Illustration of the current-voltage characteristics of a tandem cell. (a) Current-voltage characteristics of the two single component cells under AM1.5 conditions. The current generated in the bottom cell is higher than that generated in the top cell. (b) Current-voltage characteristics of the two subcells in a tandem cell. As the cells are well matched, the photocurrent generated in the two cells is equal. The resulting tandem cell has a short-circuit current density, which is equal to that of the two subcells, and an open-circuit voltage, which is roughly equal to the sum of the open-circuit voltages of the two subcells.

cell is filtered by the top cell and different from AM1.5 conditions. Consequently, the photocurrent generated in the bottom cell of a tandem cell is lower than that of a similar single-junction solar cell. If the connection between the two cells has a low ohmic resistivity, the voltage generated by the bottom cell of a tandem cell is only slightly lower than that of a similar single-junction solar cell. Therefore, tandem solar cells have an open-circuit voltage, which is roughly equal to the sum of the open-circuit voltages of the single component cells. As the component cells are connected in series, the total current of a tandem cell is limited by the minimum of the currents generated in the component cells, as was already mentioned in section 1.4. The current-voltage characteristics of a tandem solar cell and its components are schematically depicted in figure 2.6(a) and (b).

The measurements were performed using a WACOM dual source solar simulator, in which illumination from a halogen lamp is mixed with that from a xenon lamp using semi-transparent mirrors. The simulator provides illumination with an AM1.5 spectrum at an intensity of 100 mW/cm^2 . A Keithley 238 source-measure unit was used as the voltage source and current meter, using a four point probe configuration. A mask was used to define the illuminated area. Without the use of a mask, photo-carriers that are created just outside the cell area can be collected, which may lead to an increase of the generated photocurrent dependent on the size and geometry of the contact pads area. Also the fill factor is slightly decreased, because the carriers

collected outside the immediate contact area encounter a higher series resistance. For small $n-i-p$ structured cells, the increase in the photogenerated current, due to the absence of a mask, can amount up to $\sim 25\%$. In the case of $p-i-n$ structured cells, this increase is about 10% . Although there are some optical losses in the top contact, no correction was made for the transmittance of the top contacts. In the case of $n-i-p$ cells, the resistivity of the top transparent conductive oxide (TCO) contact was lowered by the use of metal grid contacts on top of the TCO. As these contacts shield the cell partly from illumination, the so-called active or illuminated area defines the cell area.

2.4.2 Spectral response measurements

Spectral response measurements of a solar cell are performed to obtain information about the response of the cell to light of different wavelengths. The cell is illuminated with a modulated monochromatic light beam, and the photocurrent $i_{ph}(\lambda)$ is measured with a lock-in amplifier. In order to create a charge density distribution as under operating conditions, (continuous) bias light should always be used. A bias illumination of approximately one sun results in an increase of the total photogeneration in the cell, similar to the situation under AM1.5 illumination. Therefore, more charge carriers are created and the internal electric field increases. This improves the collection of charge carriers, and thus also the spectral response.

The external quantum efficiency $\eta_{coll}(\lambda)$ is defined as

$$\eta_{coll}(\lambda) = \frac{i_{ph}(\lambda)}{e \phi_{ph}(\lambda)}, \quad (2.24)$$

where $\phi_{ph}(\lambda)$ is the incident number of photons with wavelength λ per unit area per second. From spectral response measurements, information can be obtained about absorption and reflection losses in the cell. A low response to short wavelengths indicates losses in the front contact, p -layer, or at the p/i -interface. For long wavelengths, the spectral response depends on the bandgap, on the thickness of the absorbing layer, on the light scattering properties of the contact layers (TCO) and on the reflectance of the back contact. In particular, the red response can be improved by optimizing the textured, reflecting back contact. From the external collection efficiency the short-circuit current density J_{sc} under AM1.5 conditions can be calculated by

$$J_{sc} = e \int \eta_{coll}(\lambda) \phi_{AM1.5}(\lambda) d\lambda. \quad (2.25)$$

This calculated value for the short-circuit current density corresponds with the value measured during $J-V$ measurements, but a deviation of 10% is allowed.

For single-junction solar cells, the spectral response measurements are usually performed under short-circuit conditions (i.e. no bias voltage is used). However, by

applying a bias voltage the internal electric field of the cell is changed. A negative bias voltage (reverse bias) will increase the internal electric field, leading to a decrease of trapping and/or recombination of charge carriers. Sometimes, this results in an increase of the external collection efficiency if the absorbing layer is not already fully depleted at 0 V. Good quality cells show complete collection at 0 V. At a certain negative voltage all charge carriers will be collected, resulting in saturation of the external collection efficiency.

The spectral response of tandem cells can also be measured. This is done by measuring the separate spectral responses of the two subcells. However, as the absorption of most of the monochromatic light is distributed unevenly over the two subcells, this is not straightforward. When no bias light is used (dark), the spectral response of a tandem cell is equal to the minimum of the two spectral responses of the subcells. Therefore, to measure the response of one of the two subcells, the other subcell must generate enough current so that the cell that is probed actually limits the total current in the tandem cell. This current generation is obtained by the use of bias light, with wavelengths that are not absorbed in the subcell that is probed. For instance, to measure the spectral response of the top cell, the tandem cell is illuminated with continuous red light. The top cell is transparent for this light, and most of the red light is absorbed in the bottom cell. The response of the top cell is measured using chopped monochromatic light. To measure the bottom cell, the current generated in the top cell is saturated by the use of blue light.

Another important issue for the measurements of tandem cells is the use of a bias voltage. Namely, when no bias voltage is applied, the voltage over each subcell is not zero and the subcells are not measured under short-circuit conditions. Kirchhoff's

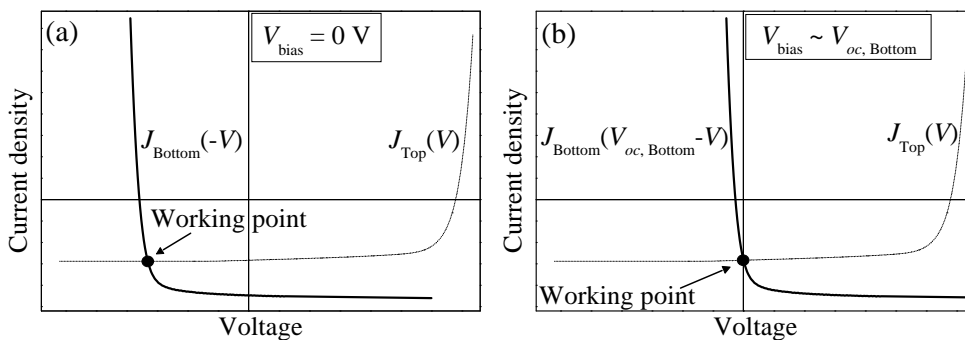


Figure 2.7: Illustration of the working point shift of a tandem cell, as a function of the bias voltage. The top cell is probed. (a) Working point when no bias voltage is applied. (b) A bias voltage roughly equal to the open-circuit voltage of the bottom cell is applied to shift the working point to short-circuit conditions for the top cell.

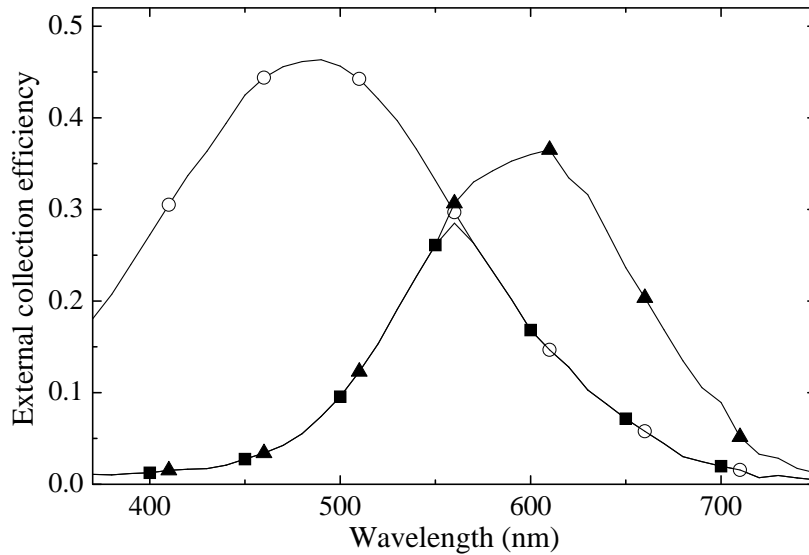


Figure 2.8: External collection efficiency of the top cell (○) and bottom cell (▲) of a tandem cell. Also plotted is the response of the tandem cell in the dark (■).

rules must be obeyed, which state that:

$$V_{\text{Top}} + V_{\text{Bottom}} = V_{\text{bias}} , \quad (2.26)$$

$$I_{\text{Top}} = I_{\text{Bottom}} . \quad (2.27)$$

Thus, by applying a bias voltage, the working point of the probed subcell can be shifted to short-circuit conditions ($V = 0$ V). The correct value of the bias voltage is approximately equal to the open-circuit voltage of the subcell that is not probed. This is illustrated in figure 2.7.

An example of the external collection efficiency of a tandem cell is shown in figure 2.8, together with the response in the dark. The short-circuit current density of a tandem cell is equal to the lowest of the short-circuit current densities of the separate subcells.

2.4.3 Degradation of solar cells

In order to measure the degradation of solar cells during illumination, light-soaking experiments were performed. The free carrier concentration in the layer increases due to the illumination, and results in an increase of the recombination rate. As the Staebler-Wronski effect is a recombination-driven process [69], defects are created

in the material and the solar cell parameters deteriorate. Measurements of the solar cell characteristics were performed as a function of the light-soaking time. For this purpose, a metal-halide lamp was used, providing an illumination intensity of $\sim 100 \text{ mW/cm}^2$. The lamp spectrum is not identical to the AM1.5 spectrum, as it had a higher intensity in the blue ($\sim 120\%$ of the AM1.5 spectrum at 400 nm). The intensity for wavelengths above 700 nm was very low. Therefore, the spatial defect distribution was different from that under working conditions. In the latter case more defects are generated in the bulk of the layer and more annealing takes place, due to the higher red light intensity. As a result, the light-soaking experiments may overestimate the degradation under AM1.5 illumination, as blue photons were always absorbed, and the cell was not heated up due to the absence of red photons. Fortunately, this effect is not large, so the measurements give a good indication of the resistance of the material to photoinduced structural changes.

3

Hot-wire deposited intrinsic amorphous silicon

With the use of tantalum as filament material, it is possible to decrease the substrate temperature of hot-wire deposited intrinsic amorphous silicon, while maintaining device quality material. The influence of specific deposition parameters on the material properties was investigated. It is shown that both the filament history and the deposition pressure are crucial parameters for material quality, as the formation of silicides on the filaments has a detrimental effect on the deposition rate and the ambipolar diffusion length. Optimal material properties are obtained at a substrate temperature of 250 °C, showing the beneficial effect of a moderate deposition temperature on the material quality of hot-wire deposited intrinsic amorphous silicon.

3.1 Introduction

The hot-wire chemical vapor deposition (HWCVD) or catalytic CVD (Cat-CVD) technique has gained much attention in the last two decades, especially for the deposition of silicon-based thin films and solar cells [21–24]. The high growth rate of more than an order of magnitude higher than that of the commonly used plasma-enhanced CVD (PECVD) process, the possibility to deposit uniformly over a large area, and the low equipment costs have made the HWCVD technique an attractive alternative for the PECVD process. With the HWCVD technique, however, device quality hydrogenated amorphous silicon (*a*-Si:H) has mainly been made at high deposition temperatures of over 350 °C [23, 24]. Previously at Utrecht University, amorphous silicon deposited at 430 °C was optimized for the incorporation in *n-i-p* cells [24]. This material was made at a high deposition rate of more than 2 nm/s, and had an ambipolar diffusion length of about 170 nm. The Tauc bandgap of this material was 1.7 eV [34]. The incorporation of these hot-wire deposited layers in devices like *p-i-n* structures or multijunction solar cells is hindered, as the underlying *p*-doped silicon layers and/or transparent conductive oxide (TCO) layer deteriorate at such high temperatures. For these applications, it is essential that the deposition temperature of the hot-wire deposited absorbing layer is lowered in order to protect the underlying TCO-layer and/or the *p*-layer.

As was already mentioned in section 1.8, the aim of this work was to investigate if the deposition temperature of hot-wire deposited amorphous silicon can be lowered

while device quality is maintained. For this, tantalum was used as filament material. The formation of silicides on this material is reduced [35], which allows for a substantial decrease of the filament temperature. As a result, the substrate temperature can be lowered as well.

In this chapter, the effects of several deposition parameters in the HWCVD process on the structural and (opto-)electronic properties of *a*-Si:H are described. Results of the dependence of the material properties on the substrate temperature are presented and compared with results on material deposited at 430 °C.

3.2 Influence of the substrate temperature

To measure the effect of the substrate temperature on the material properties of amorphous silicon, films were deposited at different filament temperatures and heater temperatures. All layers were deposited in chamber #4 of the PASTA system, using a single pair of filaments. The filament current was varied between 11.0 A and 9.0 A, corresponding to virgin filament temperatures in vacuum between 1900 °C and 1720 °C. However, the filament temperature can decrease by as much as 100 °C when the filaments age (see figure 2.1(a)). During deposition, the presence of the gasses will decrease the filament temperature further due to energy losses due to dissociation of the gas molecules, and due to convection [47]. The resulting substrate temperatures were between 275 °C and 200 °C when no external heating was used. By setting the heater to 450 °C with the filaments on, an increase in substrate temperature of about

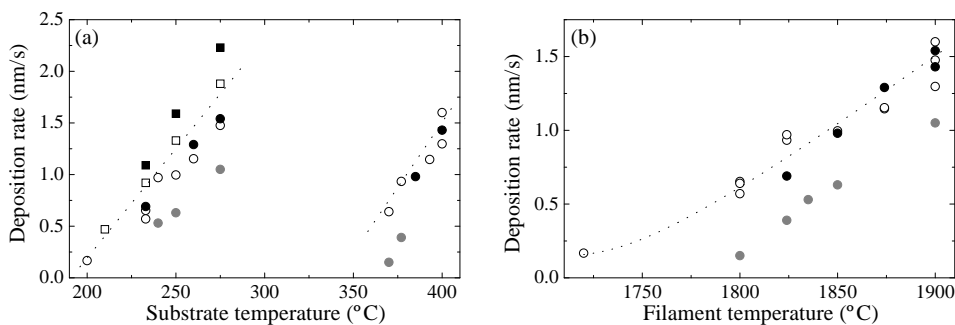


Figure 3.1: (a) Deposition rate as a function of the substrate temperature and (b) deposition rate as a function of the filament temperature in vacuum. Two different gas flow rates were used, namely 60 sccm (■) and 90 sccm (●). The closed symbols represent thick layers, and the open symbols represent thin layers. The dotted lines serve as guides to the eye. The gray symbols will be discussed in section 3.2.2.

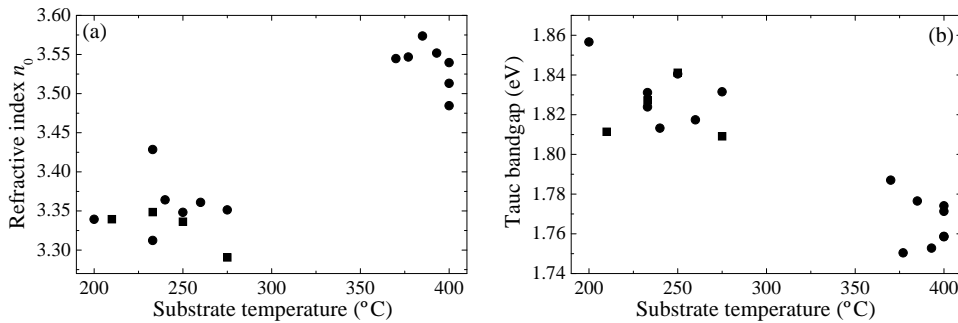


Figure 3.2: (a) Refractive index at zero energy n_0 and (b) Tauc bandgap as a function of the substrate temperature. Two different gas flow rates were used, namely 60 sccm (■) and 90 sccm (●).

130 °C was obtained. The effect of the external heater on the substrate temperature is small compared to that of the filaments. Two different gas flow rates were used, namely 60 and 90 sccm. The pressure was kept constant at 20 μ bar, similar to the optimum pressure Feenstra found at a substrate temperature of 430 °C [34].

For each of the deposition conditions, thin films (~ 150 nm) and thick films (~ 1 μ m) were deposited. Figure 3.1(a) shows the deposition rate of all these samples as a function of the substrate temperature. From this figure it is clear that two different regimes can be identified, which correspond to the temperature regimes in which the heater is off (200-275 °C) or on (370-400 °C). Within each of the two regimes, the deposition rate increases with increasing substrate temperature, and thus with the filament temperature. Therefore, figure 3.1(b) shows the deposition rate as a function of the filament temperature. Apparently, the use of the heater has hardly any influence on the deposition rate. Therefore, the deposition rate is dominated by the filament temperature.

For the thin films, the refractive index at zero energy, n_0 , and the Tauc bandgap are plotted as a function of the substrate temperature in figures 3.2(a) and 3.2(b), respectively. The refractive index increases from about 3.35 to 3.55 with increasing temperature, indicating that more compact material is deposited at higher (heater) temperatures. This can be explained by the surface mobility of the precursors, which is strongly dependent on the substrate temperature. At high temperature, the precursors can move over the surface and reach an energetically favorable position, resulting in more compact film growth. The Tauc bandgap increases with decreasing temperature.

The hydrogen concentration is plotted as a function of the substrate temperature in figure 3.3(a). It is clear that the hydrogen concentration increases from 8 at.% to about 15 at.% as the substrate temperature is decreased from 400 °C to 200 °C.

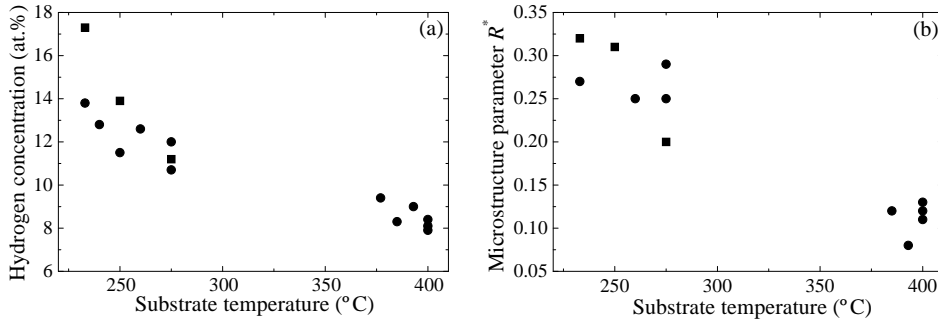


Figure 3.3: (a) Hydrogen concentration and (b) microstructure parameter R^* as a function of the substrate temperature. Two different gas flow rates were used, 60 sccm (■) and 90 sccm (●).

The microstructure parameter, shown in figure 3.3(b), also increases with decreasing temperature. This indicates that, when the temperature decreases, more hydrogen is present in SiH_2 - or SiH_3 -configurations, or on the inner surface of voids. Most other material parameters behave as expected for the hydrogen content. As an example, the ambipolar diffusion length, shown in figure 3.4(a), strongly depends on the temperature. For decreasing temperature, the diffusion length decreases, indicating a deterioration of the electronic quality of the material. Nevertheless, the photoconductivity and dark conductivity, shown in figure 3.4(b), show no dependence on the substrate temperature. It is also clear from this figure that material made at a silane gas flow rate of 90 sccm is better than that deposited at 60 sccm, as the dark conductivity improves (becomes lower) at this flow rate. It is possible that a difference in silane depletion for the two different gas flow rates plays a role in this, but no measurements were done to investigate this effect.

3.2.1 Role of hydrogen

From figure 3.3(a), it can be seen that the hydrogen concentration increases for decreasing substrate temperature. This effect is well known and can be explained by hydrogen incorporation during deposition. During film growth, the chemical potential of hydrogen (μ_H) in the gas phase and that in the deposited film are in equilibrium. The hydrogen in the film can be present in two different configurations: either in a deep trap, corresponding to a covalent silicon-hydrogen bond, or in a shallow trap, corresponding to a bond-centered or interstitial site [70]. This is illustrated schematically in figure 3.5. The chemical potential of hydrogen in the film can be described by

$$\mu_H = E_T + k_B T_{\text{sub}} \ln \frac{N_H}{N_T - N_H}, \quad (3.1)$$

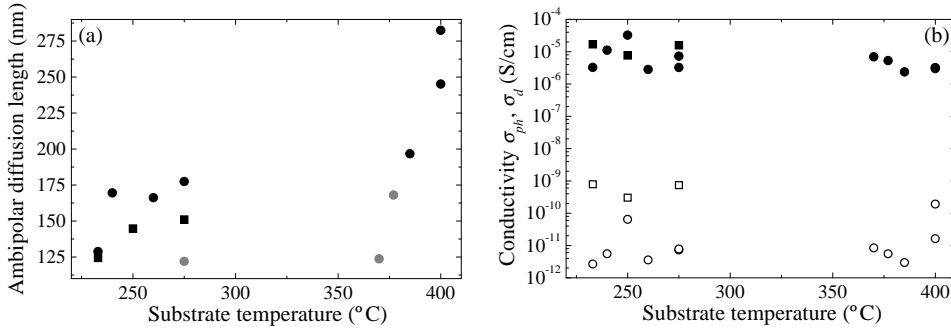


Figure 3.4: (a) Ambipolar diffusion length and (b) photoconductivity (closed symbols) and dark conductivity (open symbols) as a function of the substrate temperature. Two different gas flow rates were used, namely 60 sccm (■) and 90 sccm (●). The gray symbols will be discussed in section 3.2.2.

where E_T is the energy level of the deep traps, T_{sub} is the substrate temperature, N_H is the density of occupied deep states, and N_T is the total deep trap density. From this equation, it follows that the chemical potential of hydrogen increases with the substrate temperature. From the fact that the chemical potential of hydrogen in the gas phase and that of hydrogen in the film must be in equilibrium during film growth, it follows that the occupation level of the traps decreases for higher substrate temperatures. As a consequence, the bonded hydrogen content in the film is reduced at

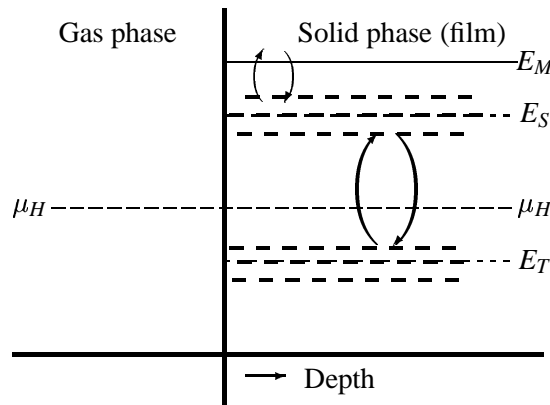


Figure 3.5: Schematic representation of the spatial distribution of hydrogen states in amorphous silicon [70]. E_M is the energy for mobile hydrogen. E_S and E_T represent the energy levels of the shallow traps and the deep traps, respectively.

elevated deposition temperature. Thus, a higher substrate temperature results in a lower hydrogen concentration in the film.

The hydrogen concentration has a large influence on the material properties of amorphous silicon. For PECVD samples, it is known that the optical bandgap is directly correlated with the hydrogen concentration. In figure 3.6, the Tauc bandgap is plotted as a function of the hydrogen concentration for PECVD samples, HWCVD samples made using tungsten filaments, and HWCVD samples made using tantalum filaments. In the case of PECVD, two different regimes can be identified. According to Meiling *et al.*, these regimes correspond to different morphologies of the material [71]. At low hydrogen concentrations ($\lesssim 11$ at.%) the bandgap increases linearly with the hydrogen concentration. The corresponding material is homogeneously structured, with a low hydrogen concentration. Hydrogen is present only in Si-H bonds, and there are no voids in the material. When the hydrogen content increases, the distance between the silicon atoms increases slightly. In this regime, the bandgap E_g correlates with the silicon interatomic distance. At higher hydrogen concentrations from 11 at.% up to ~ 20 at.%, the bandgap remains constant. The additional hydrogen atoms are not incorporated in isolated Si-H bonds. Rather, $(\text{Si-H}_2)_n$ -chains and voids are formed, which have no effect on the Si-Si bond density in the most-dense phase. As the optical bandgap is determined by the phase with the smallest bandgap, the bandgap is constant in this region.

For hot-wire deposited samples, Feenstra showed that, even for hydrogen concentrations as low as 1 at.%, the Tauc bandgap remains as high as 1.7 eV (see figure 3.6) [34]. This effect was attributed to the presence of microvoids in the material, which left the Si-Si bond density in the most-dense phase constant. As a result, the bandgap was constant. For amorphous silicon made at lower substrate temperature using tantalum filaments, the hydrogen concentration lies between 8 at.% and 15 at.%. For these samples, the microstructure parameter lies between 0.1 and 0.3, indicating that part of the hydrogen is bonded in SiH_2 -configurations or on the surfaces of microvoids. As a result, the corresponding Tauc bandgap remains high, with values between 1.75 eV and 1.86 eV. In figure 3.6, it can be seen that the hydrogen concentration in the layers is much too high to obtain a Tauc bandgap of ~ 1.65 eV.

3.2.2 Filament aging

As was already mentioned in section 2.1, aging of the filaments results in the formation of silicides on the filaments during hot-wire CVD [35]. These silicides will decrease the active area of the filaments and, due to the reactions with the tantalum, lead to brittleness of the filaments. As a consequence, the deposition rate decreases and the film quality may deteriorate. As the samples described in section 3.2 were deposited with a single set of filaments, these aging effects indeed took place. The last samples which were deposited showed a decreased deposition rate, and also the am-

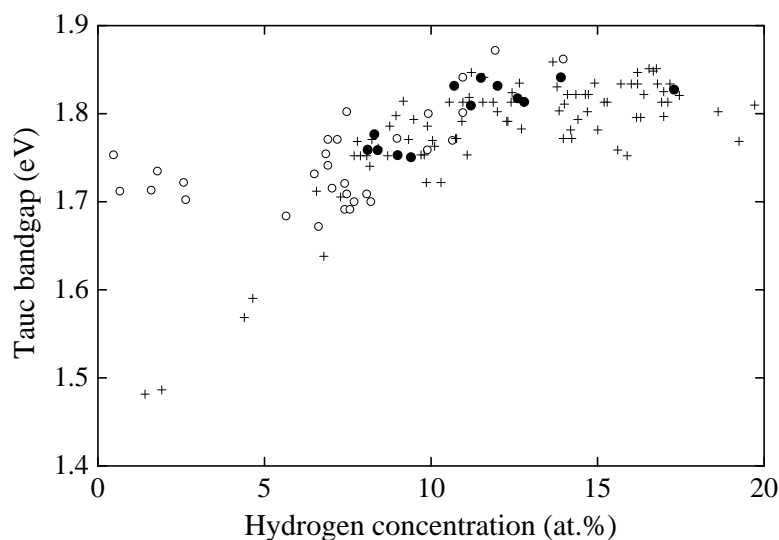


Figure 3.6: Tauc bandgap of amorphous silicon samples as a function of the hydrogen concentration. +: PECVD deposited samples, data from [71] and [34]; o: hot-wire deposited samples using tungsten as filament material [34]; •: hot-wire deposited samples using tantalum as filament material, data taken from figures 3.2(b) and 3.3(a).

bipolar diffusion length was smaller than could be expected. In figures 3.1 and 3.4(a), the data from these samples are indicated by gray symbols. Furthermore, the voltage necessary to keep the filament current constant goes up when the filaments age, indicating that the resistivity of the filaments increases during deposition. Unfortunately, as the filament age was not the only parameter which was varied in this deposition series, it is difficult to quantify the influence of the filament aging on the material properties. In section 3.3, a more systematic study of the dependence of the material properties of amorphous silicon on the filament age will be presented.

3.2.3 Epitaxial growth

An interesting result from the deposition series described in section 3.2 is the deposition of an epitaxially grown silicon layer on a (111) oriented crystalline silicon wafer. This epitaxial growth occurred at a filament current of 10.0 A (1800 °C), a substrate temperature of 370 °C, and a silane gas flow rate of 90 sccm. Raman measurements of this sample are shown in figure 3.7. A single crystalline peak at 520 cm^{-1} can be seen, while a layer deposited on adjacent Corning glass is fully amorphous. X-

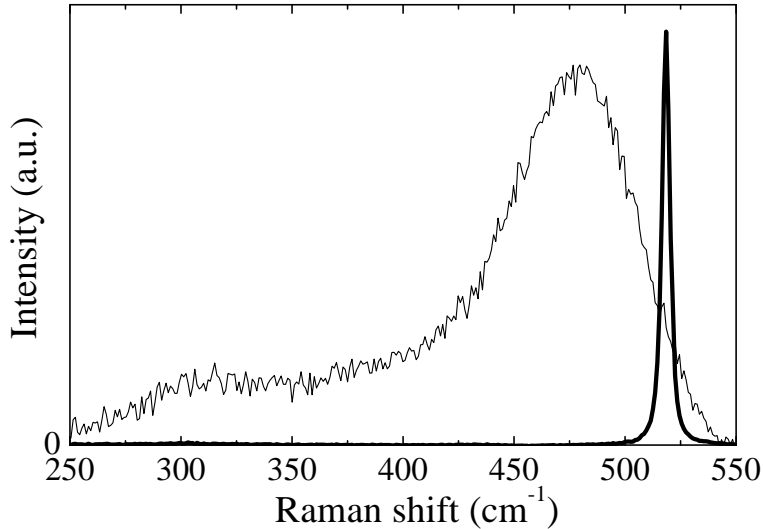


Figure 3.7: Raman spectrum of an epitaxially grown layer (thick line) and of a film deposited on adjacent Corning glass (thin line).

ray diffraction measurements revealed the silicon (111) diffraction peak around 30° , indicating the epitaxial nature of the film.

A cross sectional transmission electron microscope (X-TEM) micrograph of the epitaxially deposited silicon layer is shown in figure 3.8. From the TEM micrographs, it could be derived that the distance between the silicon crystal planes was 3.1 \AA , which corresponds well with the lattice spacing in the silicon (111) direction (see table 2.2). From other TEM photographs, it could be derived that the thickness of the layer is about 130 nm. Consequentially, the deposition rate of this layer was about 1 \AA/s , which is of the same order of magnitude as that found by others for hot-wire CVD [72]. It is clear that the filament age during deposition of this layer plays a role in the epitaxial nature of the deposition, as the epitaxial layer was the last sample of the deposition series, and the filament aging effects already deteriorated the material quality of amorphous samples deposited directly before. As was already shown in section 2.1, the radicals desorbed from an aged wire are expected to be different than those desorbed from a new wire. This change in radicals, along with a reduced growth rate, might cause epitaxial growth, but the mechanism for this is unclear. Furthermore, the filament temperature and substrate temperature were similar to that used for deposition of polycrystalline silicon with a high crystalline volume fraction [73]. Since it is not the main goal of this thesis, no further investigations on silicon epitaxial growth by HWCVD were performed.

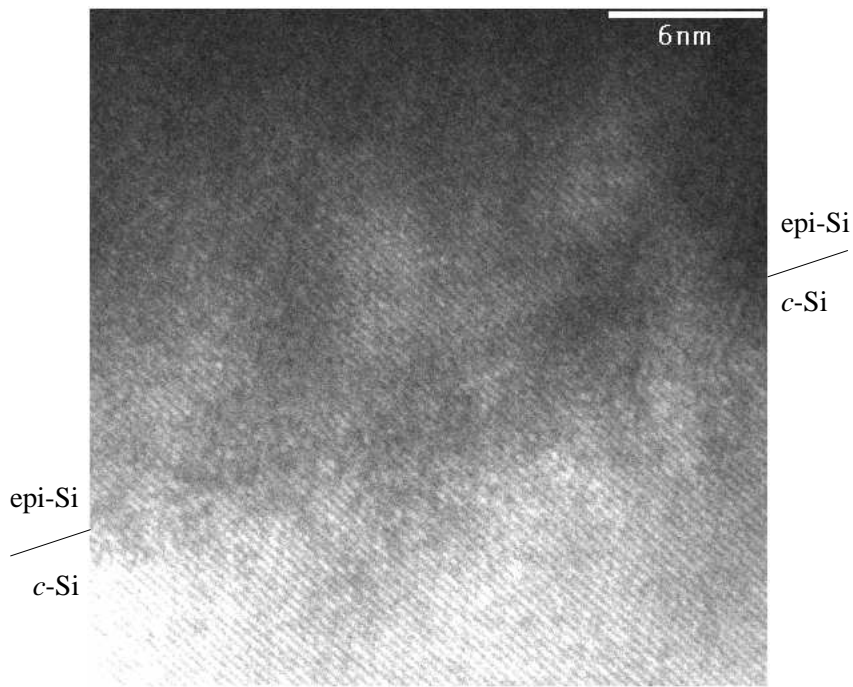


Figure 3.8: Cross sectional TEM micrograph of an epitaxially deposited silicon layer on a crystalline silicon wafer.

3.3 Influence of silicide formation

As was already indicated in the previous section, silicides can be formed on the filaments during deposition, which can have a significant effect on the material properties. Furthermore, the reduced active area of the filaments results in a decrease of the deposition rate. The reactions with the tantalum lead to brittleness and, eventually, breakage of the filaments. Also the electronic properties, like the ambipolar diffusion length, deteriorate. Although these effects are known to occur, only few research studies have been done to investigate their exact origin. Holt *et al.* discovered that aged wires show strikingly different radical desorption kinetics compared to new wires [41]. However, the effect of filament aging on the gas phase reactions and growth chemistry is not known. Mahan *et al.* measured the influence of tungsten filament alloying on the electronic properties of hot-wire deposited *a*-Si:H films [74] and found that the deposition rate and the ambipolar diffusion length decrease by about 50 % when filament aging takes place. Furthermore, aging effects are known to be stronger for tungsten filaments than for tantalum filaments [35], but no systematic investigations have been performed for the case of tantalum. In order to measure the influence of this tantalum silicide formation on the material quality a new series

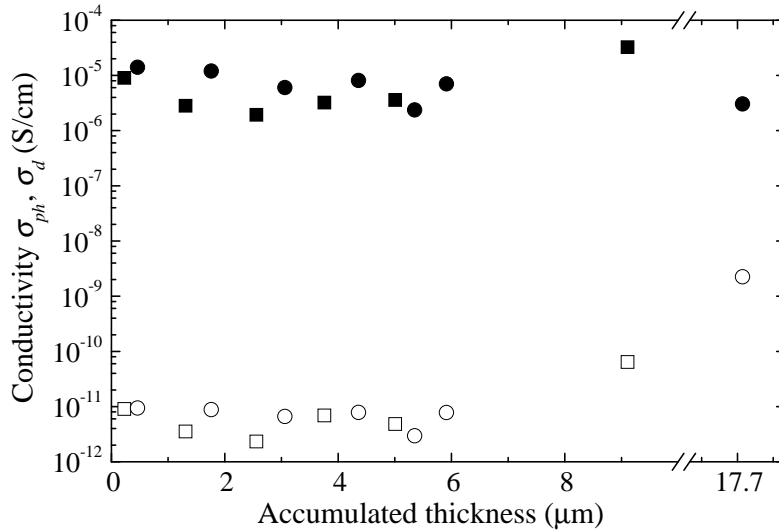


Figure 3.9: Photoconductivity (closed symbols) and dark conductivity (open symbols) of successively deposited amorphous silicon layers as a function of the accumulated thickness of all layers deposited by one set of tantalum filaments. Two different temperatures were investigated, namely 250 °C (■, □) and 370 °C (●, ○).

of films was made.

Figure 3.9 shows the photoconductivity and dark conductivity as a function of the total thickness of all silicon layers deposited by a single set of filaments. The substrate temperature during deposition was 250 °C, the silane gas flow rate was 90 sccm, and the deposition pressure was 20 μ bar. The filaments were preheated at 10.5 A (1850 °C) for at least 90 minutes to make sure that thermal equilibrium was reached. Under these deposition conditions, for the first 6 μ m of deposition there is hardly any influence of the filament age on the material properties. This can be seen from the the photoconductivity and dark conductivity, shown in figure 3.9. However, for accumulated thicknesses larger than 9 μ m, especially the dark conductivity starts to increase, indicating a deterioration of the material quality. Similar results are found for samples made at a substrate temperature of 370 °C. These results stress the necessity of the use of clean filaments for the optimization of the material properties of hot-wire deposited amorphous silicon.

Amorphous silicon made at 250 °C is interesting for device applications as it has a high photoresponse of 10^6 and a relatively high ambipolar diffusion length of 160 nm, in combination with a high growth rate of 10 Å/s. The filament current in this case is

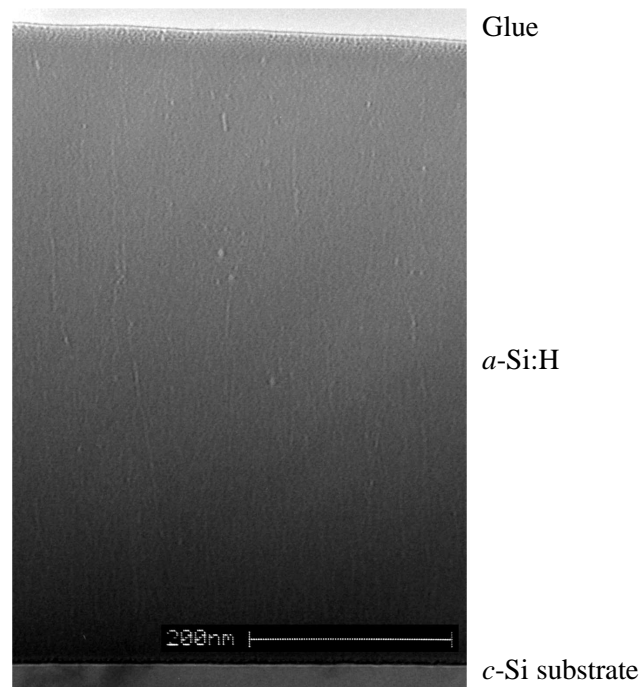


Figure 3.10: Cross sectional TEM micrograph of an amorphous silicon layer deposited at 250 °C, on a crystalline wafer substrate.

10.5 A, corresponding to a temperature of about 1850 °C for a new wire (measured in vacuum). A cross sectional transmission electron microscopy (X-TEM) photograph of an amorphous silicon layer deposited at 250 °C is shown in figure 3.10. Clearly visible are long inhomogeneities or voids in the direction of the growth, indicating that the layer is not fully compact. This agrees well with the high microstructure parameter of this material, which already indicated the presence of voids.

In figure 3.11, the absorption coefficient of this hot-wire deposited material is plotted as a function of the photon energy. Constant photocurrent method (CPM) measurements yielded an Urbach energy of 51 meV and a defect density of $1.3 \times 10^{16} \text{ cm}^{-3}$. However, photothermal deflection spectroscopy (PDS) measurements resulted in a higher defect density of almost 10^{17} cm^{-3} . These values of the defect density, as measured by PDS and by CPM, are comparable to those measured in *a*-Si:H deposited at high temperature. Apparently, the out-diffusion of hydrogen is not the only reason for the high defect density in high temperature amorphous silicon. A very thick layer of 20 μm , which was deposited at 250 °C, also showed a rather high defect density. This can be explained by silicide formation on the filaments during the long deposition time of this sample. As was seen before, the presence of these

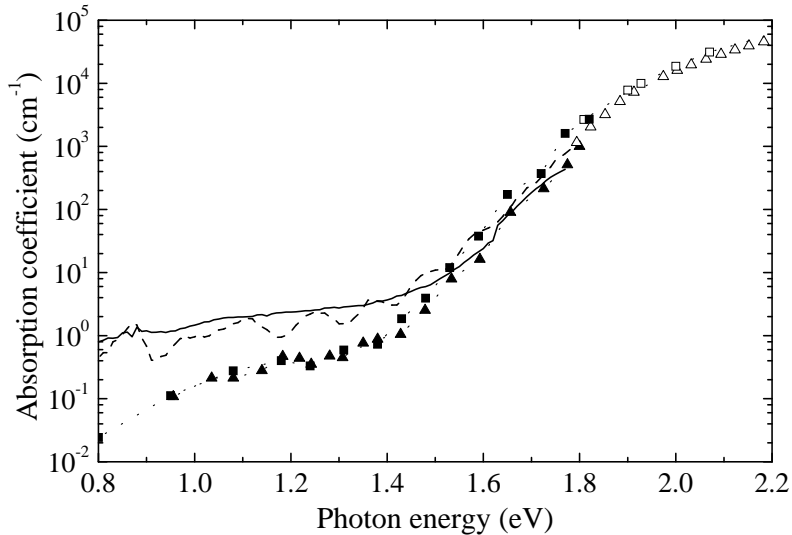


Figure 3.11: Optical absorption coefficient of hot-wire deposited amorphous silicon films deposited at 250 °C, compared to a device quality *a*-Si:H layer deposited by PECVD. Absorption data from reflection/transmission (R/T) measurements are used for calibration. ■: PECVD data, measured by CPM; □: PECVD data, measured by R/T measurements; ▲: HWCVD data, measured by CPM; △: HWCVD data, measured by R/T measurements; —: HWCVD data for a 1 μm thick sample, measured by PDS; - - -: HWCVD data for a 20 μm thick sample, measured by PDS.

silicides results in unoptimized deposition.

3.4 Deposition pressure

Further optimization of amorphous silicon was done in deposition chamber #5 of the PASTA system. To optimize amorphous silicon deposited at 250 °C, the influence of the deposition pressure on the material quality was investigated. The gas flow rate was kept constant at 90 sccm. At this gas flow rate, the lowest pressure that could be reached was 12 μbar. In figure 3.12 the deposition rate is plotted versus the pressure, for both thin (~ 150 nm) and thick (~ 1.0 μm) films. It is clear that the deposition rate is smaller for thin films than for thick films. This effect is most probably caused by the fact that amorphous silicon deposition does not start immediately after opening of the shutter. First, a certain surface roughness must evolve, after which actual deposition starts [75]. This surface roughness evolution takes a few tens of seconds.

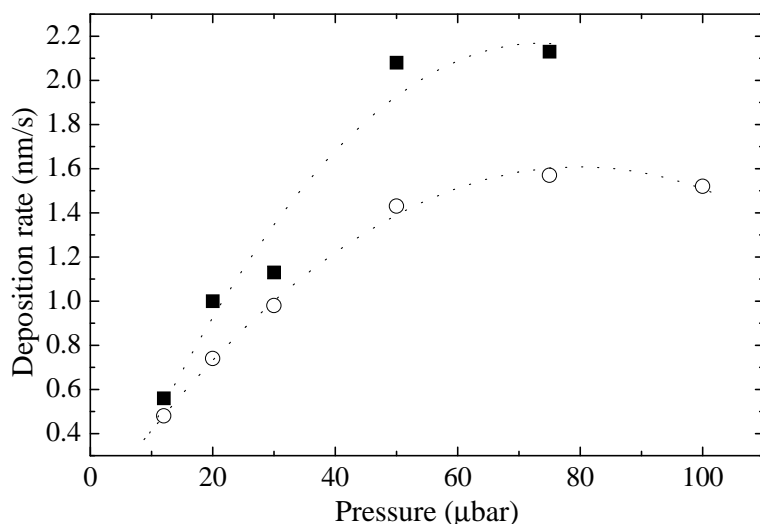


Figure 3.12: Deposition rate versus the pressure for both thin (○) and thick (■) amorphous silicon layers. The dotted lines are a guide to the eye.

As the deposition rate is equal to the total thickness of the layer divided by the time in which the shutter is open, the deposition rate is smaller for thin films. The behavior shown in figure 3.12 can be explained as follows: in the low pressure regime the number of silane dissociation reactions on the filament increases with increasing pressure, which leads to higher production of precursors. As the mean free path length is larger than the distance between the filaments and the substrate, this results in an increase in the deposition rate. At higher pressures, the number of collisions in the gas phase per unit of time increases, and this will finally lead to a limitation in the radical transport to the substrate, and thus in the deposition rate. Furthermore, at high pressure the silane supply to the filaments becomes limited, and this depletion also limits further increase of the deposition rate. In addition to these effects, the increasing number of silane dissociations per unit of time leads to the enhanced formation of silicides on the filaments. As was mentioned in section 3.3, this results in a decrease in the film growth rate. At high pressures ($\geq 50 \mu\text{bar}$) this effect was indeed observed. Unfortunately, the alloying of the filaments could not be completely reversed by annealing treatments and resulted in a permanently lowered deposition rate. To minimize this type of aging of the filaments, they were heated at 12.5 A (2020 °C) before each deposition so that silicon is evaporated from the alloyed filaments as much as possible. This preheating also has the advantage that the material quality is improved: the CPM defect density decreases from $1.3 \times 10^{16} \text{ cm}^{-3}$ to 0.3

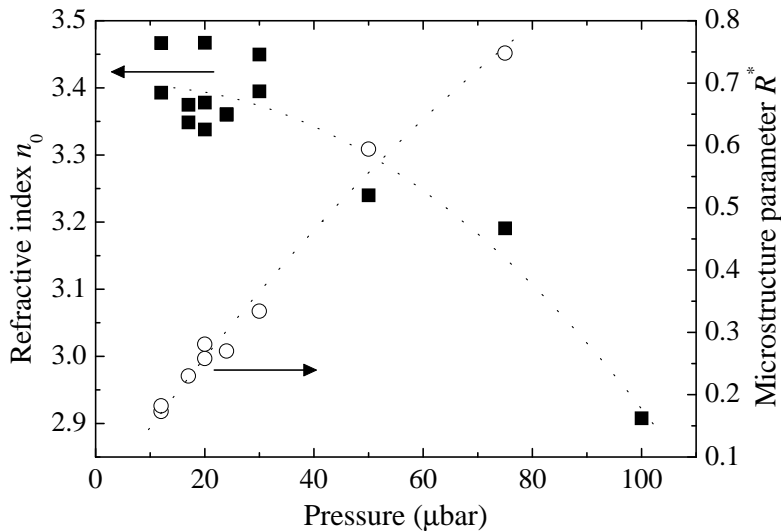


Figure 3.13: Refractive index n_0 (■) and microstructure parameter R^* (○) as a function of the pressure. The dotted lines serve as guides to the eye.

$\times 10^{16} \text{ cm}^{-3}$. Apparently, the presence of silicides on the wires has a large effect on the defect density in amorphous silicon.

The material quality and structure also depend on the deposition pressure. For low pressures, the mean free path length is larger than the distance between the filaments and the substrate. For instance, at a pressure of $5 \mu\text{bar}$, the mean free path length can be calculated to be in the order of 6 cm [76]. As this length is more than the distance between the filaments and the substrate (4 cm), hardly any reactions between gas phase radicals will take place before deposition. Therefore, atomic Si can be expected to be the main growth precursor in this pressure regime [24]. This radical has a high sticking coefficient (close to 1) [77], which results in a void-rich layer. If the pressure increases, the mean free path length decreases. When this length becomes comparable to the distance between the filaments and the substrate, collisions in the gas phase occur and precursors are created that are more mobile on the amorphous silicon surface (e.g. SiH_2 , SiH_3). As a result, the material quality is improved. At even higher deposition pressure, more gas phase reactions take place. Consequently, higher radical silanes are formed, which lead to less compact films of inferior material quality. Therefore, an optimum in the material quality is expected for a certain deposition pressure.

Figure 3.13 shows the refractive index n_0 and the microstructure parameter R^* as a function of the deposition pressure. It is clear that n_0 decreases with increasing

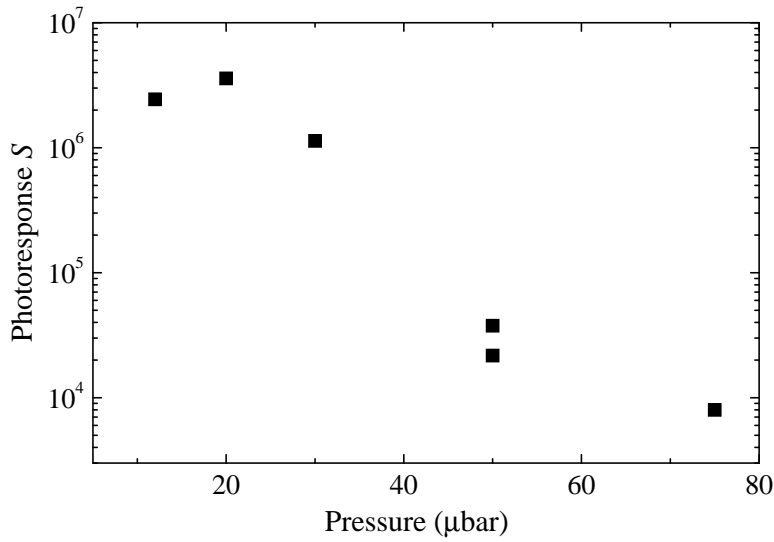


Figure 3.14: Photoresponse S versus the pressure.

pressure, indicating that the layers become less compact. This can also be seen from the microstructure parameter, which increases from 0.17 to 0.75 when the pressure is increased from 12 μbar to 75 μbar . This indicates that more bonded hydrogen is present in voids or in highly hydrogenated silicon groups (SiH_2 - or SiH_3 -groups). Even the sample made at a pressure of 12 μbar has a quite high microstructure parameter. Moreover, FTIR measurements on the layers deposited at a deposition pressure of 50 and 75 μbar reveal an increasing Si-O-Si peak around 1100 cm^{-1} , which provides further evidence for the porous nature of these layers made at high pressure. Figure 3.14 shows the photoresponse of the samples as a function of the deposition pressure. This parameter shows a maximum for deposition pressures around 20 μbar . At the same time, the defect density and the Urbach energy, as measured by CPM, show a minimum at 20 μbar . Clearly, optimal material quality is found at a pressure of 20 μbar . This value of the pressure p depends on the number of gas phase reactions per unit of time that occur during film growth, and is therefore dependent on the distance d_{f-s} between the filaments and the substrate. In other words, optimal amorphous silicon quality is found for values of $p \times d_{f-s}$ of approximately 8 Pa cm. This value corresponds rather well with those found by others [24, 78]. Results on the incorporation of this material in solar cells will be presented in chapter 4.

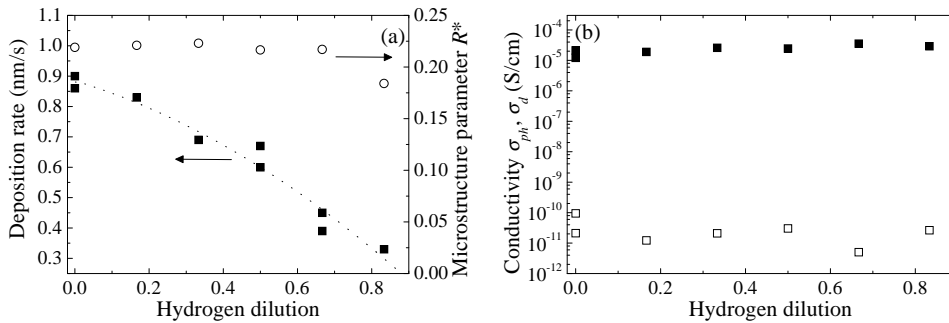


Figure 3.15: (a) Deposition rate (■), microstructure parameter R^* (○), and (b) photoconductivity (■) and dark conductivity (□) of amorphous silicon as a function of the hydrogen dilution.

3.5 Hydrogen dilution

The drawback of amorphous silicon deposited at 250 °C is that the microstructure parameter R^* is high (0.2-0.3), indicating that a lot of hydrogen is present on the inner surfaces of voids in the layers. This may result in a reduced resistance against photoinduced structural changes [64, 79].

Therefore, a new series of layers was deposited at 250 °C, in which the silane source gas was diluted with hydrogen. The total gas flow rate was kept at 90 sccm and the pressure at 20 μ bar. The deposition rate of these samples are plotted in figure 3.15(a) as a function of the hydrogen dilution $\Phi_{H_2}/(\Phi_{SiH_4} + \Phi_{H_2})$. The deposition rate decreases with increasing hydrogen dilution due to the smaller amount of silane gas present during deposition. The photoconductivity and dark conductivity are plotted in figure 3.15(b) as a function of the hydrogen dilution. These material parameters, and also most other parameters did not depend on the hydrogen dilution. However, at a hydrogen dilution of 0.833 an improvement in the structural order appeared. In figure 3.15(a), it can be seen that R^* decreased from about 0.25 to 0.18 at this hydrogen dilution, which indicates that this material can be more stable upon light-soaking. At this hydrogen dilution, the growth rate was about 0.33 nm/s. Raman measurements showed that these diluted silicon layers are still amorphous. The incorporation of this material in solar cells will be discussed in section 4.2.2. Also the stability of this material will be discussed in this section.

3.6 Deposition rate and bandgap variation

Although the material properties of hot-wire deposited amorphous silicon, made at a substrate temperature of 250 °C, are very promising for application in solar cells, dif-

ferent deposition conditions were also investigated. It is likely that a temperature of 250 °C is too high for application in *p-i-n* structured solar cells, as both the underlying TCO- and the *p*-layer may deteriorate. Therefore, several experiments were done to decrease the substrate temperature further and to increase the optical bandgap. This low-temperature, wide bandgap (WBG) material could well be applied as the top cell in multijunction solar cells. However, when lower filament temperatures are used, also the silicide formation on the filaments is enhanced. Therefore, a minimal filament current of 10.0 A (1800 °C in vacuum) was used, resulting in a substrate temperature of 220 °C. In this case, the deposition rate for undiluted amorphous silicon was 0.54 nm/s, and the Tauc bandgap was 1.84 eV. A high hydrogen dilution during deposition of 0.933 lowered the deposition rate to 0.12 nm/s, but increased the Tauc bandgap to 1.87 eV.

As the deposition rate of the low- and medium-temperature deposited hot-wire amorphous silicon is about 1 nm/s or lower, a different filament geometry can be considered to improve the deposition rate. High-rate deposition of amorphous silicon was investigated in chamber #4 using four wires instead of two. Tungsten was used as filament material, and the filament temperature was about 2100 °C. No external heating was used, resulting in a substrate temperature of about 400 °C. A deposition rate of 8.1 nm/s was obtained for a 1 μm thick sample, while the material properties deteriorated only slightly. The sample had a dark conductivity of 3×10^{-11} S/cm, and a photoconductivity of 1×10^{-5} S/cm. The hydrogen concentration of this layer was only 5 %. From this experiment, it is clear that the deposition rate can be increased by optimization of the filament geometry and of the filament conditions.

3.7 Conclusions

With the use of tantalum as filament material, a decrease in the *a*-Si:H deposition temperature during hot-wire CVD from 430 °C to 250 °C was obtained, while maintaining device quality material. By varying the deposition pressure, silane gas flow rate, and hydrogen dilution this material was optimized with respect to its (opto-)electronical characteristics. An overview of the material properties of different hot-wire deposited amorphous silicon layers is given in table 3.1. From this table, it is clear that the photoresponse improves greatly and the CPM defect density decreases when the substrate temperature is decreased from 430 °C to 250 °C, indicating a strong improvement in material quality. As the hydrogen concentration in the material is dominated by the substrate temperature during deposition, it is not possible to have a low hydrogen concentration at a low filament temperature or at a low deposition rate. Therefore, the optical bandgap of the material increases for lower substrate temperatures, and a Tauc bandgap of 1.8 eV is obtained at 250 °C.

Furthermore, it was shown that the filament history is a crucial parameter for

Table 3.1: Material properties of optimized hot-wire deposited intrinsic layers.

Material property	250 °C	250 °C	430 °C
	undiluted	0.833 diluted	undiluted
Filament material	Ta	Ta	W
Filament temperature (°C)	1850	1850	1900
Tauc band gap (eV)	1.8	1.85	1.7
Hydrogen concentration (at.%)	12-13	15	8
Microstructure parameter R^*	0.2-0.3	0.18	< 0.1
Dark conductivity σ_d (S/cm)	6.6×10^{-12}	2.6×10^{-11}	1.2×10^{-10}
Photoconductivity σ_{ph} (S/cm)	2.4×10^{-5}	2.9×10^{-5}	2.4×10^{-6}
Photoresponse S	3.6×10^6	1.1×10^6	2×10^4
Ambipolar diffusion length (nm)	160	150	170
Urbach energy (meV)	51	51	48
CPM defect density (cm^{-3})	1×10^{16}	2×10^{16}	3×10^{16}

material quality, as the presence of silicides on the filaments has a negative influence on the material properties of the deposited layer. The silicide formation resulted in significant decreases in the deposition rate and in the ambipolar diffusion length. For extreme silicide formation, even epitaxial growth was observed. By preheating the wires at elevated temperature before deposition, the influence of silicides was minimized.

The material properties of amorphous silicon deposited at 250 °C are better than those obtained at 430 °C. However, a substrate temperature of 250 °C might still be too high for application in, for instance, $p-i-n$ structured cells, as the underlying p - and/or TCO-layer may deteriorate at too high deposition temperatures of the absorbing layer. In the current configuration, it is not possible to decrease the substrate temperature much further, as the formation of silicides is enhanced at lower filament temperatures. Also, the decreased deposition rate at low temperatures is unwanted. It is shown that a different filament geometry, in combination with higher filament temperatures, can result in a strong increase of the deposition rate. However, as the filament temperature can have a large influence on the substrate temperature, high rate deposition at low temperatures will be a serious challenge. This situation can be improved by increasing the distance between the substrate and the filaments, but also the use of thinner wires, or a completely different catalyzer layout can have a positive effect.

4

Amorphous silicon solar cells

Hot-wire deposited amorphous silicon is an excellent material for incorporation as the absorbing layer in solar cells. Optimized material, deposited at 250 °C, was incorporated in efficient single- and multijunction solar cells on flexible stainless steel substrates. The n-i-p structure was used to show the beneficial effect of a low deposition temperature of hot-wire deposited intrinsic amorphous silicon for solar cells, as any degradation of the transparent conductive oxide layer and the p-doped layer, that is otherwise present in p-i-n structures, is avoided. The cells have a high open-circuit voltage (~ 0.9 V) and high fill factor (> 0.7), showing the improved performance of hot-wire deposited amorphous silicon made at moderate temperature. Application of the same material in tandem and p-i-n structured solar cells resulted in high open-circuit voltages and high fill factors.

4.1 Introduction

The hot-wire chemical vapor deposition (HWCVD) technique has proven to be a method for the deposition of high-quality silicon-based thin films and solar cells [21–24]. The high deposition rate, the possibility of depositing uniformly over a large area, and the low equipment costs, have made the HWCVD technique an attractive alternative for the commonly used plasma-enhanced chemical vapor deposition (PECVD) process. A disadvantage of the HWCVD technique is that device quality hydrogenated amorphous silicon (*a*-Si:H) has mainly been made at high deposition temperatures of over 350 °C [23, 24]. Since especially *p*-doped silicon layers deteriorate at such high temperatures [80], the hot-wire CVD process has mainly been applied for the deposition of *n-i-p* structured amorphous silicon solar cells [23]. For the application of the technique in *p-i-n* structures and multijunction solar cells, it is essential that the deposition temperature is lowered.

So far, only the University of Kaiserslautern has obtained high initial efficiencies for *p-i-n* solar cells [81], but without a comparison to *n-i-p* cells. Previously at Utrecht University, amorphous silicon deposited at 430 °C had been optimized for the incorporation in *n-i-p* cells. With a special thermally resistant *n*-layer [82] and a rehydrogenation procedure after *i*-layer deposition, the best cell had an initial efficiency of 5.5 %.

In this chapter, the influence of the deposition temperature of the absorbing layer or *i*-layer on the performance of *n-i-p* structured solar cells is studied. Unlike trans-

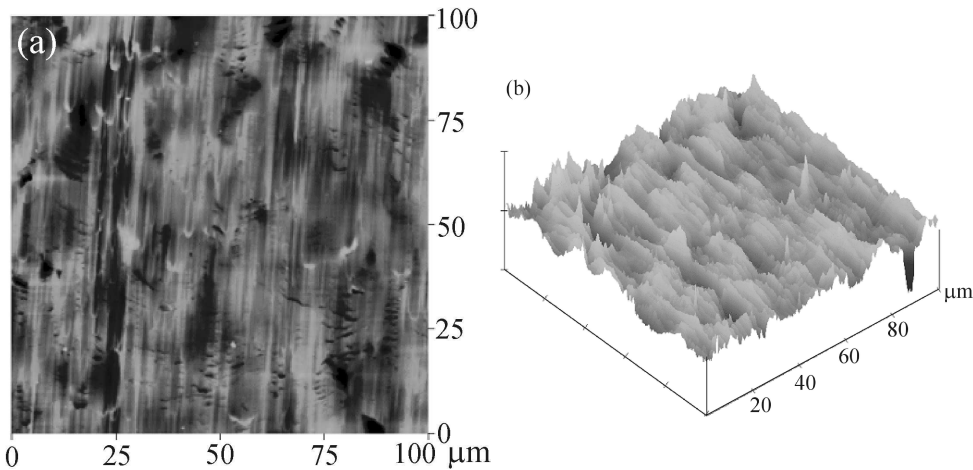


Figure 4.1: Atomic force microscopy (AFM) picture of (part of) a stainless steel substrate: (a) top view and (b) side view. The z -axis has a scale of 250 nm/div.

parent conductive oxide (TCO) and p -layers, the n -doped layer is, for deposition temperatures roughly below 450 °C, largely insensitive to changes in the deposition temperature of the absorbing layer [82]. Therefore, this study gives better insight in the correlation between the deposition temperature of the absorbing layer and the device performance. The application of moderate-temperature amorphous silicon in single-junction $n-i-p$ structured solar cells was examined and compared to the solar cells deposited at high temperature. Also, the application of this amorphous silicon in tandem solar cells and $p-i-n$ structured solar cells was investigated.

4.2 $n-i-p$ structured solar cells

4.2.1 Experimental details

Amorphous silicon was incorporated as the absorbing layer in $n-i-p$ structured solar cells. Flexible, unpolished, stainless steel (AISI 430) or (in a few cases) molybdenum was used as the cell substrate, with an area of $5 \times 10 \text{ cm}^2$. Before deposition, the substrates were ultrasonically cleaned with Deconex soap and isopropylalcohol. After this, they were rinsed with deionized water and subsequently dried with a nitrogen flow. As the substrates are unpolished, their surface is not smooth, and irregularities are present on the metal surface. Figure 4.1 shows an atomic force microscopy (AFM) picture of the surface of a stainless steel substrate. Curvatures originating from the rolling process, and also (sharp) irregularities can be seen. AFM pictures of a molybdenum substrate also revealed a large inhomogeneity, with an rms roughness

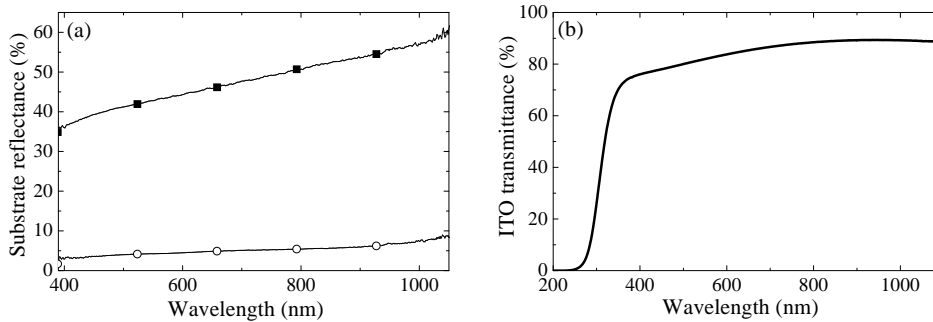


Figure 4.2: (a) Reflectance of stainless steel (■) and of molybdenum (○) as a function of the wavelength of the incident light. (b) Transmittance of an 80 nm thick indium-tin oxide (ITO) layer deposited on Corning 1737 glass as a function of the wavelength of the incident light.

roughly six times as high as that of a stainless steel substrate. In figure 4.2(a) the reflectance of the substrates is shown as a function of the wavelength. For molybdenum, the reflectance is low ($< 10\%$), but also the reflectance of stainless steel is not ideal with values of 40-60% in the visible and near-infrared regime. For the *n-i-p* structured solar cells investigated in this thesis no light absorption enhancement due to (textured) back reflectors or textured front surfaces was included.

The doped layers were deposited using PECVD at a discharge frequency of 13.56 MHz. The microcrystalline *n*-doped layer [83] was deposited at a substrate temperature of 200 °C and had a thickness of 50 or 80 nm*. A mixture of 2% phosphine (PH₃) in hydrogen was used as dopant gas. Details about the deposition of the *n*-layer are given in table 4.1. The absorbing *i*-layer was subsequently deposited using the hot-wire CVD technique. Between the *i*- and *p*-layer a thin buffer layer of low-temperature deposited amorphous silicon was deposited. This wide bandgap buffer layer ensures a short incubation phase for the 20 nm thick *p*-doped layer, and prevents back-diffusion of photogenerated electrons. The microcrystalline *p*-layer [84] is deposited at a substrate temperature of 160 °C, and has a thickness of about 20 nm. A mixture of 2% trimethylboron (TMB) and 1% silane in helium is used as the dopant gas and a high hydrogen dilution ($\Phi_{\text{H}_2}/\Phi_{\text{SiH}_4} = 200$) is used to obtain crystallinity. In table 4.1 also details of the deposition parameters of the *p*-layer are provided.

Indium-tin oxide (ITO) is used as the top electrode of the solar cell. This layer is deposited by reactive thermal evaporation of an indium-tin alloy in an oxygen atmosphere. The substrate temperature during ITO-deposition is 175-180 °C. Due to some inhomogeneity of the deposition, the thickness of the layer varies from about 90

*The *n*-layer thickness is measured on adjacent Corning glass.

Table 4.1: Deposition parameters of the PECVD deposited $\mu\text{c-Si:H}$ n - and p -layers applied in single-junction n - i - p structured solar cells.

Deposition parameter	n -layer	p -layer
Φ_{SiH_4} (sccm)	0.7	0.5
Φ_{H_2} (sccm)	100	100
$\Phi_{\text{PH}_3/\text{H}_2}$ (sccm)	0.6	—
$\Phi_{\text{TMB}/\text{SiH}_4/\text{He}}$ (sccm)	—	0.4
$T_{\text{substrate}}$ ($^{\circ}\text{C}$)	200	160
p (mbar)	0.99	1.1
r_d ($\text{\AA}/\text{s}$)	0.6	0.25

nm in the middle of the deposition to about 60 nm at the edges (measured on glass). In figure 4.2(b) the transmission of an 80 nm thick ITO-layer, deposited on Corning 1737 glass is shown. For wavelengths above 500 nm, the transmittance of the material is more than about 80 %. The sheet resistance of this material is typically $(150 \pm 30) \Omega/\square$. As these values are quite high for use as a solar cell electrode, silver or gold grid contacts were deposited on top of the ITO-layer to improve the conductivity. The ITO-layer defines the area of the solar cells. Unless indicated otherwise, the area of the n - i - p cells was equal to $4 \times 4 \text{ mm}^2$ (0.16 cm^2). For these cells, the area of the metal grid lines was 0.03 cm^2 , resulting in an active area of the cells, under illumination, of 0.13 cm^2 .

4.2.2 Results and discussion

Amorphous silicon layers made from either undiluted silane or hydrogen diluted silane (dilution = 0.833) were incorporated as the absorbing layer in n - i - p solar cells on stainless steel or (sometimes) on molybdenum substrates. The material properties of the intrinsic layers are given in table 3.1. An overview of the characteristics of the best solar cells is shown in table 4.2. In all cases, the best cells were made on a stainless steel substrate. The best undiluted cell has a very high open-circuit voltage (0.89 V) and fill factor (0.72), resulting in an initial efficiency of 7.2 %. Comparing this result with that obtained for cells with an absorbing layer deposited at $430 \text{ }^{\circ}\text{C}$, a large increase in efficiency was obtained. This improvement is mainly a result of a higher open-circuit voltage and a higher fill factor.

The best diluted cell, deposited at $250 \text{ }^{\circ}\text{C}$, also has a high open-circuit voltage of 0.87 V, but a lower fill factor. This is due to an unintentionally thinner absorbing layer, which was made at the end of the filaments usable life. Nevertheless, the initial efficiency of this cell is 5.8 %. When a relatively new filament was used for the deposition of the absorbing layer, the short-circuit current density was about

Table 4.2: Characteristics of the best *n-i-p* structured solar cells with a hot-wire deposited amorphous silicon absorbing layer.

Cell	$d_{i\text{-layer}}$ (nm)	V_{oc} (V)	J_{sc} (mA/cm ²)	FF	η (%)
250 °C undiluted	400	0.89	11.2	0.72	7.2
250 °C 0.833 diluted	200	0.87	9.8	0.68	5.8
430 °C [82]	400	0.79	12.1	0.57	5.5

10.5 mA/cm², which is comparable to the short-circuit current density of the best undiluted cell. From these results it is clear that the quality of the hot-wire deposited absorbing layers, made at 250 °C, is high. However, incorporation of *a*-Si:H layers deposited from undiluted silane results in a higher initial cell efficiency compared to layers made from hydrogen diluted silane. Unfortunately, the reproducibility of this performance turned out to be difficult, as many *n-i-p* structured cells occasionally showed shunting behavior. This issue was solved later, which will be discussed in chapter 5.

The external collection efficiencies (ECE) from spectral response measurements for *n-i-p* structured solar cells made from undiluted and hydrogen diluted silane are

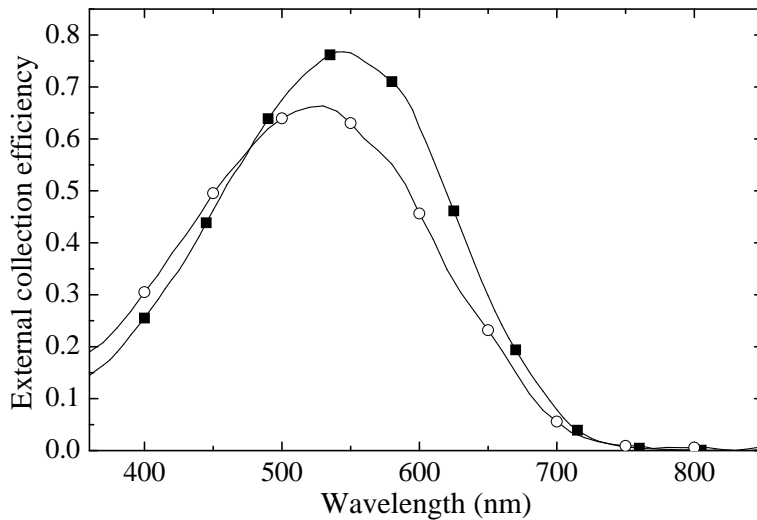


Figure 4.3: External collection efficiency of single-junction *n-i-p* structured solar cells made of undiluted silane (■) and of hydrogen diluted silane (○). Not all data points are shown individually.

shown in figure 4.3. For both cells, the collection efficiency is low in both the blue and the (infra)red regime. This will be discussed later in this chapter. The difference between the two cells in the green and red parts of the ECE spectrum can be attributed to the difference in thickness. The difference in the blue regime is most likely caused by a difference in the quality of the ITO-layers, which varies for different depositions runs.

From these results it is concluded that the quality of the hot-wire absorbing layers made at 250 °C is high. Comparing the results with those obtained for cells deposited at 430 °C, a large increase in efficiency at 250 °C was obtained. This is mainly the result of a higher open-circuit voltage and a higher fill factor. As can be seen from table 3.1, the photoresponse improves greatly and the CPM defect density decreases when the substrate temperature is decreased from 430 °C to 250 °C, indicating a strong improvement in material quality. Therefore, the difference in solar cell performance can be attributed mainly to the difference in material quality of the absorbing layer. In addition, an intrinsic layer deposited at 250 °C allows the use of conventional doped layers, while extra interface treatments are necessary at high temperature. These less stringent demands during deposition again indicate the advantage of the material deposited at moderate temperature. Figure 4.4 shows a cross sectional

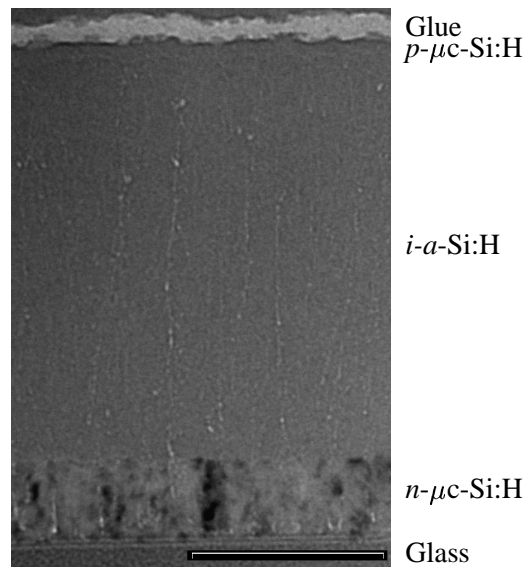


Figure 4.4: Cross sectional TEM micrograph of an amorphous silicon n-i-p structured solar cell, deposited on glass. The absorbing layer is deposited at 250 °C from undiluted silane gas. The scale bar corresponds to a length of 200 nm.

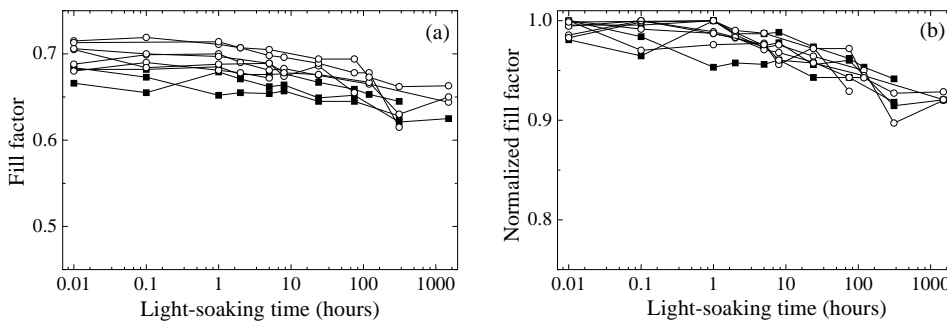


Figure 4.5: (a) Fill factor and (b) normalized fill factor as a function of the light-soaking time for single-junction $n-i-p$ cells in which the absorbing layer is made from undiluted silane (\circ) and hydrogen diluted silane (\blacksquare).

transmission electron microscopy (X-TEM) micrograph of a $n-i-p$ structured cell, where the intrinsic layer is deposited at 250 °C. Similar to figure 3.10, long voids can be seen in the direction of the growth of the amorphous silicon absorbing layer.

In order to investigate the stability of these single-junction solar cells against photoinduced changes, light-soaking experiments were performed. During these experiments, the temperature of the solar cells was about 45 °C, and the light intensity was about 100 mW/cm². Figures 4.5(a) and (b) show preliminary results of the fill factor and normalized fill factor of different $n-i-p$ structured solar cells, in which the absorbing layer is made at 250 °C. Both cells made from undiluted silane, and cells made from hydrogen diluted silane were investigated. The thickness of the intrinsic layers was 300-400 nm. From figure 4.5 it can be seen that the fill factor of both cells degrades by not more than 10 % after 1500 hours of light-soaking. As these values are rather low, it can be concluded that the cells have a high stability. Furthermore, hydrogen dilution does not have any influence on the stability of these solar cells. However, the initial parameters of the cells were not identical, which makes comparison between the cells difficult.

As the quality of amorphous silicon layers deposited from undiluted silane is high, these layers were also used in an $a\text{-Si:H}/a\text{-Si:H}$ $n-i-p/n-i-p$ configured tandem solar cell. A cross section of this tandem solar cell is schematically illustrated in figure 4.6. The doped layers of this tandem cell were similar to the ones described earlier in this section. However, the thicknesses of the doped layers in the tunnel recombination junction were different, as can be seen in figure 4.6. The tunnel-recombination junction consisted of an $n\text{-}\mu\text{c-Si:H}/\text{oxide}/p\text{-}\mu\text{c-Si:H}$ structure, which was similar to the tunnel-recombination junctions in $p-i-n/p-i-n$ structured solar cells [85]. The best cell has an open-circuit voltage of 1.70 V and a fill factor of 0.71. This open-circuit voltage has a value that agrees very well with the sum of the open-circuit voltage of

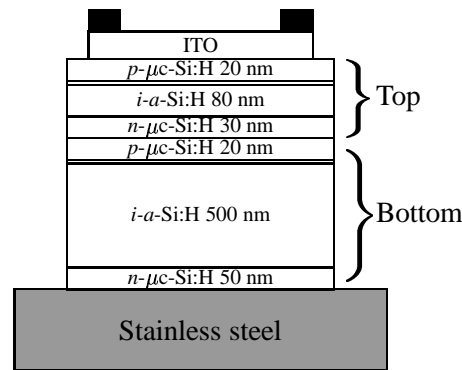


Figure 4.6: Schematic cross section of the *n-i-p/n-i-p* structured amorphous silicon tandem cell.

the single-junction amorphous silicon cell under AM1.5 illumination (~ 0.87 - 0.89 V) and of a slightly lower open-circuit voltage of the bottom cell. Also the fill factor is high, indicating that most photogenerated charge carriers are collected. The short-circuit current density measured (without a mask) is 7.1 mA/cm^2 , resulting in an initial efficiency of 8.5 %. The current density measured without a mask is 10-25 % higher than that measured with a light mask. Therefore, minimum values for the short-circuit current density and efficiency are 5.7 mA/cm^2 and 6.8 %, respectively. This corrected initial efficiency is slightly lower than the initial efficiency of a single-junction amorphous silicon cell (7.2 %), but this reduction can be expected based on losses in the tunnel-recombination junction.

Figure 4.7 shows the external collection efficiency of the best *a-Si:H/a-Si:H* tandem solar cell as a function of the wavelength, together with results from a single-junction *a-Si:H* solar cell. The top cell of the tandem cell generates a short-circuit current density of 5.6 mA/cm^2 , measured using red bias light. This value agrees very well with the (corrected) value obtained from current-voltage measurements under the solar simulator. According to the spectral response measurements, the bottom cell generates a total current density of 4.4 mA/cm^2 , which is only 77 % of the short-circuit current density of the total tandem cell. The origin of this difference will be discussed in more detail in chapter 8.

Comparing the total external collection efficiency of the tandem solar cell with that of the single-junction cell, it is clear that more blue light is absorbed in the tandem cell. This is caused by the thinner absorbing layer of the (blue-absorbing) top cell compared to that of the single-junction cell, resulting in a higher electric field and a higher current collection. On the other hand, green light ($\lambda = 500$ - 600 nm) is partly lost in the tandem cell due to the tunnel-recombination junction, resulting in a lower total current density.

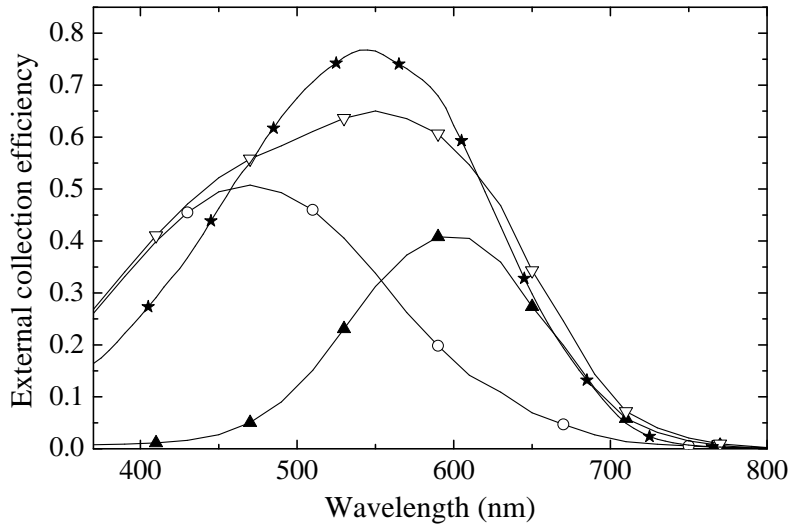


Figure 4.7: External collection efficiency of the best *a-Si:H/a-Si:H* *n-i-p/n-i-p* structured tandem solar cell. ○: Top cell, measured using red bias light, no bias voltage; ▲: bottom cell, measured using blue bias light, $V_{bias} = 0.91$ V; ▽: total. Also the external collection efficiency of a single-junction amorphous silicon *n-i-p* structured solar cell is shown (★).

4.3 *p-i-n* structured solar cells

The results on *n-i-p* structured solar cells, presented in the first part of this chapter, prove the device quality of hot-wire deposited amorphous silicon at moderate temperatures. Generally, *p-i-n* structured solar cells have a higher efficiency than *n-i-p* structured cells, due to the light scattering properties of the TCO front contact and better reflection at the back electrode, which is made of silver instead of stainless steel. However, care must be taken to ensure that the deposition temperature is low enough to avoid degradation of the TCO and/or *p*-layer. Amorphous silicon, deposited at moderate temperatures (220–300 °C), was incorporated in *p-i-n* structured solar cells. In order to measure the effect of the hot-wire deposition on the performance of *p-i-n* structured cells, different deposition conditions were used.

4.3.1 Experimental details

For the incorporation of hot-wire deposited amorphous silicon in *p-i-n* structured solar cells, Asahi U-type $\text{SnO}_2\text{:F}$ coated glass was used as the front contact of the solar cells. Silver grid lines were deposited on top of the TCO-layer. PECVD deposited

Table 4.3: Deposition parameters of the PECVD deposited a-Si:H *n*- and *p*-layers applied in single-junction *p-i-n* structured solar cells.

Deposition parameter	<i>n</i> -layer	<i>p</i> -layer
Φ_{SiH_4} (sccm)	40	30
$\Phi_{\text{PH}_3/\text{H}_2}$ (sccm)	10	–
$\Phi_{\text{TMB}/\text{SiH}_4/\text{He}}$ (sccm)	–	15
Φ_{CH_4} (sccm)	–	30
$T_{\text{substrate}}$ (°C)	200	160
p (μbar)	300	700
r_d ($\text{\AA}/\text{s}$)	0.7	2.0

wide band gap amorphous silicon carbide was used for the *p*-layer. This layer has a thickness of 9 nm. Details about the deposition parameters of the *p*-doped layer are given in table 4.3. On top of this *p*-layer, a buffer layer with a high bandgap is deposited to reduce electron back-diffusion [86]. As a consequence, the open-circuit voltage of the solar cells is increases. The intrinsic layer consists of hot-wire deposited amorphous silicon and has a thickness of about 500 nm. Before deposition of the absorbing layer, the filaments were preheated at about 2000 °C to evaporate as much silicon as possible from them. An amorphous silicon *n*-layer was used, which was deposited using the PECVD technique. This layer has a thickness of 20 nm. Details about the deposition parameters of this layer are also presented in table 4.3. Finally, highly reflective silver back contacts were applied, which define the area of the solar cells. Unless indicated otherwise, the area of the *p-i-n* structured cells was $4 \times 4 \text{ mm}^2$ (0.16 cm^2). The *p-i-n* structured cells were measured in a new automatic setup, and a reference cell was used to correct the solar simulator illumination for deviations from exact AM1.5 illumination. No mask was used to define the illuminated area, as this is usually not done for measurements of superstrate cells. This results in a small error (5-10 %) in the short-circuit current density and in the initial efficiency.

4.3.2 Results and discussion

Different amorphous silicon layers were incorporated as the absorbing layer in *p-i-n* structured solar cells. The substrate temperature during deposition of the absorbing layers was 300 °C, 250 °C, or 220 °C. As a deposition temperature of 300 °C is expected to deteriorate the *p*- or TCO-layer, in this case a buffer layer was incorporated between the *p*-layer and *i*-layer in order to protect the TCO-layer from (reactive) hydrogen radicals. For this purpose, a 5 nm thick hot-wire deposited amorphous silicon layer, made at 220 °C, was used. The substrate temperature of 220 °C during deposition is considered to be the minimum achievable temperature using the current

Table 4.4: Deposition parameters of the hot-wire deposited absorbing layers incorporated in *p-i-n* structured solar cells. Also the results of a PECVD deposited absorbing layer are given.

Absorbing layer	Φ_{SiH_4} (sccm)	Φ_{H_2} (sccm)	I_{fil} (A)	r_d (nm/s)
300 °C	90	0	11.5	1.5
250 °C	90	0	10.5	1.0
220 °C	90	0	10.0	0.54
220 °C WBG	6	84	10.0	0.12
PECVD 200 °C	40	0	—	0.24

deposition configuration, as silicide formation is greatly enhanced below this temperature and the material quality deteriorates strongly. Also the incorporation of wide bandgap (WBG) amorphous silicon made at high hydrogen dilution is investigated (see section 3.6). The deposition conditions of all absorbing layers are shown in table 4.4.

Figure 4.8(a) shows the current-voltage characteristics of the best *p-i-n* structured cells for each of the deposition conditions. Table 4.5 gives an overview of the corresponding cell parameters. Spectral response measurements were performed on all these solar cells. In figure 4.8(b) the external collection efficiencies of the different *p-i-n* structured solar cells are shown. From table 4.5 it can be seen that the deposition temperature has no significant influence on the open-circuit voltage of the solar cells. The solar cell deposited at a substrate temperature of 300 °C has a reduced fill factor.

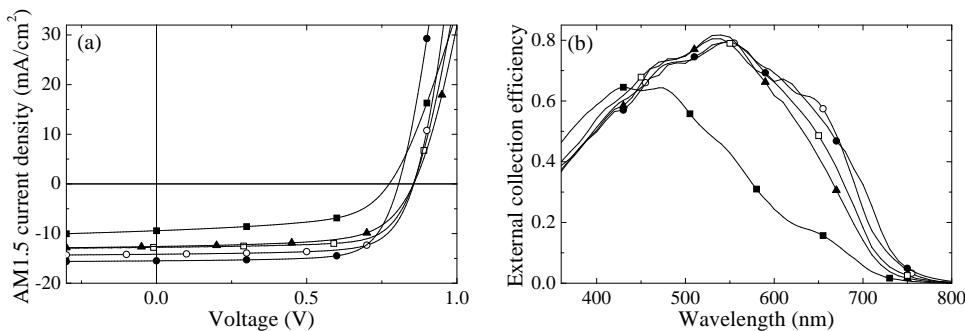


Figure 4.8: (a) Current-voltage characteristics and (b) external collection efficiency of *p-i-n* structured solar cells with a hot-wire deposited absorbing layer made at substrate temperatures during deposition of 220 °C (○), 250 °C (□), 300 °C (▲), and 220 °C WBG (■). For comparison, also the data of a PECVD deposited cell at 200 °C are shown (●).

Table 4.5: Characteristics of all *p-i-n* structured solar cells with a hot-wire deposited amorphous silicon absorbing layer. Also the results of a PECVD deposited reference cell are given.

Cell	V_{oc} (V)	J_{sc} (mA/cm ²)	FF	η (%)	R_s (Ω cm ²)	R_p (k Ω cm ²)
300 °C	0.85	12.6	0.65	7.0	7.4	1.0
250 °C	0.84	14.0	0.71	8.4	6.0	1.7
220 °C	0.86	14.2	0.71	8.6	4.9	1.8
220 °C WBG	0.78	9.4	0.56	4.1	12.1	0.44
PECVD 200 °C	0.81	15.5	0.72	9.0	4.5	2.0

Probably, the substrate temperature in this case is high enough to deteriorate the *p*- and/or the TCO-layer. Apparently, the application of a thin buffer layer between the *p*- and *i*-layer is not enough to protect the underlying TCO-layer. A too high substrate temperature may also be the reason for the slightly lower efficiency of the cell made at 250 °C compared to that made at 220 °C.

Unfortunately, the deposition rate of amorphous silicon, deposited at 300 °C, was lower than expected. Therefore, the cells made at 300 °C have a thickness of only 350 nm, which results in a lower red response, as can be seen in figure 4.8(b). For these cells, the short-circuit current density is rather low compared to that of the cell made at 220 °C. At this low temperature, the best cell has an efficiency of 8.6 %, which is comparable to the efficiency of a PECVD deposited reference cell. The PECVD deposited cell has a lower open-circuit voltage, but a higher short-circuit current density, which is the result of the lower bandgap (1.77 eV) of the absorbing layer material. This can also be seen from the external collection efficiency of the PECVD deposited solar cell, which is the highest in the red regime. Incorporation of wide bandgap (WBG) material in *p-i-n* structured cells results in a reduction of all cell parameters. Apparently, the high concentration of atomic hydrogen during deposition due to the high hydrogen dilution reduces the TCO-layer, resulting in bad solar cell properties.

The results on the incorporation of hot-wire deposited amorphous silicon as the absorbing layer in *p-i-n* structured solar cells again illustrate the high quality of the material. Similarly to *n-i-p* structured cells, it is possible to obtain high open-circuit voltages and high fill factors. However, the substrate temperature, and also the hydrogen dilution during deposition, must be kept low in order to minimize any effects of *p*-layer degradation or TCO reduction. Compared to *n-i-p* structured solar cells, the *p-i-n* solar cells have a higher short-circuit current density, which is mainly caused by the textured TCO-layer and the highly reflecting silver back reflector. Due to this texture, light is scattered in the cell and the optical path length is increased. As a result, the absorption of red light is increased, as is shown in figure 4.9. From this

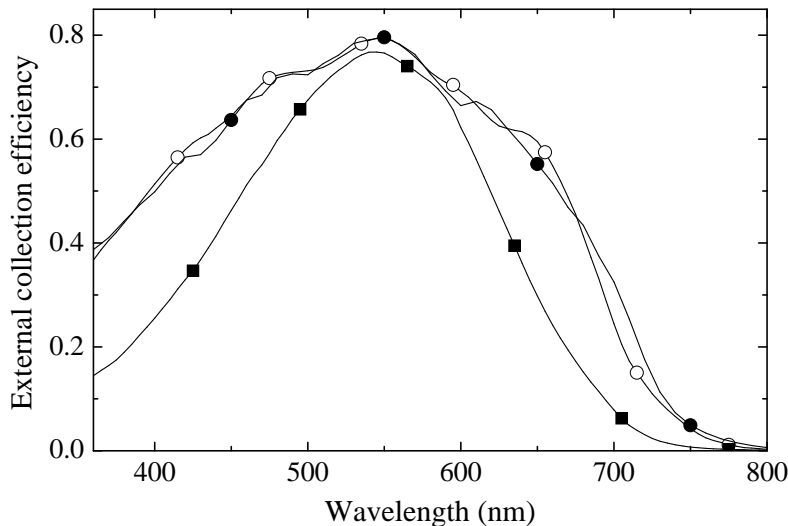


Figure 4.9: Comparison of the external collection efficiencies of the best hot-wire deposited *p-i-n* structured solar cell (○) and the best hot-wire deposited *n-i-p* structured solar cell (■). For comparison, also the data of a PECVD deposited cell at 200 °C are shown (●).

figure, it can also be seen that the blue response of *n-i-p* structured cells is very low. This is mainly caused by light absorption in the (microcrystalline) *p*-layer. From reflection/transmission measurements, Raman measurements and conductivity measurements, it is concluded that the microcrystalline silicon *p*-layer has only a very small crystalline ratio, indicating that the fraction of amorphous phase, and thus the absorption coefficient of blue light, is high. Furthermore, the influence of the ITO-deposition on the underlying *p*-layer is not known. As a result, optimization of the ITO/*p*- μ c-Si:H/*i*-a-Si:H structure is necessary to improve the *n-i-p* cell efficiency in the future. For the moment, the efficiency of *p-i-n* structured cells is therefore higher than that of *n-i-p* cells.

4.4 Conclusions

Amorphous silicon deposited at moderate temperature was incorporated as the absorbing layer in *n-i-p* structured solar cells. This cell structure was used to avoid the effect of variations in the *p*- and TCO-layer degradation, that are otherwise dominating upon variation of the *i*-layer deposition temperature in *p-i-n* device structures. The solar cells made showed a high open-circuit voltage and a high fill factor, which

resulted in a high initial efficiency. The best cell has an open-circuit voltage of 0.89 V, a fill factor of 0.72 and an initial efficiency of 7.2 %. This result is a clear improvement compared to the efficiency of solar cells incorporating a hot-wire deposited absorbing layer made at 430 °C. The results prove the device quality of amorphous silicon deposited at moderate temperatures by hot-wire CVD. Furthermore, the beneficial effect of a reduced deposition temperature of absorbing layers for incorporation in solar cells is demonstrated. Optimization of the ITO/ p - μ c-Si:H/ i -a-Si:H structure and the application of a highly reflective back contact are necessary to improve the n - i - p cell efficiency further.

As the results on n - i - p structured solar cells showed that high-quality materials and solar cells can be made using the hot-wire deposition method, the technique was also used for the deposition of absorbing layers in p - i - n structured solar cells. Again, high-quality solar cells were made, with high open-circuit voltages of about 0.86 V and fill factors of over 0.7. The best cell was made at a deposition temperature of 220 °C, and had an initial efficiency of 8.6 %. These results prove that no deterioration of the TCO and/or p -layer occurs, but care must be taken that the deposition temperature of the absorbing layer is kept below 250 °C, and that no high hydrogen dilution during deposition of the absorbing layer is used.

5

Shunting of hot-wire deposited amorphous silicon solar cells

Amorphous silicon solar cells, in which the absorbing layer is deposited using the hot-wire chemical vapor deposition technique, have potential advantages over solar cells made with the standard plasma-enhanced chemical vapor deposition technique. Although it is possible to make high-quality solar cells, many n-i-p structured cells occasionally show shunting behavior. Therefore, better control over the variation in cell performance must be obtained. In this chapter, it is proven that this behavior is directly correlated with the filament age and different successful methods for avoiding shunted cells and for improving the reproducibility of cell performance are presented.

5.1 Introduction

The hot-wire chemical vapor deposition (HWCVD) technique has proven to be a viable method for the deposition of high-quality amorphous silicon solar cells [23, 87]. Due to a high growth rate, which can be well over 10 nm/s [27], in combination with uniform deposition [88], this technique has major advantages over the commonly used plasma-enhanced chemical vapor deposition (PECVD) method. At Utrecht University, an initial efficiency of 7.2 % was recorded for an *n-i-p* structured cell on a flexible plain stainless steel foil, in which the absorbing layer was deposited using HWCVD [89]. Although this is a promising result, it turned out that the reproducibility of this performance was not straightforward. In addition, occasionally many cells show severe shunting problems. For eventual production purposes, it is necessary that both these problems are solved. Therefore, the purpose of this chapter is to clarify the origin of these shunting effects and, moreover, to present approaches for avoiding these effects.

5.2 Experimental details

All silicon layers and solar cells used in this study were deposited in the PASTA system [46], a multichamber high vacuum system. For the hot-wire depositions two straight tantalum filaments were used with a diameter of 0.5 mm and a length of 15

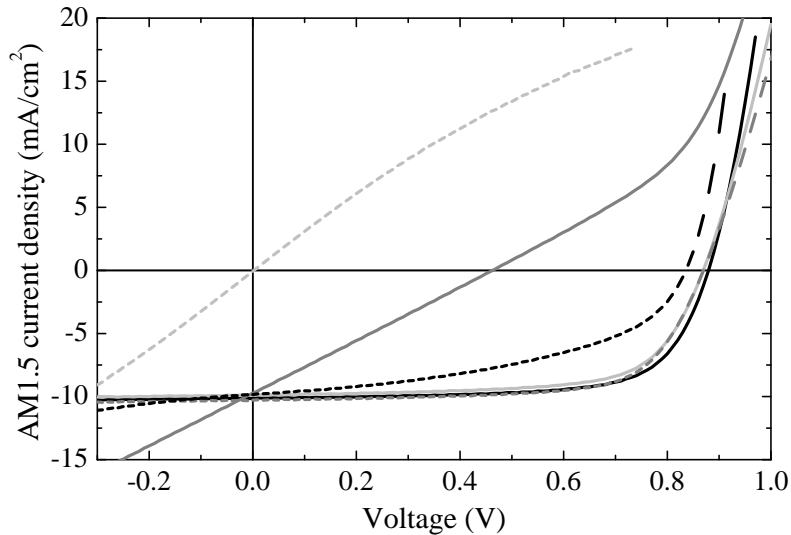


Figure 5.1: *J-V characteristics of several amorphous silicon single-junction $n-i-p$ cells under AM1.5 illumination.*

cm. These filaments were located parallel to each other at about 4 cm from the substrate. In all investigated $n-i-p$ structured solar cells in this chapter, hot-wire deposited hydrogenated amorphous silicon ($a\text{-Si:H}$), made at a temperature of 250 °C [89], was incorporated as the absorbing layer. Before deposition of the intrinsic layer, the filaments were heated at 1850 °C to make sure that thermal equilibrium was obtained. The influence of the filament aging was minimized by replacing the filaments early to avoid deterioration of material quality (see figure 3.9). The doped layers were made with the PECVD technique and are described in table 4.1. Unpolished, flexible, plain stainless steel was used as cell substrate. No textured layer or extra back reflector was used. The microcrystalline n -doped layer was deposited at a substrate temperature of 200 °C. The thickness of this layer was 50 nm. Between the i - and p -layer a thin buffer layer was applied, which ensures a short incubation phase for the microcrystalline p -doped layer. This p -layer was deposited at 160 °C and had a thickness of 20 nm. On most cells, indium-tin oxide (ITO) and silver or gold grid contacts were applied as the front electrodes. All $n-i-p$ structured cells had an area of 0.16 cm². The presence of the metal grid lines resulted in an active area of the cells of 0.13 cm² under illumination. However, on a few $n-i-p$ structures no ITO was deposited, but only silver contacts were deposited with an area of 0.16 cm². As a result, these structures could only be measured in the dark.

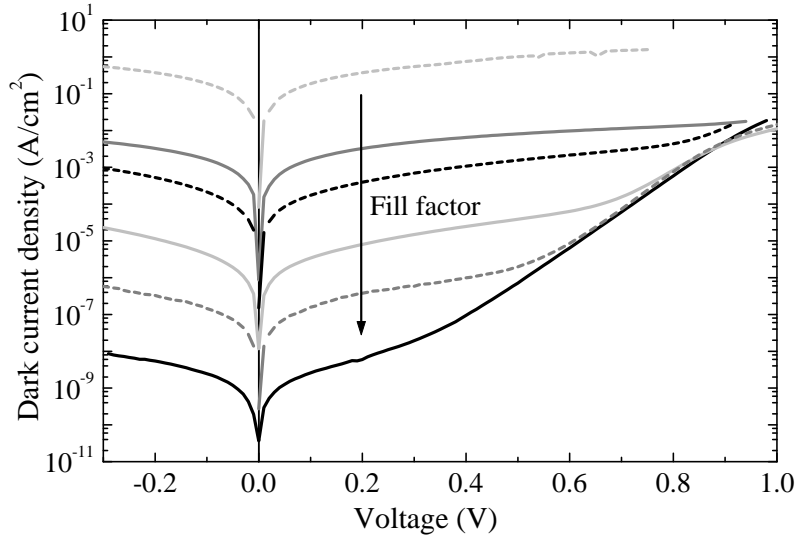


Figure 5.2: Dark J - V characteristics of the same amorphous silicon single-junction n - i - p cells as in figure 5.1. The arrow indicates the increase in fill factor when the cells are illuminated under AM1.5 conditions.

5.3 Results and discussion

In order to investigate the cell performances, AM1.5 and dark J - V characteristics of individual cells were measured. The cells were arranged in matrices on different samples, and each sample contained about 210 cells. The best of the cells that were made in this study had an open-circuit voltage of 0.89 V, a fill factor of 0.72, and an efficiency of 7.2 %. Figure 5.1 shows the J - V characteristics of several hot-wire deposited amorphous silicon cells under AM1.5 illumination. Figure 5.2 shows the dark J - V characteristics of the same cells. From these figures it can be seen that the cell behavior in the dark is directly correlated to the behavior under AM1.5 conditions. As was already explained in section 2.4.1, the current density $J(V)$ through an n - i - p device in the dark is given by

$$J(V) = J_0 (\exp [e(V - J(V)R_s)/nk_B T] - 1) + \frac{V - J(V)R_s}{R_p}. \quad (5.1)$$

In this equation, J_0 denotes the reverse-bias saturation current density, and n the diode ideality factor. R_p and R_s represent the parallel and series resistance, respectively. For high-quality amorphous silicon cells, J_0 should be in the order of 10 pA/cm². At low voltages, the cell behavior is dominated by the parallel or shunt resistance. From the solar cell characteristics shown in figure 5.1, it can therefore be concluded that

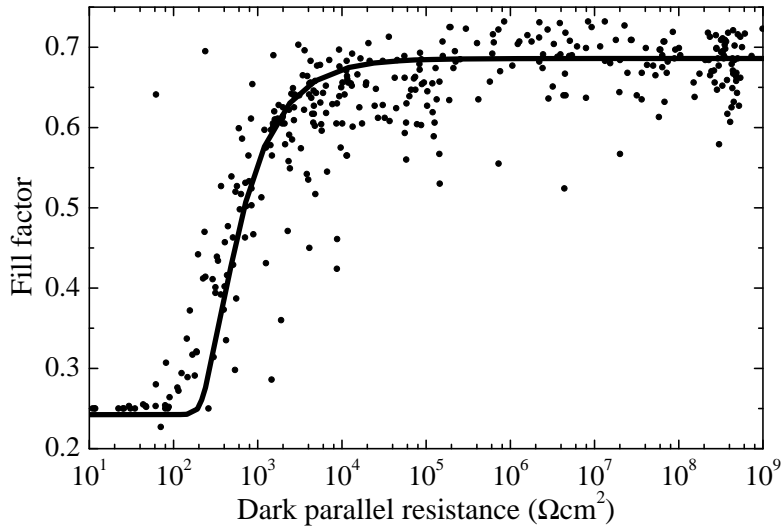


Figure 5.3: Fill factor as a function of the dark parallel resistance of several hot-wire deposited amorphous silicon *n-i-p* cells. The solid line is plotted as a guide to the eye.

the performance of these solar cells is correlated with the magnitude of the parallel resistance. The parallel resistance thus constitutes a critical figure of merit.

By fitting the measured dark *J-V* curves with the diode equation (5.1), values are obtained for J_0 , n , and R_p . In figure 5.3 the fill factor (*FF*) of many cells is plotted as a function of the dark parallel resistance. It is clear that a cell is completely short-circuited ($FF = 0.25$) when the dark parallel resistance is below $10^2 \Omega\text{cm}^2$, and that the fill factor saturates for values of the dark parallel resistance above $10^4 \Omega\text{cm}^2$.

In table 5.1 the yield of working hot-wire deposited cells is indicated, where the yield is defined as the percentage of cells having a dark parallel resistance larger than $10^4 \Omega\text{cm}^2$. The error in all values of the yield is estimated to be 5 %. From table 5.1 it is clear that there is a large spread in device performances, depending on the type of *n*-layer used. Hot-wire deposited solar cells with a conventional amorphous silicon *n*-layer, deposited at 200 °C, show zero yield. The use of a different, thermally stable, amorphous *n*-layer [82], did improve the yield, but a yield of 33 % is still too low for industrial applications. With a microcrystalline silicon ($\mu\text{c-Si:H}$) *n*-layer, occasionally relatively high yields of over 70 % were obtained. However, the reproducibility of this performance was not straightforward: the yield of different cell samples made in different deposition runs varied from 35 to 74 %, while the deposition conditions were the same.

Table 5.1: Yield of all *n-i-p* cells with a hot-wire deposited *a-Si:H* *i*-layer, but with different *n*-layers.

<i>n</i> -layer	Yield (%)
amorphous	0
thermally stable amorphous	33
microcrystalline	35-74

Several possible explanations for this effect were investigated. Firstly, unpolished stainless steel and molybdenum were used as cell substrate, and sharp irregularities are present on these metal, as was shown in figure 4.1. Layers which are deposited on top of such a metal peak do not have a uniform thickness, which might cause a shunting path through the solar cell. However, solar cells made on a flat substrate (Corning 1737 glass coated with a nickel-chromium alloy) also had a low yield. Therefore, the substrate roughness was not causing the shunting behavior.

A second effect that was investigated is that shunting behavior is normally associated with the presence of metal in the absorbing layer. In *n-i-p* structured cells the substrate is made of metal. Therefore, diffusion of metal from the substrate to the absorbing layer could be a reason for the shunts. However, the substrate temperature during the deposition of the hot-wire *i*-layer is only 250 °C, which is much too low for thermal diffusion. Moreover, the incorporation of a zinc oxide diffusion barrier between the metal substrate and the *n*-layer still resulted in a low yield of less than 30 %. Therefore, it can be concluded that metal diffusion from the substrate into the solar cell is not causing the shunting effect.

After extensive experimental investigations, it is concluded that the shunting effects can be attributed to aging of the filaments and not to the type of *n*-layer used. It is known that during hot-wire CVD silicides are formed on the filaments [35]. As a consequence, the filaments become brittle and their active area decreases, leading to a decrease of the deposition rate [74, 90]. Also the material quality of the deposited layer deteriorates as the filament age increases [74].

To confirm that indeed the filament age was responsible for the shunting of the solar cells, the filaments were preheated at elevated temperature (2020 °C) before deposition. As a consequence, silicon, which is present on the wires, is evaporated from the filaments. Indeed, the yield showed unprecedented high levels of 98 % when a microcrystalline silicon *n*-layer was used. In the case of an amorphous silicon *n*-layer the yield could even be increased from 0 % to 92 %. These huge differences between the yield with annealed filaments and that without annealed filaments are remarkable, as the differences in amorphous silicon material properties are small. With an unused filament, device quality material can be deposited even if the filaments are not preheated at elevated temperature before deposition (see section 3.3). However,

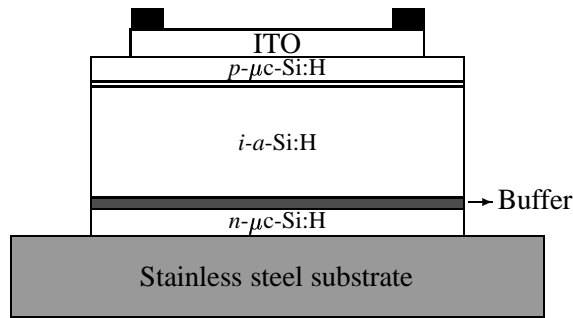


Figure 5.4: Schematic cross section of an *n-i-p* structured cell with a buffer layer. The dimensions are not to scale.

when this material is incorporated in solar cells, a yield of only 74 % is obtained. From table 5.1 it is clear that this yield decreases rapidly when an older filament is used, but no difference can be seen in material quality (see figure 3.9). Apparently, filament preheating at elevated temperature is crucial for the successful application of hot-wire deposited amorphous silicon in solar cells.

Another approach to improve the yield is to deposit a buffer layer between the *n*- and *i*-layer, as shown in figure 5.4. This buffer can act in two ways: it can avoid penetration in the *n*-layer from unwanted radicals, or it can act as an interface treatment to change the sticking probability of the radicals arriving at the surface. Different amorphous silicon buffers were used, deposited at 200 °C, either by PECVD at 13.56 MHz, or by HWCVD [81]. In table 5.2 the effects of the filament preheating and of the buffer layers are shown. From this table, it is clear that both methods consistently lead to a recovery of the yield to values that are a prerequisite for industrial production. For clarity, the effects of the buffer layer and of the filament preheating are illustrated in figure 5.5, in which the fill factor is plotted as a function of the par-

Table 5.2: Influence of the filament preheating and of the amorphous silicon buffer layer. A microcrystalline *n*-layer was used.

Cell	Yield (%)
Reference <i>a</i> -Si:H <i>n-i-p</i>	35-74
+ annealed wires (2020 °C)	98
+ PECVD buffer 1 nm	94
+ PECVD buffer 3 nm	95
+ PECVD buffer 5 nm	100
+ HWCVD buffer 3 nm + annealed wires	92
+ PECVD buffer 3 nm + annealed wires	91

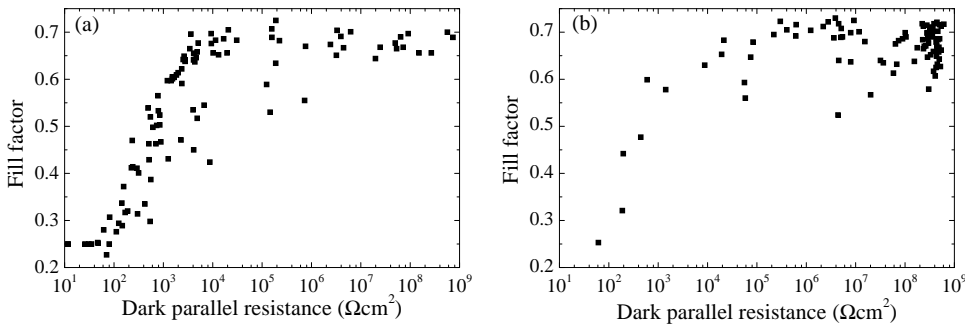


Figure 5.5: Fill factor as a function of the dark parallel resistance of simultaneously deposited *n-i-p* solar cells incorporating hot-wire deposited amorphous silicon made at 250 °C. (a) No buffer layer or filament preheating was applied. The yield is 35 %. (b) A 3 nm thick HWCVD buffer layer was incorporated, and the filaments were preheated at elevated temperature before deposition. The yield is 92 %.

allel resistance for cells with a low yield and cells with a high yield. In table 5.2 it can be seen that even a buffer layer with a thickness of 1 nm has a positive effect on the yield of working solar cells. As it is unlikely that such a thin buffer can act as a barrier against penetration of unwanted radicals, the beneficial effect of the buffer is caused by the changed surface. As a result, the sticking coefficient of adverse radicals changes.

Still, it is unclear what the exact cause of the shunting behavior is. From figure 4.4, it is clear that the absorbing layer contains long voids in the growth direction. It is possible that these voids can form a shunting path if their size is comparable to the thickness of the absorbing layer. Furthermore, it is possible that the density and the shape of these voids depends on the filament age, as a difference in growth radicals can result in a change in layer structure. This assumption can explain the dependence of the yield on the presence of silicides on the filaments. The role of the buffer layer in this case is, however, more difficult to understand. A possibility is that the formation of the voids is retarded by the changed growth surface due to the buffer layer. As a result, the shunting path can be shorted, resulting in an increase in the yield of working cells. The exact influence of the filament age or of the nature of the growth surface on the shape and density of the voids is not known and is still under investigation.

Filament preheating has also proven to be beneficial for the quality of *p-i-n* structured solar cells. When the filaments were not preheated at elevated temperature before deposition, the best cell had an open-circuit voltage of only 0.77 V, and a fill factor of 0.53. For this cell, the series resistance and parallel resistance were 12 Ωcm^2

and $0.49 \text{ k}\Omega\text{cm}^2$, respectively. The resulting initial efficiency was only 5.5 %. The results of a similar *p-i-n* structured solar cell, for which the filaments were annealed before deposition, are presented in table 4.5. In this case, the open-circuit voltage was improved to 0.85 V, and an enormous increase was found in the fill factor (0.71), resulting in an efficiency of 7.7 %.

5.4 Conclusions

In this chapter, it is shown that using the hot-wire CVD deposition technique the reproducibility of high-quality *n-i-p* cells can be difficult due to shunting problems. Similar behavior was seen for *p-i-n* structured cells. The shunting problems were directly correlated with the filament age during deposition. As known from literature [41], the presence of silicon on the filaments induces a change in radical species coming from the wires. As a consequence, the material quality of the deposited layer deteriorates [74, 89], which can explain the shunting effect. By preheating the wires at elevated temperature before deposition, the silicon was evaporated from the wires as much as possible, and the percentage of shunted cells was greatly decreased. Also by using a thin *a*-Si:H buffer layer between the *n*- and *i*-layer, the yield was increased to values well over 90 %. Because even the thinnest (1 nm) buffer layers showed this effect, it is unlikely that the buffer layer acts as a barrier layer against penetration of unwanted radicals. Therefore, it can be concluded that the drastic increase in the performance of the solar cells using a buffer layer is due to a change in sticking probability of adverse radicals to the changed surface. However, the exact nature of these radicals is unknown and is still under investigation. The shunting problems may be related to the presence of elongated voids in the material, which can act as a current leakage path. The results stress the importance of avoiding silicide formation on the filaments when optimizing hot-wire deposited amorphous silicon solar cells.

6

Polycrystalline and microcrystalline silicon

*In this chapter, the material properties of hot-wire deposited microcrystalline silicon are presented. Compared to polycrystalline silicon, microcrystalline silicon can be made at a much lower deposition temperature, but the structural properties and the bandgap of the materials are significantly different. The influence of the hydrogen dilution during deposition of microcrystalline silicon layers on the material and solar cell quality was investigated. Optimal material properties were found for material made close to the transition from the microcrystalline to the amorphous regime. An initial efficiency of 4.8 % was obtained for an *n-i-p* structured cell on untextured stainless steel, which is a clear improvement compared to the best polycrystalline cell.*

6.1 Introduction

In recent years, the hot-wire chemical vapor deposition technique has turned out to be a high-quality method for the deposition of silicon-based thin films. Advantages of this deposition technique are the high deposition rate, and the possibility to deposit uniformly over large areas. Previously, device quality amorphous silicon was found in the moderate temperature regime (250 °C), and efficient solar cells have been made with this material [89].

The combination of amorphous silicon and a narrow bandgap material in a tandem solar cell could result in a considerable increase in the energy conversion efficiency of thin-film solar cells. Possible narrow bandgap materials are hydrogenated microcrystalline silicon ($\mu\text{c-Si:H}$) and polycrystalline silicon (poly-Si). As these materials have an indirect bandgap, the layers must be several micrometers thick in order to obtain sufficient absorption in the red part of the solar spectrum. Therefore, the deposition of poly-/microcrystalline silicon at a high growth rate, while maintaining high material quality, is a key issue for industrial application. The hot-wire chemical vapor deposition technique would be an excellent choice for the fast deposition of these narrow bandgap materials.

In this chapter, results on hot-wire deposited polycrystalline silicon and microcrystalline silicon are discussed. Polycrystalline silicon is a material with a crystalline fraction of over 95 %, and a bandgap of 1.1 eV. Previously, incorporation of this material in a single-junction *n-i-p* solar cell resulted in an initial efficiency of 4.41 % [36].

However, as this material is deposited at high temperatures (~ 500 °C), the choice of substrates is limited. Therefore, also the material properties of hot-wire deposited microcrystalline silicon are investigated. Microcrystalline silicon can be deposited at much lower temperature (250 °C), but the material has a significantly different structure and bandgap compared to polycrystalline silicon. The influence of several deposition parameters on the microcrystalline silicon material quality was measured. In this chapter, results on the material properties of microcrystalline silicon will be presented. Furthermore, the application of microcrystalline silicon as the absorbing layer in solar cells will be discussed and compared with results on polycrystalline silicon.

6.2 Polycrystalline silicon

Hot-wire deposited polycrystalline silicon is a highly crystalline material, with a bandgap of 1.1 eV. The material is made at high substrate temperature during deposition (~ 500 °C), using two tungsten filaments. Deposition of this material is done in chamber #4. Two main types of polycrystalline silicon exist: one with randomly oriented small crystals (*Poly1*) and the other with columnar (220) oriented crystals, with a thickness dependent texture (*Poly2*). *Poly1* is deposited using a high hydrogen dilution of the silane gas. This material does not show any incubation phase, but the deposition rate of this material is only about 1 Å/s. *Poly2* is deposited using a lower hydrogen dilution of the silane source gas, at a much higher deposition rate of 5-10 Å/s. However, *Poly2* shows an incubation layer before nucleation with a thickness in the order of 50 nm. For the polycrystalline material used in solar cells, a profiled layer is deposited, which consists of a 15 nm thick layer of *Poly1* with *Poly2* on top of this. As a result, the crystalline volume fraction of the entire structure is larger than 90 %. Figure 6.1 shows an X-TEM micrograph of such a profiled *Poly1/Poly2*-layer. Application of a profiled polycrystalline silicon layer in an *n-i-p* structured cell resulted in an initial efficiency of 4.41 % [36]. This cell has an open-circuit voltage of 0.365 V, a short-circuit current density of 19.9 mA/cm², and a fill factor of 0.61. There are several reasons why the efficiency of this device is limited. Firstly, the value of the open-circuit voltage is rather low, which is caused by recombination of charge carriers at the grain boundaries and in the *Poly1*-layer, which has a high defect density. Secondly, cracks in the *n*-layer are present, as observed by X-TEM [91]. These cracks are probably caused by thermal stress due to the large difference in deposition temperature of the *n*-layer (200 °C) and of the absorbing layer (~ 500 °C). It is likely that these cracks affect the cell parameters negatively. Furthermore, the polycrystalline silicon absorbing layer is deposited at high temperature (~ 500 °C). As there is no diffusion barrier between the stainless steel substrate and the *n*-layer, impurities such as chromium diffuse from the substrate into the *n*-layer, as observed by X-ray

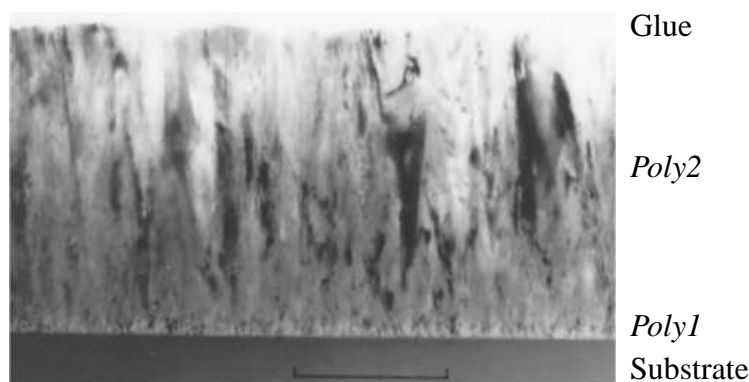


Figure 6.1: X-TEM micrograph of a profiled Poly1/Poly2-layer on glass. The length of the scale bar corresponds to 500 nm. Micrograph taken from [91].

photoluminescence spectroscopy (XPS). Finally, the lack of a back reflector results in a low red response. Another disadvantage of the high deposition temperature of polycrystalline silicon is the limitation in the choice of substrates.

A big advantage of polycrystalline silicon is the narrow bandgap, which results in a high red response of solar cells when a highly reflecting back reflector is included. Due to this high red response, polycrystalline silicon seems to be a good choice for the absorbing layer of the bottom cell of a multijunction solar cell. Unfortunately, the material is difficult to reproduce, and optimization of this material was in conflict with other depositions done in chamber #4. Therefore, the deposition of a different narrow bandgap material was investigated, namely microcrystalline silicon.

6.3 Microcrystalline silicon

Microcrystalline silicon is a two-phase material, in which crystalline regions are embedded in an amorphous matrix. In contrast to polycrystalline silicon, the material can be made at much lower deposition temperature. However, the materials have a significantly different structure and bandgap. In this section, results on the material and solar cell properties of hot-wire deposited microcrystalline silicon are presented.

6.3.1 Experimental details

All microcrystalline silicon layers were deposited in chamber #5, and tantalum was used as the filament material. As a substrate temperature of 250 °C during deposition turned out to be the optimal temperature for the deposition of amorphous silicon and its incorporation in solar cells [89], this temperature was also used for the deposition of intrinsic microcrystalline silicon. The filament temperature in this case was 1850

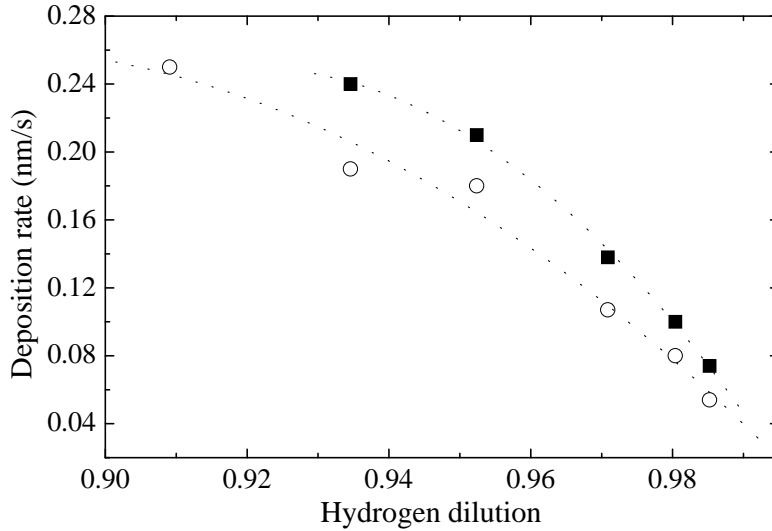


Figure 6.2: Deposition rate as a function of the hydrogen dilution for both thin (○) and thick (■) microcrystalline layers deposited at 250 °C. The dotted lines are plotted as a guide to the eye.

°C (measured in vacuum for virgin, annealed, filaments). Microcrystalline silicon was obtained by diluting the silane gas with hydrogen during deposition. The hydrogen dilution is defined as $\Phi_{\text{H}_2}/(\Phi_{\text{SiH}_4} + \Phi_{\text{H}_2})$. The pressure during deposition was kept constant at 50 μbar . Microcrystalline layers were characterized using thickness, optical, and electronic measurements, Fourier-transform infrared (FTIR) spectroscopy and Raman spectroscopy. The crystalline ratio R_c of the materials was calculated via $R_c = (I_{520} + I_{510})/(I_{520} + I_{510} + I_{480})$, where I_x is the integrated Gaussian corresponding to mode x in the Raman spectrum.

Optimized microcrystalline silicon was incorporated as the absorbing layer in n - i - p structured solar cells. Flexible, unpolished stainless steel foils were used as cell substrates. No back reflector was used. The doped microcrystalline layers were deposited using PECVD and are described in section 4.2.1. Indium-tin oxide (ITO) and gold grid contacts were deposited on top of the p -layer as the top electrodes. The solar cells were characterized by current-voltage and spectral response measurements. The cells have an area of 0.16 cm^2 , but the presence of the metal top contacts results in an active area of 0.13 cm^2 under illumination.

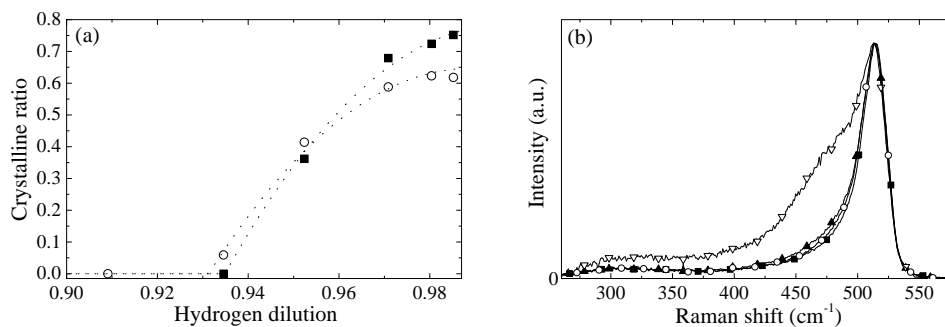


Figure 6.3: (a) Crystalline ratio R_c as a function of the hydrogen dilution for both thin (\circ) and thick (\blacksquare) microcrystalline layers deposited at 250 °C. The dotted lines are plotted as guides to the eye. (b) Raman shift spectra of different thick $\mu\text{c-Si:H}$ layers made using hydrogen dilutions of 0.985 (\blacksquare), 0.980 (\circ), 0.971 (\blacktriangle) and 0.952 (∇). The spectra are normalized with respect to their maximum (around 515 cm^{-1}).

6.3.2 Results and discussion

In order to deposit microcrystalline silicon, the hydrogen dilution during deposition is increased by lowering the silane gas flow. The hydrogen gas flow is kept constant at 100 sccm. The hydrogen dilution is varied between 0.909 and 0.985. At each deposition condition, both thin films (~ 150 nm) and thick films (~ 1.2 μm) were deposited. In figure 6.2 the deposition rate of these layers is plotted as a function of the hydrogen dilution. As was expected, the deposition rate decreases as the silane gas fraction decreases. However, still reasonably high values of more than 0.5 $\text{\AA}/\text{s}$ were obtained.

In figure 6.3(a) the crystalline ratio R_c is shown for samples on Corning 1737 glass. Apparently, the transition from the amorphous to the microcrystalline regime on glass substrates occurs for hydrogen dilutions above 0.93. The lower crystalline ratio of thin films made at high hydrogen dilution indicates that the crystallinity of these layers is still evolving after 150 nm of deposition. Figure 6.3(b) clearly shows the relative decrease of the amorphous Raman peaks at 330 cm^{-1} , 445 cm^{-1} and 480 cm^{-1} when the hydrogen dilution increases.

Figure 6.4 shows the bandgap E_{04} and the refractive index n_0 of the thin layers as a function of the hydrogen dilution. Both parameters were derived from specular reflection/transmission measurements. Although a small error is made as part of the light is lost due to scattering of the light in microcrystalline regions, a trend can be seen for both the bandgap and the refractive index. The bandgap E_{04} increases with the hydrogen dilution, indicating that the absorption coefficient decreases for

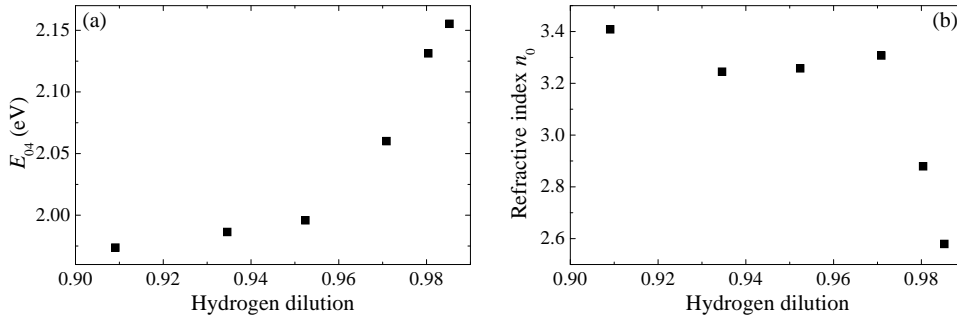


Figure 6.4: (a) Energy E_{04} at which the absorption coefficient equals 10^4 cm^{-1} and (b) refractive index n_0 as a function of the hydrogen dilution.

photon energies $\gtrsim 2 \text{ eV}$. This corresponds with the increase in the crystalline fraction in the material shown in figure 6.2(a), as this means that the bandgap becomes more indirect. At the same time, the refractive index goes down abruptly at 0.97, indicating that the material becomes void-rich.

Figure 6.5(a) plots the hydrogen concentration and the microstructure parameter R^* of as-deposited layers as a function of the hydrogen dilution during deposition. For these layers, the hydrogen concentration decreases from 9.6 at.% to 2.5 at.% as the hydrogen dilution increases. The microstructure parameter increases from 0.11 to 0.84, due to the decreasing amorphous fraction in the material. The increasing poros-

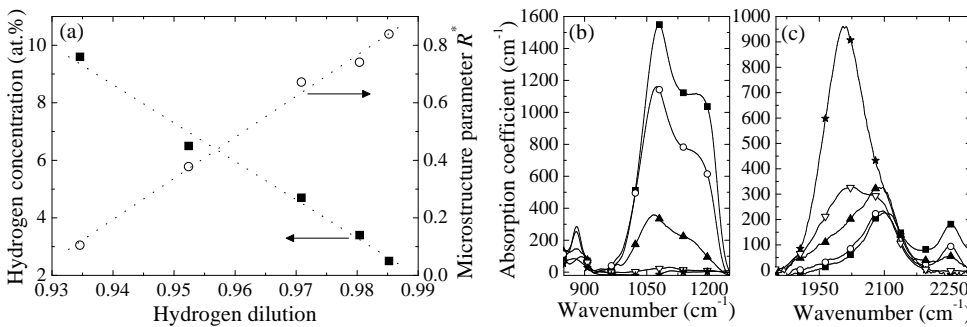


Figure 6.5: (a) Hydrogen concentration (\blacksquare) and microstructure parameter R^* (\circ) of as-deposited layers as a function of the hydrogen dilution during deposition. The dotted lines are plotted as a guide to the eye. (b), (c) Fourier-transform infrared spectra of different $\mu\text{c-Si:H}$ layers made using hydrogen dilutions of 0.985 (\blacksquare), 0.980 (\circ), 0.971 (\blacktriangle), 0.952 (∇) and 0.926 (\star). The spectra were measured three months after deposition.

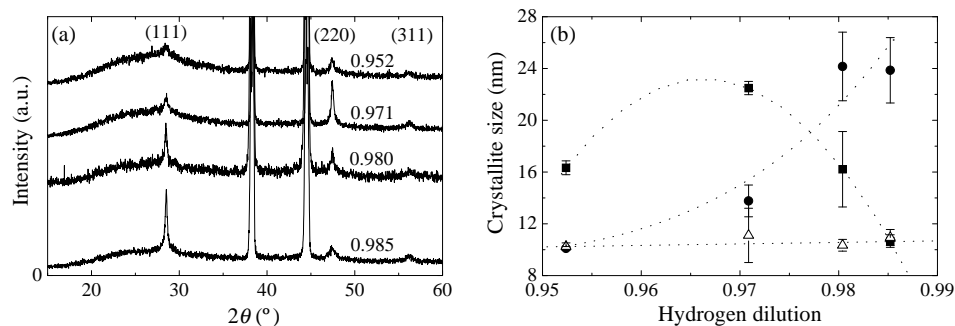


Figure 6.6: (a) X-ray diffractograms of the hydrogen dilution series. The graphs are shifted vertically for better clarity. (b) Crystallite size as determined from XRD measurements for different diffraction peaks: (111) (●), (220) (■) and (311) (△).

ity of microcrystalline silicon with the hydrogen dilution during deposition can also be seen in figure 6.5(b) and (c), in which the Fourier-transform infrared spectra are plotted. The data were taken three months after the deposition of the layers. Clearly visible are the silicon-oxide bond related peaks around 1100 cm^{-1} and around 2260 cm^{-1} , which increase with the hydrogen dilution. These peaks are caused by the presence of Si-O-Si bond structures, which have a transverse optical resonance frequency of 1076 cm^{-1} and a longitudinal optical resonance frequency around 1180 cm^{-1} [92], and by H-SiO₃ clusters, which have a resonance frequency of 2260 cm^{-1} [93]. The materials made using hydrogen dilutions below 0.96 do not oxidize in air. In the FTIR spectra measured directly after deposition, no silicon-oxide bond related peaks were present around 1100 cm^{-1} . Apparently, the crystallites do not coalesce at high hydrogen dilutions, leaving open paths in the material where oxygen can penetrate into the layer, as was also seen in the decrease of the refractive index.

The diffusion of oxygen into the layers is known to result in *n*-type doping. This effect is also seen from the decrease of the activation energy of the samples decreases with time. However, for application in solar cells the oxygen diffusion will be less problematic, as the layers are covered with a *p*-type layer and a contact layer which act as a diffusion barrier. The photoresponse of the hydrogen diluted layers decreases strongly from 10^7 to 10^1 when going from amorphous to the most crystalline layers.

Figure 6.6(a) shows X-ray diffractograms of the thick microcrystalline layers deposited using different hydrogen dilutions. The large peaks at 38° and 44° results from reflection at the aluminum sample holder. In contrast to the columnar, (220) oriented, crystals in polycrystalline silicon, the crystallites in the microcrystalline silicon layers do not have a single orientation, as is clear from the presence of various intensity peaks in the diffractograms. The total peak area increases roughly with in-

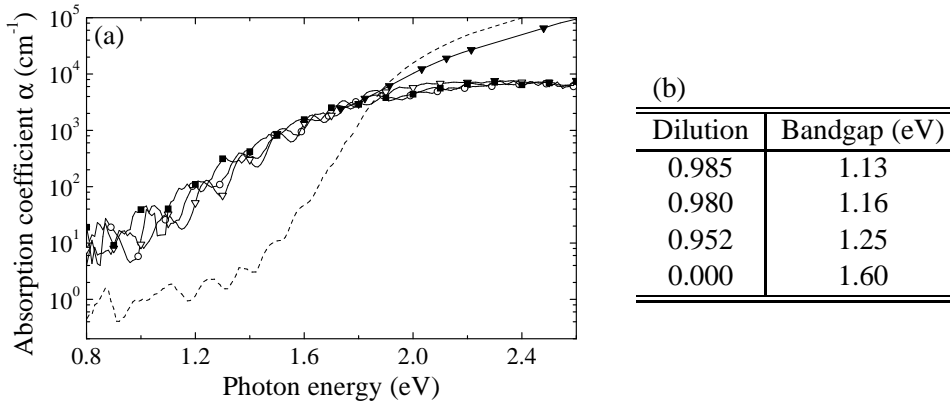


Figure 6.7: (a) Optical absorption coefficient α as determined by PDS for layers deposited using hydrogen dilutions of 0.985 (\blacksquare), 0.980 (\circ) and 0.952 (∇). For comparison, results of hot-wire deposited amorphous silicon, made at 250 °C, are shown (—). Data from reflection/transmission measurements are also plotted for a thin sample made using a hydrogen dilution of 0.952 (\blacktriangledown). (b) Optical bandgap as determined from PDS measurements for samples made at different hydrogen dilutions. The error in all values is about 0.06 eV.

creasing hydrogen dilution, indicating that the crystalline volume fraction increases. For all peaks, the crystallite grain size t_{hkl} was determined using equation (2.18). Here h , k , and l denote the Miller indices of the diffraction planes. In order to minimize the error in the calculations, the average over several high-resolution measurements was taken for each diffraction peak. The results are plotted in figure 6.6(b). The value of t_{311} does not vary with the hydrogen dilution, as it remains around 10 nm. In contrast to this, t_{111} increases with the hydrogen dilution, while t_{220} has a maximum around a hydrogen dilution of 0.97. For all peaks, the average size of the crystallites lies between 10 nm and 25 nm. These values agree well with those found by others for PECVD deposited material [6, 94].

In figure 6.7(a) the optical absorption coefficient is plotted for thick layers made at different hydrogen dilutions. For comparison, also the results of an amorphous layer are shown. It is clear that the red response of the microcrystalline layers is much higher than that of the amorphous layer. The absorption coefficients of all layers show interference fringes, which are due to internal reflection in the layers or to surface texture. The period of the interference fringes ($\sim 1.3 \mu\text{m}$) corresponds roughly to the thickness of the layers ($\sim 1.2 \mu\text{m}$). The optical bandgap of the materials was derived from a plot of $\sqrt{\alpha}$ versus the photon energy. The results are shown in figure 6.7(b). It is clear that the bandgap decreases with increasing hydrogen dilution, indicating

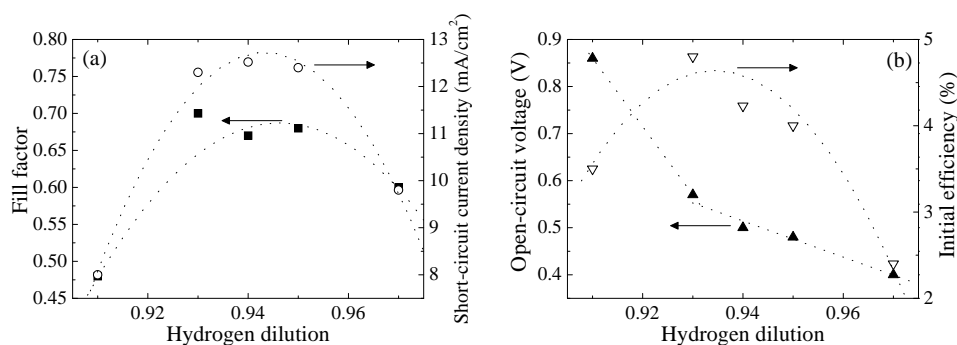


Figure 6.8: (a) Fill factor (■), short-circuit current density (○) and (b) open-circuit voltage (▲) and initial efficiency (▽) of *n-i-p* structured microcrystalline silicon solar cells as a function of the hydrogen dilution during deposition of the absorbing layer. The dotted lines are plotted as a guide to the eye.

that the crystallinity increases. This corresponds to the results from Raman and XRD measurements discussed earlier in this chapter.

The results on hot-wire deposited microcrystalline silicon show that it is possible to deposit a narrow bandgap material at a substrate temperature of 250 °C. Microcrystalline silicon is deposited when a high hydrogen dilution of more than 0.93 is used during deposition. As expected, the crystalline ratio increases with the hydrogen dilution. The crystallites are oriented randomly, and have a size between 10 and 25 nm. The compactness of the material decreases with the hydrogen dilution, and oxygen diffusion can take place in layers made with the highest hydrogen dilutions. In a solar cell, this oxygen diffusion will be limited by the presence of a *p*-doped layer on top of the microcrystalline layer. In the remainder of this chapter, results will be presented on the application of hot-wire deposited microcrystalline silicon as the absorbing layer in *n-i-p* structured solar cells.

6.3.3 Solar cells

Microcrystalline layers, made at different hydrogen dilutions between 0.909 and 0.971, were incorporated in *n-i-p* cells on untextured stainless steel without a back reflector. The thickness of the absorbing layer was about 1 μm. The measured parameters were all obtained using a light mask. The results of the best cells at each deposition condition are plotted in figure 6.8.

For a hydrogen dilution of 0.971, the best cell had an open-circuit voltage of 0.40 V, a short-circuit current density of 9.8 mA/cm², and a fill factor of 0.60, resulting in an initial efficiency of 2.4 %. All these parameters improve when the hydrogen dilution decreases and the crystalline ratio decreases. At a hydrogen dilution of 0.935, the

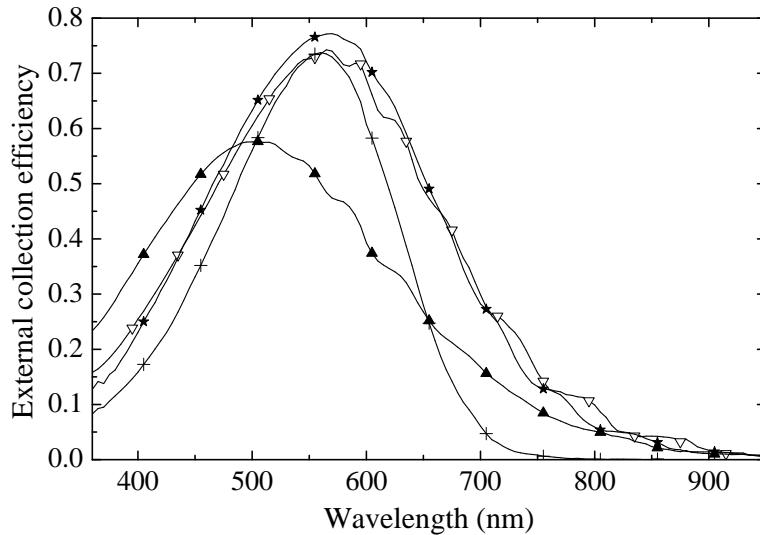


Figure 6.9: External collection efficiency of the best *n-i-p* cells with a $1.0 \mu\text{m}$ thick microcrystalline silicon absorbing layer. Different hydrogen dilutions were used, namely 0.971 (▲), 0.952 (▽), 0.926 (★) and 0.909 (+).

best cell has an open-circuit voltage of 0.57 V, a fill factor of 0.70, and a short-circuit current density of 12.3 mA/cm^2 , resulting in an initial efficiency of 4.8 %. Without the use of a mask, the short-circuit current density was 14.5 mA/cm^2 , resulting in an initial efficiency of 5.7 %. The values of the open-circuit voltage and of the fill factor are remarkably good for microcrystalline solar cells. For this cell, it is noted that layers made on glass using a similar hydrogen dilution are fully amorphous. For hydrogen dilutions below 0.926 the intrinsic layer becomes amorphous. However, as the thickness of the intrinsic layer is large, the best cell from this run has a fill factor of only 0.48, a short-circuit current density of 8.9 mA/cm^2 , and an open-circuit voltage of 0.86 V. Apparently, the best solar cells are made just before the transition from the microcrystalline to the amorphous regime. The external collection efficiencies of the best cells at different hydrogen dilutions are plotted in figure 6.9. The external collection efficiency of the highest diluted solar cell deviates strongly from the characteristics recorded for other dilutions. This is probably caused by the high defect density at the grain boundaries, which was already concluded from the oxygen incorporation seen in FTIR and activation energy measurements. The red response of all cells, and therefore the short-circuit current density, can be improved using a textured back reflector and/or thicker absorbing layers.

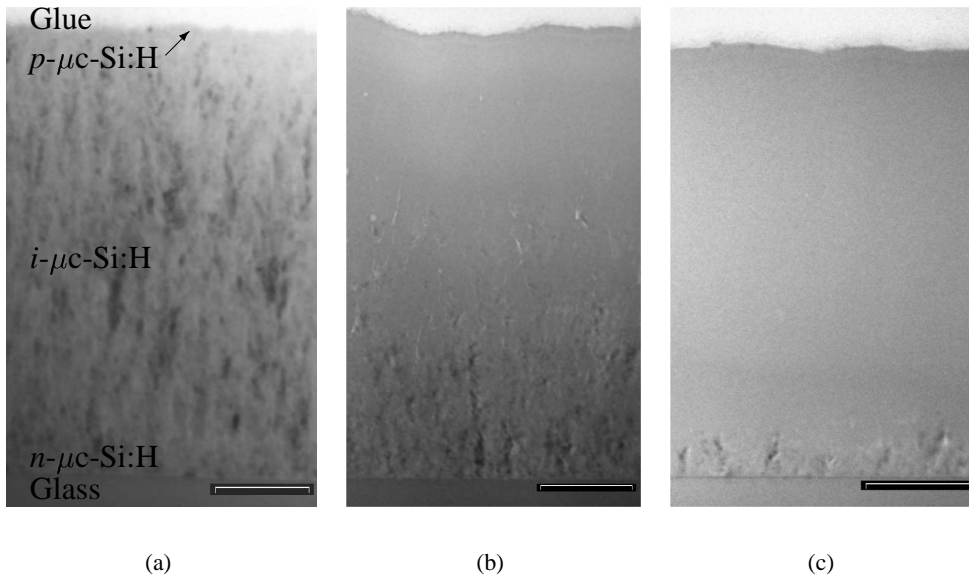


Figure 6.10: Cross sectional TEM micrographs of *n-i-p* structured cells made at different hydrogen dilutions. The substrate for *n-i-p* structures for TEM purposes is Corning glass. The hydrogen dilutions are 0.971 (a), 0.935 (b), and 0.926 (c). In all micrographs, the scale bar corresponds to a length of 200 nm.

6.3.4 Microstructure

Different microcrystalline silicon solar cells were investigated by cross sectional transmission electron microscopy (X-TEM) to retrieve information about the structural homogeneity of the absorbing layers and about the presence of voids. As it is very difficult to prepare samples on (magnetic) stainless steel, samples which were simultaneously deposited on adjacent Corning glass were investigated. Figure 6.10 shows cross sectional transmission electron microscopy (X-TEM) micrographs of *n-i-p* structured cells made at different hydrogen dilutions during deposition. From this figure, it is clear that the structure of the absorbing layer depends heavily on the hydrogen dilution of the silane gas during deposition. At a hydrogen dilution of 0.971, the absorbing layer is fully microcrystalline, with a homogeneous structure. In contrast to this, the absorbing layer made using a hydrogen dilution of 0.935 starts microcrystalline, but gradually becomes less crystalline, and becomes even amorphous at a certain thickness! This is against the phase diagram concepts of Collins *et al.* [95]! The absorbing layer made at a dilution of 0.926 is fully amorphous. The observed amorphicity of the samples deposited using a hydrogen dilution of 0.926 and

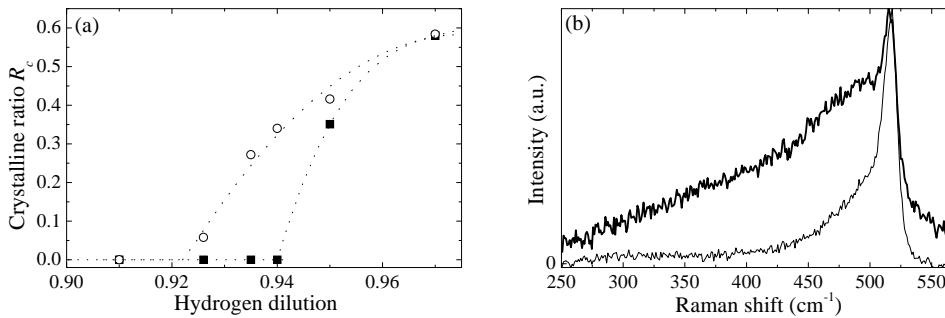


Figure 6.11: (a) Crystalline ratio R_c of *n-i-p* structured solar cells as a function of the hydrogen dilution during deposition of the absorbing layer, for cells on Corning glass (■) and cells on stainless steel (○). The measurements are done with the illumination through the *p*-doped layer. (b) Raman spectra of two 40 nm thick microcrystalline *n*-layers, simultaneously deposited on stainless steel (thin line) and Corning glass (thick line).

0.935 seems to be in contradiction with the results of the current-voltage measurements. The low open-circuit voltages (< 0.6 V), low series resistances ($< 8 \Omega\text{cm}^2$), the improved red response and the high fill factors ($\gtrsim 0.6$) are evidence that the cells made at a dilution of 0.926 and 0.935 are microcrystalline. This difference in crystallinity for different substrates was investigated further using Raman spectroscopy. The solar cells were illuminated through the *p*-layer to get information about the top part of the cells. Figure 6.11(a) shows the crystalline ratio R_c of the solar cells as a function of the hydrogen dilution, both for cells on stainless steel, and for cells on Corning glass. Although the *p*-layer, through which the cells are illuminated, is microcrystalline, the crystallinity of this layer is not detected by Raman spectroscopy of amorphous silicon solar cells. Therefore, the influence of this layer on the total Raman spectrum can be ignored. From figure 6.11(a) it is clear that the cells on stainless steel have a much larger crystalline ratio than the cells deposited on glass. The Raman spectra of cells deposited on glass correspond well with the spectra of single layers on glass, which were shown in figure 6.3(a). Apparently, the use of stainless steel enhances the crystallinity of the solar cells. More specifically, the crystallinity of the *n*-layer is enhanced by the use of stainless steel as substrate. This can also be seen in figure 6.11(b), which shows the Raman spectra of two 40 nm thick *n*-layers, which were simultaneously deposited on stainless steel and Corning glass. The layer on glass has a crystalline ratio of 0.37, while the layer on stainless steel has a much higher crystalline ratio of 0.58. This dependence of the crystallinity of the *n*-layer on the substrate has been seen before [96], and can, most likely, be attributed to a difference in surface roughness of the substrates [97]. The improved crystallinity of the

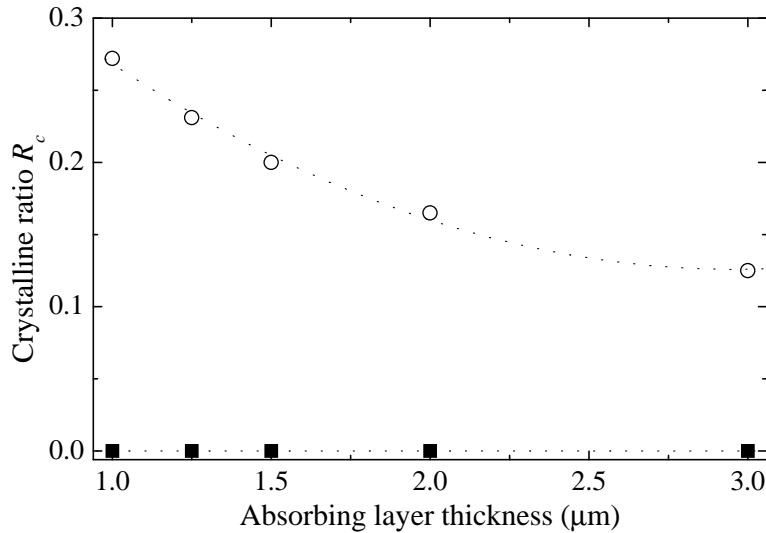


Figure 6.12: Crystalline ratio R_c as a function of the thickness of the intrinsic layer for $n-i-p$ structured solar cells made at a hydrogen dilution of 0.935, for cells on Corning glass (■) and cells on stainless steel (○). The measurements are done with the illumination through the p -doped layer. The lines are drawn as a guide to the eye.

n -layer results in enhanced crystalline growth of the absorbing layer [98]. From the Raman measurements it is clear that this effect can be very drastic, especially for layers which are deposited at the transition from the amorphous to the microcrystalline regime.

Figure 6.12 shows the crystalline ratio of $n-i-p$ structured cells made at a hydrogen dilution of 0.935 as a function of the thickness of the absorbing layer. The crystallinity of the cells on stainless steel decreases with the thickness of the intrinsic layer, which was also seen in figure 6.10(b) for samples on glass. On glass, the absorbing layer is amorphous for all thicknesses above 1 μm .

The crystallinity of layers deposited at a higher hydrogen dilution of 0.952 does not change with the layer thickness, as the crystalline ratio is 0.4 for films between 150 nm and 3 μm . It can be concluded that the morphology changes only for layers deposited at the transition from the microcrystalline to amorphous regime. As all deposition parameters remain constant during deposition, the change in material structure must be related to a change in filament properties during deposition. Therefore, by monitoring the filament power and temperature during deposition it should be possible to get insight in the deposition conditions. However, due to the position

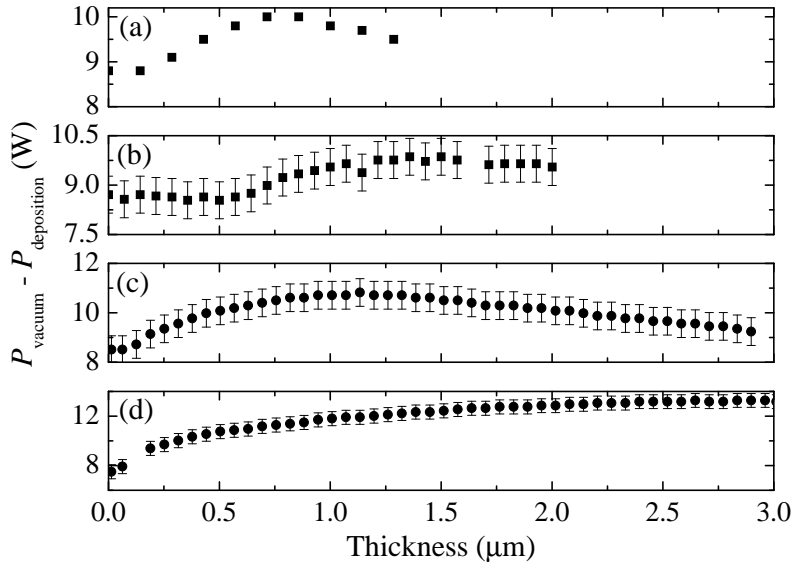


Figure 6.13: Filament power during deposition relative to the filament power in vacuum (before deposition) as a function of the layer thickness for four different depositions with one set of filaments. The deposition order is from (a) to (d). The hydrogen dilutions used are 0.952 (●) and 0.935 (■).

of the shutter in the deposition chamber when it is open, it is not possible to measure the filament temperature during actual deposition. Therefore, only the power dissipated in the filaments can be measured. In general, the filament power depends on the power loss in the filament connections, the power loss by radiation, the heat dissipation due to gas dissociation, and losses due to convection [47]. Figure 6.13 plots the filament power as a function of the layer thickness for different samples made with one set of filaments. The layer thickness equals the product of the deposition time and the deposition rate (see figure 6.2). The power dissipated in the filaments is not constant, but changes during deposition for all depositions shown in figure 6.13. Unfortunately, for each deposition the variation in the filament power is different, which makes it difficult to draw precise conclusions from these measurements. However, a few remarks can be made. Firstly, the changes in filament power for depositions done using a hydrogen dilution of 0.935 are in the order of 1.5 W, which is smaller than the variations of 3 to 4 W found for depositions made using a hydrogen dilution of 0.952. Therefore, it is expected that the influence of the change in filament power is larger at higher hydrogen dilutions. On the other hand, the deposition done at a dilution of 0.935 lies on the edge of the transition from the microcrystalline to

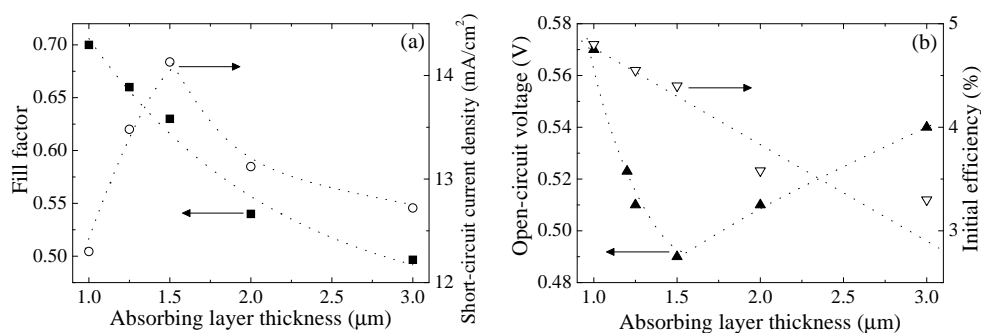


Figure 6.14: (a) Fill factor (■), short-circuit current density (○) and (b) open-circuit voltage (▲) and initial efficiency (▽) of *n-i-p* structured microcrystalline silicon solar cells as a function of the thickness of the absorbing layer. For all cells, the hydrogen dilution is 0.935. The dotted lines are plotted as a guide to the eye.

the amorphous regime. In this case, a small change in filament properties can have a drastic effect on the material structural properties. A second effect is that, for the four depositions in figure 6.13, the power in vacuum to reach a certain filament current increases with the filament age (not shown). Apparently, the resistivity of the filaments increases with the filament age, which is most likely due to the formation of silicides and the accompanying change in filament structure. This effect illustrates that, although the filaments are preheated at elevated temperature before deposition, the influence of silicide formation is still present. From these measurements it seems most likely that the change in filament properties causes the changing microstructure of samples deposited at a hydrogen dilution of 0.935.

6.3.5 Thickness dependence

Figure 6.14 shows the parameters of the solar cells as a function of the thickness of the absorbing layer. The hydrogen dilution during deposition of the absorbing layer was kept constant at 0.935. When the thickness of the absorbing layer increases, the electric field over this layer decreases, resulting in enhanced recombination of photogenerated carriers. This results in a decrease in the fill factor, which can also be seen in figure 6.14(a). The number of photogenerated carriers increases with the absorbing layer thickness, which results in a higher generated current. However, the enhanced recombination results in a maximum in the short-circuit current density, as can also be seen in figure 6.14(a). As the open-circuit voltage is affected negatively by the recombination rate, a decrease in V_{oc} can be seen in figure 6.14(b). However, at a certain thickness, the open-circuit voltage increases again. This effect is caused

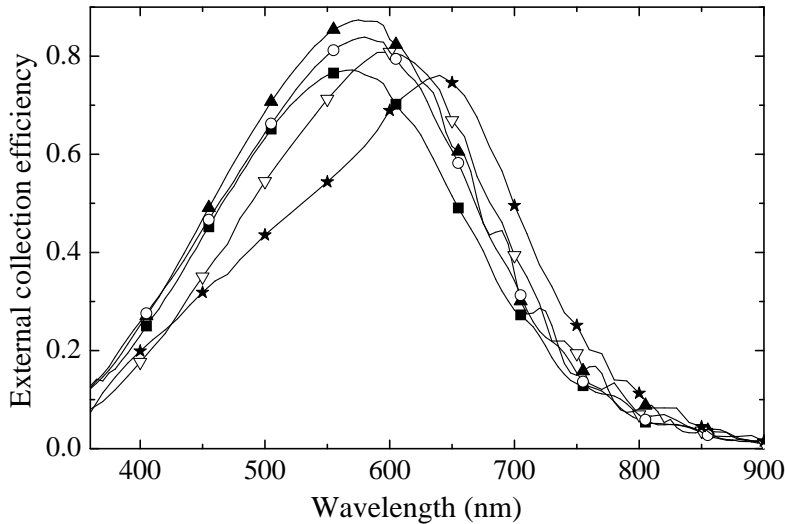


Figure 6.15: External collection efficiency of the best *n-i-p* structured cells as a function of the absorbing layer thickness. A hydrogen dilution of 0.935 was used during deposition of the absorbing layer. The absorbing layer thicknesses are 1.0 μm (■), 1.25 μm (○), 1.5 μm (▲), 2.0 μm (▽) and 3.0 μm (★).

by the inhomogeneous structure of microcrystalline silicon deposited at a dilution of 0.935, as was already shown in figures 6.10(b) and 6.12. When the thickness of the absorbing layer increases, the material becomes less crystalline. Therefore, the bandgap of this material increases with the thickness. As a result, the open-circuit voltage, which is directly correlated with the bandgap, increases. Apparently, this effect becomes dominant for layer thicknesses larger than 1.5 μm . The (initial) efficiency decreases with the absorbing layer thickness, indicating that the extra red response does not weigh up to the recombination losses, and that the amorphous material which is deposited is not device quality type of amorphous silicon.

To illustrate these effects, the external collection efficiencies of solar cells with different absorbing layer thickness are shown in figure 6.15. When the absorbing layer thickness increases from 1.0 μm to 1.5 μm , the short-circuit current density increases due to an improved red response. For even higher absorbing layer thickness, the red response goes up only slightly. This means that most of the red light is lost due to the bad reflectivity of the stainless steel substrates. At the same time the blue response decreases due to recombination of charge carriers. It is clear that, in order to benefit from the high red response of microcrystalline silicon, a (textured) back

reflector layer is required and that a phase transition must be avoided.

Although the best microcrystalline solar cells are made using a hydrogen dilution of 0.935, the dependence of the microstructure of the absorbing layer on its thickness is a serious issue. In principle, it should be possible to adapt the deposition parameters during deposition in order to keep the material homogeneously structured. Unfortunately, a complete control of the material structure is probably difficult at this filament temperature. It is expected that a higher filament temperature has a beneficial effect on the structural homogeneity of this material, due to the reduction of the influence of silicide formation on the wires. However, in this case also the substrate temperature during deposition is increased. As the microcrystalline silicon layers will be applied in the bottom cell of a multijunction solar cell, it is important that the layers have a high red absorption. Therefore, more crystalline layers are needed, and a higher hydrogen dilution during deposition is preferred. Material made at a hydrogen dilution of 0.952 has a constant crystalline ratio, which is independent of the layer thickness. Another advantage of this material is the smaller amorphous fraction, which will result in an improved stability against light-soaking, as was already indicated in section 1.3.

6.4 Conclusions

The hot-wire chemical vapor deposition technique has been used for the deposition of microcrystalline silicon, as a low-temperature alternative for polycrystalline silicon. A substrate temperature of 250 °C was used, and tantalum was used as the filament material. Microcrystalline silicon is deposited at high hydrogen dilutions ($\gtrsim 0.93$). These layers had a high crystalline ratio and corresponding microstructure parameter. In contrast to the columnar, (220) oriented, crystals in polycrystalline silicon, the crystallites in the microcrystalline silicon layers do not have a single orientation. The average crystallite size lies between 10 nm and 25 nm. Due to the high crystalline ratio, the bandgap of the material was low (≤ 1.25 eV), which makes the material suitable for application as the absorbing layer in the bottom cell of a multijunction solar cell. Unfortunately, unlike some of the polycrystalline silicon layers made at 500 °C, microcrystalline silicon layers made at hydrogen dilutions higher than 0.971 ($R_c > 0.6$) oxidized in air, indicating the porous nature of these materials. Materials made at hydrogen dilutions below 0.96 ($R_c < 0.5$) did not oxidize.

Microcrystalline layers made at different hydrogen dilutions were incorporated in *n-i-p* structured solar cells on untextured stainless steel. The results on hot-wire deposited microcrystalline silicon solar cells correspond well with those found by others [98, 99]. The best solar cells were made with material deposited at the transition from the microcrystalline to the amorphous regime. The best cell was deposited using a hydrogen dilution of 0.935. This cell has a fill factor of 0.70, an open-circuit

voltage of 0.57 V and an initial efficiency of 4.8 %. This efficiency is significantly higher than that of the best polycrystalline silicon cell (4.41 %). This difference is mainly caused by a much higher open-circuit voltage of the microcrystalline silicon solar cell. Unfortunately, the structure of material made at a dilution of 0.935 turns out to be inhomogeneous along the growth direction, as it became less crystalline with increasing thickness. On stainless steel substrates, this effect became dominating at thicknesses above 1.5 μm . On glass substrates, this influence was already seen at thicknesses of around 0.4 μm . The structural inhomogeneity is, most likely, due to (small) changes in the filament properties during deposition, which can have a large influence for samples made near the microcrystalline to amorphous transition. In order to improve the red response of the solar cells, the influence of the absorber layer thickness on the cell parameters was measured. However, the improved red response with increasing thickness did not weigh up to the enhanced recombination rate. As a result, the solar cell efficiency decreased with the absorbing layer thickness. To optimize the microcrystalline silicon solar cells, it is therefore necessary to incorporate a (textured) back reflector and to avoid the transition from microcrystalline to amorphous material. It is expected that the use of a higher filament temperature has a beneficial effect on the crystallinity of the material. Nevertheless, the results on the material properties and solar cells clearly indicate the large potential of hot-wire deposited microcrystalline silicon for the application in solar cells.

7

Hot-wire deposited *n*-doped microcrystalline silicon

*The hot-wire chemical vapor deposition technique was used for the deposition of *n*-type microcrystalline silicon layers. Due to the internal arrangement of the deposition chamber that is used for deposition of *n*-type layers, no shutter was present. An incubation phase for microcrystalline growth of about 30 nm thick was found. Optimization of the deposition conditions yielded material with a dark conductivity of 13 S/cm, an activation energy of 0.026 eV, at a thickness of 50 nm. The deposition rate was about 1.0 Å/s, which is about six times higher than that of the commonly used plasma-enhanced deposition technique. Application of hot-wire deposited *n*-layers in *n-i-p* structured solar cells resulted in a high open-circuit voltage, but a reduced short-circuit current density compared to cells with a plasma deposited *n*-layer.*

7.1 Introduction

Recently, the application of the hot-wire chemical vapor deposition technique for the deposition of intrinsic amorphous and microcrystalline silicon has resulted in high-quality material and solar cells [89, 100]. Most solar cells incorporating hot-wire deposited absorbing layers contain doped layers, which are deposited by the plasma-enhanced chemical vapor deposition (PECVD) technique [89, 100, 101]. However, there are several disadvantages of the use of the PECVD technique for the deposition of doped layers of solar cells. A high deposition temperature of the absorbing layer in *n-i-p* structured cells causes thermal stress in the *n*-type layer, due to which cracks are formed [91]. These cracks are likely to deteriorate the cell quality. Therefore, doped layers that are resistant against high temperature and atomic hydrogen are crucial for high-quality solar cells. Another disadvantage of the PECVD technique is the low deposition rate, resulting in long deposition times. As both high deposition temperatures and high deposition rates can be obtained using the hot-wire CVD technique, it is expected that this technique can yield high-quality doped layers.

This chapter focusses on the deposition of microcrystalline *n*-type silicon layers for the incorporation in *n-i-p* structured solar cells. Due to the internal arrangement of the chamber used for depositions of *n*-type layers, only shutterless depositions can take place. Commonly, a shutter is used to avoid deposition on the substrate during the first stages of the process, when the deposition conditions have not yet stabilized.

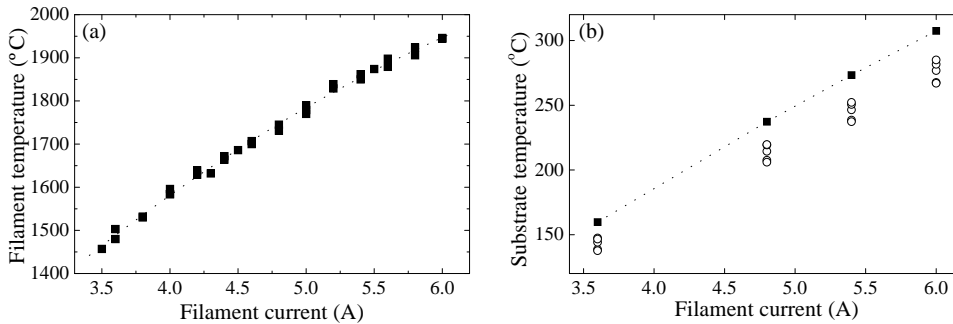


Figure 7.1: (a) Filament temperature as a function of the filament current. (b) Substrate temperature in deposition chamber #3 as a function of the filament current, measured in the middle (■) and in the quadrants of the substrate (○). The dotted lines serve as guides to the eye.

Fortunately, in an *n-i-p* structured solar cell, the interface between the metal substrate and the *n*-type layer is not crucial for the device performance. As a result, a simple deposition geometry can be used for the deposition of these layers. In this chapter, the influence of several deposition parameters on the structural and electrical properties of hot-wire deposited *n*-layers are discussed. Furthermore, results on the application of these layers in *n-i-p* structured solar cells are presented.

7.2 Experimental details

For the hot-wire chemical vapor deposition of *n*-type silicon layers, a removable assembly is used which contains two thin straight tantalum filaments. Using this assembly, depositions were done in chamber #3 of the PASTA system, which is normally used for plasma-enhanced deposition of *n*-layers. The filaments have a diameter of 0.3 mm and are located at about 1.5 cm from the substrate, and parallel to the gas flow direction. The distance between the filaments is 4 cm. Figure 7.1(a) shows the filament temperature in deposition chamber #3 as a function of the filament current. As no external heater is used, the substrates are heated only by radiation from the filaments. In figure 7.1(b) the substrate temperature is plotted as a function of the filament current.

Due to the presence of the rf electrode, no shutter could be implemented in the deposition chamber and the distance between the filaments and the substrate is kept short. In order to minimize the influence of the absence of a shutter, all depositions were done following a well-defined procedure [102]. First, the filaments were pre-heated to the deposition temperature. After this, the deposition gas mixture (silane,

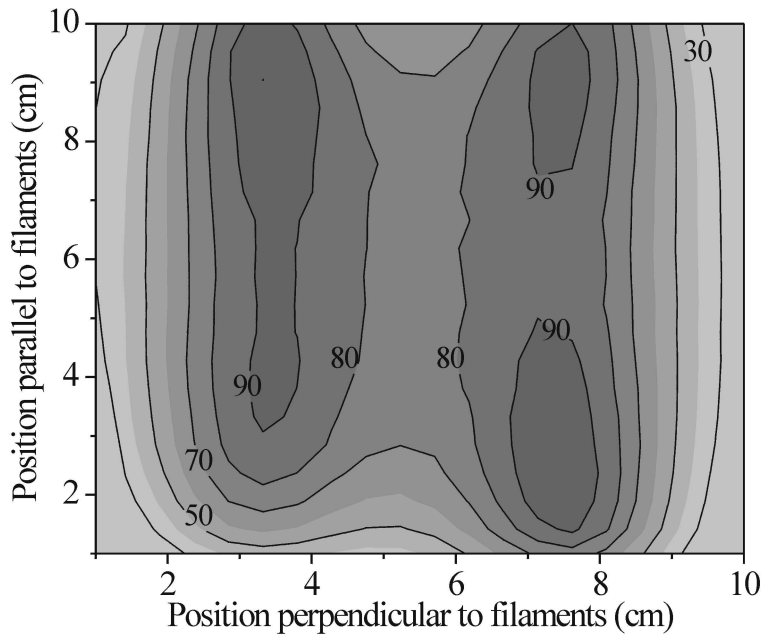


Figure 7.2: Thickness profile of a hot-wire deposited n-layer. The numbers indicate the thickness percentage relative to the maximum thickness.

hydrogen and a 2 % mixture of phosphine (PH_3) in hydrogen) was admitted, and the process pressure was set. For all samples, a hydrogen gas flow rate of 100 sccm was used, and the pressure was kept at 100 μbar . The hydrogen dilution during deposition is defined as $\Phi_{\text{H}_2}/(\Phi_{\text{SiH}_4} + \Phi_{\text{H}_2})$. Similarly, the phosphine dilution is defined as $\Phi_{\text{PH}_3}/(\Phi_{\text{SiH}_4} + \Phi_{\text{PH}_3})$. The layers were deposited on Corning 1737 glass, and characterized by optical and electrical measurements. Raman spectroscopy was used to investigate the crystallinity of the samples, both at the front side and at the back side (by illumination through the glass).

7.3 Results and discussion

Figure 7.2 shows the thickness profile of a hot-wire deposited microcrystalline n-layer. It is clear that the layers are quite inhomogeneous, which is caused by the large difference between the distance between the filaments (4 cm) and the distance from the filaments to the substrate (1.5 cm) [103]. The layers are thickest directly above the filaments. Material deposited between the filaments often had slightly improved dark

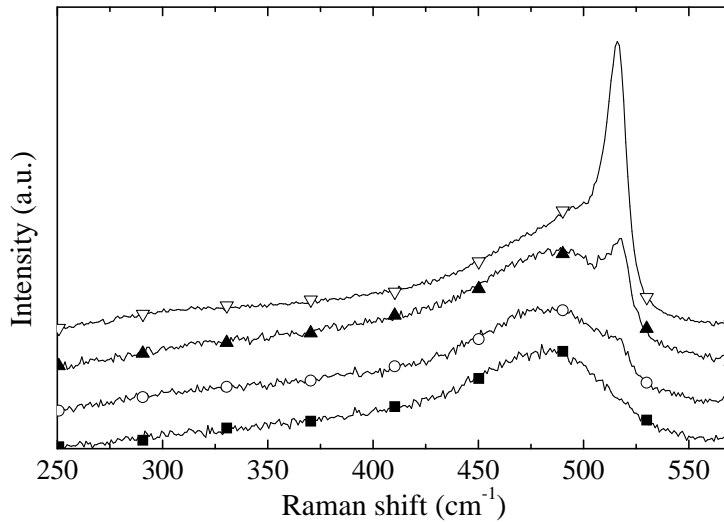


Figure 7.3: Raman shift of hot-wire deposited n -layers with a thickness of 21 nm (\blacksquare), 40 nm (\circ), 49 nm (\blacktriangle), and 133 nm (∇). The graphs are shifted vertically for better clarity.

conductivity values and lower crystalline ratios than material deposited directly above one of the filaments. The thickness of material deposited at the edge of the substrate was much lower, resulting in inferior electrical properties and low crystalline ratios. The results presented in this chapter refer, unless indicated otherwise, to material deposited directly above one of the filaments.

As a starting point for n -layer optimization, a filament temperature of 1850 °C was chosen. This temperature is the same as the filament temperature at which device quality amorphous and microcrystalline silicon were deposited, as was shown in sections 3.3 and 6.3.2. Therefore, a filament current of 5.4 A was used. This current is lower than that for amorphous or microcrystalline silicon deposition, as the filament diameter is smaller. In order to study the effect of the absence of a shutter on the structural properties of the material, layers with different thicknesses were deposited. The hydrogen dilution and phosphine dilution were 0.976 and 4.8×10^{-3} , respectively. Figure 7.3 shows the Raman spectra of layers with a thickness of 21 nm, 40 nm, 49 nm, and 133 nm. The crystalline ratios of these layers are 0.00, 0.09, 0.24, and 0.42, respectively, indicating that the crystallinity increases with the thickness. A similar trend was found using a filament current of 6.0 A, a hydrogen dilution of 0.987, and a phosphine dilution of 9.1×10^{-3} . In this case, a layer with a thickness of 27 nm had an activation energy of 0.35 eV and a dark conductivity of 6.4×10^{-3}

Table 7.1: Material properties of hot-wire deposited microcrystalline *n*-type layers. Different hydrogen and phosphine dilutions were used.

H ₂ dilution	10 ³ × PH ₃ dilution	<i>d</i> (nm)	<i>r_d</i> (Å/s)	<i>E_{act}</i> (meV)	<i>σ_d</i> (S/cm)	<i>R_c</i>
0.976	4.8	49	2.1	34	5.4	0.24
0.976	2.4	52	2.0	46	3.3	0.35
0.987	9.1	56	1.1	34	7.1	0.43
0.987	9.1	37	0.92	38	4.4	0.38
0.987	4.6	45	0.90	52	2.4	0.43

S/cm. These values are typical for amorphous material. For a layer with a thickness of 48 nm, an activation energy of 0.08 eV and a dark conductivity of 1.1 S/cm were found, which are values typical for microcrystalline material. From these results, the thickness of the incubation phase for crystalline growth can be estimated to be about 30 nm. This value compares reasonably well with the incubation phase thickness of layers deposited under similar conditions but with the use of a shutter, which can amount from about 10 nm to a few tens of nanometers [104, 105]. It is clear that the absence of a shutter does not have a negative effect on the incubation phase of the hot-wire deposited *n*-layers.

To optimize the material properties of hot-wire deposited microcrystalline *n*-layers, the influence of the hydrogen dilution and of the phosphine gas flow rate during deposition was investigated for samples deposited using a filament current of 5.4 A. Two hydrogen dilutions were used, namely 0.987 and 0.976. Also different phosphine dilutions were used. The layer thickness was aimed at 50 nm, as this is a value commonly used in *n-i-p* structured solar cells. Table 7.1 shows the results on these layers. From this table, it can be seen that the electrical properties improve when a higher phosphine dilution is used during deposition, as the dark conductivity increases and the activation energy decreases. The electrical properties hardly depend on the hydrogen dilution during deposition. However, the crystalline ratio increases when the hydrogen dilution increases from 0.976 to 0.987. As can be seen in table 7.2, a higher hydrogen dilution of 0.990 causes a deterioration in both the electrical properties and the deposition rate. At an even higher dilution of 0.993, there is no deposition at all, and the etching rate of the hydrogen becomes dominant over the deposition of silicon.

These results show that, at a filament temperature of 1850 °C, the best microcrystalline *n*-layers are made at a hydrogen dilution of 0.987 and a phosphine dilution of 9.1×10^{-3} . In order to optimize this material, the influence of the filament temperature on the electrical properties of this material is investigated. For this, layers were deposited with a thickness of about 50 nm. The filament current was varied between 4.0 A and 6.0 A, corresponding to a temperature between 1580 °C and 1950

Table 7.2: Material properties of hot-wire deposited microcrystalline *n*-type layers as a function of the hydrogen dilution. A constant phosphine gas flow rate was used.

Hydrogen dilution	d (nm)	r_d (Å/s)	E_{act} (meV)	σ_d (S/cm)	R_c
0.976	49	2.1	34	5.4	0.24
0.987	56	1.1	34	7.1	0.43
0.987	37	0.92	38	4.4	0.38
0.990	45	0.62	74	1.6	0.39
0.993	0	0.0	-	-	-

°C. Samples were taken both directly above one of the filaments and in between the filaments.

Figure 7.4 shows the deposition rate of *n*-type microcrystalline silicon as a function of the filament current for material deposited directly above one of the filaments. The deposition rate shows a clear maximum of about 1.1 Å/s at a filament current of 5.4 A. Apparently, the etching rate of the atomic hydrogen becomes larger than the rate of silicon deposition for higher currents, resulting in a decrease of the total deposition rate. The activation energy and dark conductivity of these samples are given in

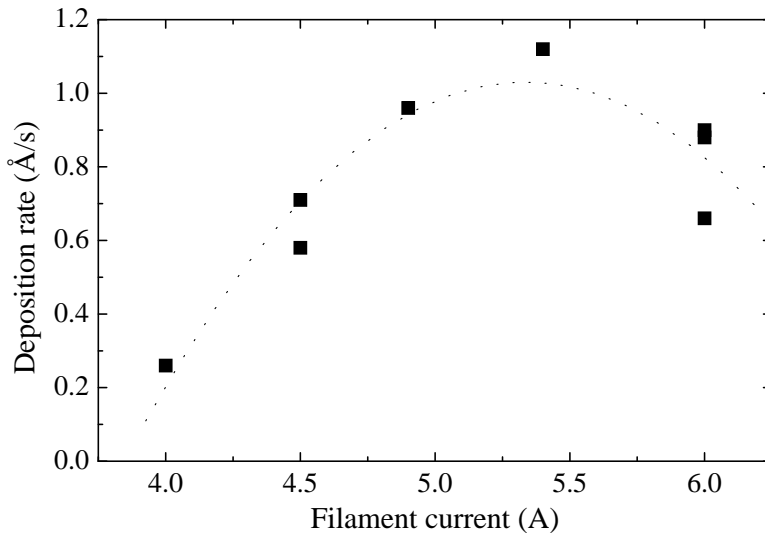


Figure 7.4: Deposition rate of hot-wire deposited microcrystalline *n*-doped layers as a function of the filament current for samples deposited above one of the filaments. The dotted line is plotted as a guide to the eye.

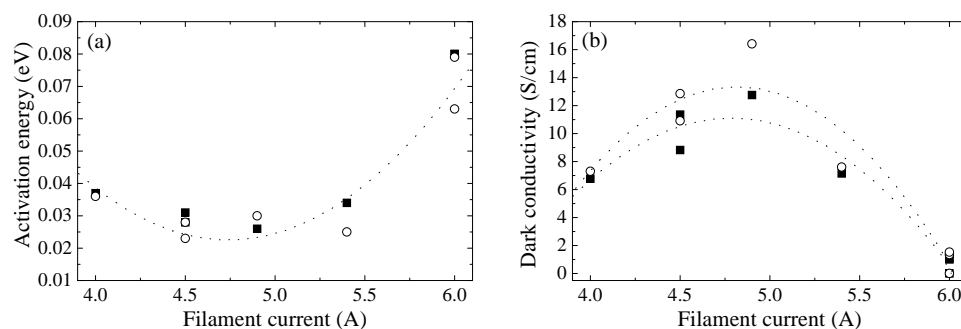


Figure 7.5: (a) Activation energy and (b) dark conductivity as a function of the filament current for hot-wire deposited microcrystalline *n*-type silicon. Measurements are done on samples deposited directly above one of the filaments (■) and on samples deposited in between the wires (○). The dotted lines are plotted as a guide to the eye.

figure 7.5(a) and (b), respectively. At a filament current of about 4.9 A, an optimum was found in the electrical properties, as the dark conductivity had a maximum, and the activation energy had a minimum around this point. The corresponding values were 13 S/cm and 0.026 eV, respectively. For this material, the deposition rate was about 1.0 Å/s. The filament current corresponds to a substrate temperature during deposition of about 230 °C. Material made in between the two wires had slightly better electronic properties, which is likely to be caused by the slightly higher temperature of the middle of the substrate during deposition. The values of the crystalline ratio did not depend much on the filament current, but a minimum of 0.27 was found at 4.9 A, indicating that a larger amount of amorphous phase is present in the material. However, a crystalline ratio of 0.27 is high enough for doped layers in a solar cell. At the same filament current, a maximum of 3.25 was found in the refractive index, indicating that the amorphous phase is more compact. For PECVD deposited *n*-type microcrystalline layers, a dark conductivity and activation energy of 24 S/cm and 0.021 eV were found, respectively, at a deposition rate of 0.16 Å/s. Thus, the optimal electrical properties of hot-wire deposited microcrystalline *n*-layers are comparable to those of PECVD deposited *n*-layers, while the deposition rate is six times higher.

The hot-wire deposited *n*-layers were applied in *n-i-p* structured solar cells on flexible stainless steel substrates. For all cells, the absorbing layer was a 400 nm thick layer of hot-wire deposited amorphous silicon, made at a substrate temperature of 250 °C [89]. The *p*-type layer is described in section 4.2.1. Indium-tin oxide and gold grid contacts were applied as the top contacts of the solar cells. The cells had an active area of 0.13 cm². Figure 7.6(a) shows the current-voltage characteristics under AM1.5 illumination of all solar cells made with a hot-wire deposited *n*-layer. The

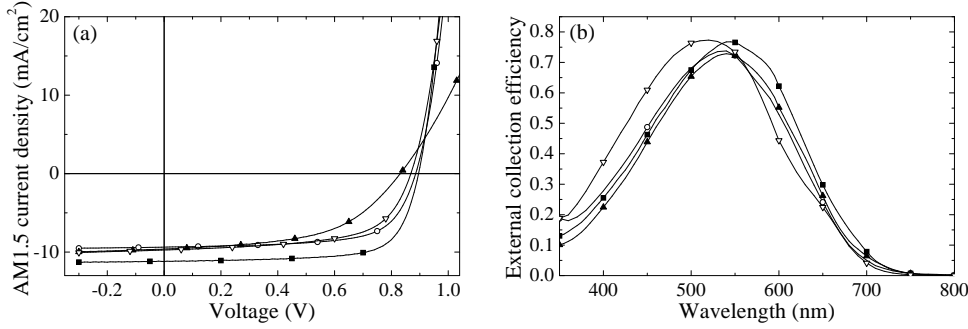


Figure 7.6: (a) AM1.5 current-voltage characteristics and (b) external collection efficiencies of $n-i-p$ structured solar cells with a hot-wire deposited n -layer. The deposition parameters of the n -layer are as follows: \circ : $I_{fil} = 4.9$ A, $d = 80$ nm; \blacktriangle : $I_{fil} = 4.9$ A, $d = 50$ nm; ∇ : $I_{fil} = 4.0$ A, $d = 50$ nm. Also the characteristics of a reference cell with a PECVD deposited μc -Si:H n -layer are plotted (\blacksquare).

corresponding external collection efficiencies are plotted in figure 7.6(b). Table 7.3 gives an overview of all parameters of these solar cells.

From figure 7.6 and table 7.3 it can be concluded that the cell made with an 80 nm thick n -layer at 4.9 A has a rather low efficiency, which is caused by a high series resistance. For this cell, an atomic hydrogen treatment was performed after n -layer deposition, in order to correct for any hydrogen loss in the material during deposition. A similar cell, made with a thinner n -layer of 50 nm, and without any hydrogen treatment after deposition of the n -layer, has a reduced series resistance, resulting in a much better fill factor of 0.67. This cell also has a high open-circuit

Table 7.3: Characteristics of all $n-i-p$ structured solar cells with a hot-wire deposited microcrystalline silicon n -layer. In all cases, the absorbing layer is hot-wire deposited amorphous silicon, deposited at a substrate temperature of 250 °C. Also the results of a reference cell are given, in which the n -layer is made by PECVD, without the hot-wire assembly in the deposition chamber.

n -layer	V_{oc} (V)	J_{sc} (mA/cm ²)	FF	η (%)	R_s (Ω cm ²)	R_p (k Ω cm ²)
4.9 A, 80 nm	0.83	9.6	0.53	4.2	19	0.63
4.9 A, 50 nm	0.88	9.4	0.67	5.6	7.0	1.4
4.0 A, 50 nm	0.87	9.7	0.62	5.2	9.0	0.84
Reference	0.89	11	0.72	7.2	5.3	2.4

voltage of 0.88 V, which is comparable to the open-circuit voltage of cells with a PECVD deposited *n*-layer. It is unclear why the short-circuit current density is so low. One possibility is that the higher amorphous fraction in the hot-wire deposited *n*-layers results in a higher absorption of (mainly red) light. As a result, the amount of light that reflects on the substrate is reduced, which leads to a lower generated current in the cell. For the cells made with a 50 nm thick *n*-layer at a filament current of 4.0 A, the yield is extremely low. Only 5 % of the cells has a fill factor above 0.4. For the cells that work, the open-circuit voltage is 0.87 V, which is comparable to the open-circuit voltage of the reference cell. The short-circuit current density and also the fill factor are rather low, resulting in an efficiency of 5.2 %. However, it is not clear what the reason is for the bad solar cell properties. The results indicate that hot-wire deposited *n*-type microcrystalline silicon is a promising material for application in solar cells, but further research is required to optimize the structural and electrical properties of the material.

7.4 Influence on plasma-enhanced deposition

Unfortunately, the incorporation of the hot-wire assembly in the deposition chamber, and also its removal from the chamber, are time consuming processes. However, if the presence of the assembly does not have a negative influence on the PECVD depositions, the assembly could remain permanently in the deposition chamber. The influence of the presence of the hot-wire assembly on the deposition of PECVD deposited *n*-layers was investigated. Table 7.4 gives an overview of the material properties of plasma-enhanced CVD deposited amorphous and microcrystalline *n*-type layers. The deposition parameters of these layers are given in sections 4.2.1 and 4.3.1. Layers were deposited either with, or without the hot-wire assembly in the deposition chamber. Also the influence of the filament potential with respect to the plasma potential is investigated, by keeping the filaments floating with respect to the plasma, or by grounding them. Due to shadowing effects of the filaments, the thickness distribution of the plasma-enhanced deposited layers is not homogeneous, but the layers are thinner directly above the filaments. In other words, the thickness profile of the plasma deposited layers is reversed with respect to the profile of the hot-wire deposited layers, shown in figure 7.2. When the hot-wire assembly is present in the deposition chamber, the electrode distance has to be increased. To compensate for this effect, a lower deposition pressure is used, keeping the product of the pressure and the electrode distance constant. In table 7.4, it can be seen that the presence of the wires results in a decrease of the deposition rate. With grounded wires, this effect is larger than with floating filaments. Fortunately, there is hardly any influence of the filaments on the electrical properties of the PECVD deposited layers, only that the activation energy improves slightly with the hot-wire assembly in the chamber.

Table 7.4: Material properties of PECVD deposited amorphous and microcrystalline *n*-type layers. Measurements are done on material deposited in the middle of the substrate (in between the wires).

Layer	Filaments	p (μbar)	d (nm)	r_d ($\text{\AA}/\text{s}$)	E_{act} (eV)	σ_d (S/cm)	R_c
<i>a</i> -Si:H	-	300	56	0.80	0.28	0.0069	0.00
<i>a</i> -Si:H	floating	230	57	0.48	0.21	0.011	0.00
μc -Si:H	-	990	49	0.16	0.021	25	0.35
μc -Si:H	floating	790	53	0.15	0.014	19	0.40
μc -Si:H	grounded	790	51	0.10	0.012	20	0.48

The same PECVD deposited *n*-layers were also tested in both *n-i-p* structured and *p-i-n* structured solar cells. However, the open-circuit voltage of all cells was about 10 % lower than that of (old) reference cells. This effect was not due to the presence of the filaments, but the silane gas bottle for the *n*-layer deposition in chamber #3 was almost empty and had to be replaced. No further depositions were done to investigate the solar cell performance with the filaments present in the deposition chamber.

7.5 Conclusions

A removable hot-wire assembly has been used for the deposition of *n*-doped microcrystalline silicon, in a deposition chamber normally used for plasma-enhanced deposition. Due to the internal arrangement of the deposition chamber, no shutter was present. The incubation phase for crystalline growth had a thickness of around 30 nm. The influences of the hydrogen and phosphine dilutions during deposition, and of the filament current on the structural and electrical properties of *n*-type microcrystalline silicon was investigated. For optimization of the material, the layer thickness was aimed at 50 nm, as this is a value commonly used in *n-i-p* structured solar cells.

Optimal electronic properties were found at a filament current of about 4.9 A, a hydrogen dilution of 0.987 and a phosphine dilution of 9.1×10^{-3} . In this case, the substrate temperature was about 230 °C. The material had a dark conductivity of 13 S/cm, and an activation energy of 0.026 eV. These values are comparable to the electrical properties of PECVD deposited *n*-type microcrystalline silicon. However, the deposition rate of hot-wire deposited material was about 1.0 $\text{\AA}/\text{s}$, which is a clear increase compared to the deposition rate of PECVD deposited material. The presence of the hot-wire assembly in the deposition chamber did not influence the material properties of plasma-enhanced CVD deposited *n*-layers significantly. In this case, a decrease in the deposition rate was found, but the electrical properties of the layers were similar.

Application of the hot-wire deposited n -layers in $n-i-p$ structured solar cells resulted in a similar open-circuit voltage compared to solar cells incorporating a plasma-enhanced deposited n -layer. However, the fill factor and short-circuit current density of the cells with a hot-wire deposited n -layer were lower. The results on the hot-wire deposition of n -type microcrystalline silicon show that it is possible to deposit high-quality layers for the application in solar cells. However, further optimization is necessary in order to improve the homogeneity of the structural and electrical properties and to increase the deposition temperature. Furthermore, the results show that, although the presence of a shutter prevents uncontrolled conditions during the first stages of deposition, a shutter is not an absolute necessity for the deposition of high-quality n -type layers. This result is important for application in large-area systems, in which no shutter is present.

8

Tandem solar cells

Different multijunction solar cells have been developed, in which the absorbing layers were deposited using the hot-wire chemical vapor deposition technique. Both the n-i-p structure and the p-i-n structure were investigated. For both structures, it is possible to obtain high open-circuit voltages and high fill factors. In n-i-p structured cells, a current leakage path through the bottom cell is present, which is the result of an unoptimized tunnel-recombination junction. Although the solar cells are not optimized, these results demonstrate the large potential of hot-wire deposited intrinsic silicon for the application in multibandgap solar cells.

8.1 Introduction

Hydrogenated amorphous silicon (*a*-Si:H), polycrystalline silicon (poly-Si) and microcrystalline silicon (μ c-Si:H) have proven to be device-quality materials for the application in solar cells. As these materials have different optical bandgaps between 1.8 eV and 1.1 eV, they can be incorporated as the absorbing layers in a multibandgap tandem solar cell. The concept for this so-called “micromorph” solar cell was introduced by the University of Neuchâtel in a *p-i-n/p-i-n* configuration, using the very high frequency deposition technique (VHF-CVD) [106]. Using the high pressure PECVD technique at 13.56 MHz, the IPV institute of Forschungszentrum Jülich has developed tandem cells with an efficiency of 11.1 % initial, and 10.0 % stabilized [107]. Recently, the University of Neuchâtel has obtained an initial efficiency of 12.3 % using low-pressure CVD deposited zinc oxide as the back reflector [108].

Unfortunately, there are some limitations to the techniques mentioned for deposition of the absorbing layers. Firstly, as microcrystalline silicon has an indirect bandgap, the absorbing layer made from this material must be made rather thick to match the current generated in the amorphous silicon layer. Therefore, the low deposition rate of the two CVD techniques mentioned earlier (typically 5 Å/s) is a serious drawback. Also large area deposition might be a problem due to a lack of uniformity, especially for VHF deposition [18].

The hot-wire chemical vapor deposition (HWCVD) technique has turned out to be a good alternative for PECVD for the deposition of solar cells because of the high deposition rates that can be obtained. For *a*-Si:H deposition, Nelson *et al.* showed that deposition rates of more than 100 Å/s can be obtained without sacrificing material properties [27]. Microcrystalline silicon can be deposited at a rate of over

20 Å/s [109]. Moreover, pure polycrystalline silicon layers, without an amorphous phase, have been deposited at a growth rate of over 5 Å/s [105]. Also it is possible, in principle, to deposit uniformly over large areas, since there are no finite wavelength or plasma confinement effects. Furthermore, the method can be low cost, because of the elimination of expensive rf power supplies and matching boxes.

At Utrecht University, single-junction amorphous silicon, microcrystalline silicon and polycrystalline silicon *n-i-p* structured solar cells were deposited with a best initial efficiency of 7.2 % [89], 4.8 % [110] and 4.4 % [36], respectively. In this chapter, results on the incorporation of hot-wire deposited absorbing layers in various tandem solar cells will be presented and discussed.

8.2 Experimental details

Two ultrahigh vacuum hot-wire deposition chambers were available for the deposition of the amorphous, microcrystalline and polycrystalline silicon layers. This separation made it possible to completely optimize the deposition parameters for each material independently. Amorphous and microcrystalline silicon were deposited in chamber #5, using two straight tantalum filaments. For both materials, the filament current was 10.5 A, corresponding to a filament temperature of 1850 °C (in vacuum). As a result, the substrate temperature was about 250 °C.

For amorphous silicon, pure silane was used as the source gas, at a gas flow rate of 90 sccm and at a pressure of 20 μbar. The deposition rate of this material was about 10 Å/s [89]. The material is characterized by a high photoresponse of 10^6 and a relatively high ambipolar diffusion length (160 nm). The Tauc bandgap of this amorphous silicon is 1.8 eV and the hydrogen concentration is about 12 %. More details about this material are shown in table 3.1.

Microcrystalline silicon was deposited using a high hydrogen dilution during deposition. The deposition pressure was 50 μbar. The hydrogen dilution during deposition was either 0.935 or 0.952 [110]. The deposition rates of these materials were 2.4 Å/s and 2.1 Å/s, respectively. The crystalline ratios of these materials were 10-30 % and 40 %, respectively.

Polycrystalline silicon was deposited in chamber #4, using two coiled tungsten filaments. The filament temperature was 1800 °C, and a deposition pressure of 100 μbar was used. The substrate temperature was about 500 °C. Relevant material properties of this polycrystalline silicon are a bandgap of 1.1 eV and a photoresponse of 10^2 .

The materials mentioned above were incorporated as the absorbing layers in *n-i-p* and *p-i-n* structured multijunction solar cells. In the case of *n-i-p* structured cells, flexible, unpolished stainless steel foils were used as cell substrates. No enhanced back reflector was applied. The doped microcrystalline layers were deposited using

PECVD at a discharge frequency of 13.56 MHz. Both n -doped layers were deposited at a substrate temperature of 200 °C. Unless indicated otherwise, the thickness of both n -layers was 50 nm. In both subcells a thin wide-bandgap amorphous silicon buffer layer was applied between the i - and p -layer. This void-rich buffer layer shortens the incubation phase for the 20 nm thick p -doped layers, which are deposited at 160 °C. Details about the doped layers are presented in table 4.1. Similarly to the tunnel-recombination junction in p - i - n / p - i - n structured tandem solar cells, a thin SiO_x layer was applied between the p - and n -layer, to enhance the recombination of charge carriers [85]. Indium-tin oxide (ITO) and silver or gold grid contacts were deposited on top of the uppermost p -layer as the top electrode. The solar cells were characterized by current-voltage and spectral response measurements. The active area of the cells was 0.13 cm².

In the case of p - i - n structured multibandgap solar cells, Asahi U-type SnO_2 :F coated glass was used as the front contact. To collect the current at the edge of the glass substrate, silver grid lines were deposited on top of the TCO-layer. All doped layers were deposited using the PECVD technique and are described in tables 4.1 and 4.3. The p -layer of the top cell consisted of wide bandgap amorphous silicon carbide with a thickness of 9 nm. On top of this p -layer, a buffer layer with a wide bandgap is deposited to reduce electron back-diffusion [86]. Both intrinsic layers consisted of hot-wire deposited thin-film silicon. Before deposition of the amorphous or microcrystalline silicon layer, the tantalum filaments were preheated at about 2000 °C to condition the filaments by evaporating as much silicon from them as possible. A microcrystalline silicon n -layer was used in the tunnel-recombination junction. Between the n - and p -layer, a thin SiO_x layer was applied to improve the recombination of the charge carriers [85]. The p - and n -doped layers of the bottom cell were either amorphous or microcrystalline, depending on the absorbing layer of the bottom cell. Finally, highly reflective silver back contacts were applied, which defined the area of the solar cells. The area of the p - i - n structured cells was $4 \times 4 \text{ mm}^2$ (0.16 cm²). Unless indicated otherwise, no mask was used to define the illuminated area of the p - i - n structured cells as the error in the measured value of the short-circuit current density is expected to be small.

8.3 Results and discussion

In this section, results on several multijunction solar cells are presented. Firstly, n - i - p structured solar cells are presented, followed by results on p - i - n structured cells. A comparison of all cells will be presented at the end of this section.

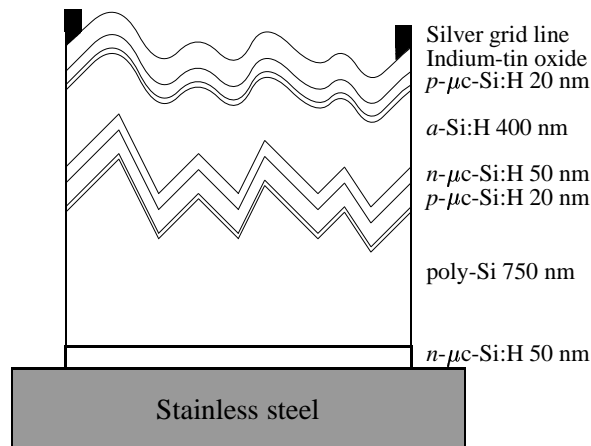


Figure 8.1: Schematic cross section of the *n-i-p/n-i-p* structured *a-Si:H/poly-Si* tandem solar cell.

8.3.1 *a-Si:H/poly-Si* tandem solar cells

Both amorphous silicon and polycrystalline silicon were applied as the absorbing layers in an *n-i-p/n-i-p* structured tandem solar cell. All doped layers were made of microcrystalline silicon. A schematic representation of the cross section of the tandem cell is shown in figure 8.1.

The AM1.5 current-voltage characteristics of the best *a-Si:H/poly-Si* solar cell are shown in figure 8.2. This cell has an open-circuit voltage of 1.18 V, a short-circuit current density of 11.4 mA/cm², and a fill factor of 0.60, resulting in an initial efficiency of 8.1 %. However, it should be noted that these values are obtained from measurements that were performed without the use of a mask. For this cell the thicknesses of the *a-Si:H* and poly-Si layers are about 200 nm and 750 nm, respectively. The open-circuit voltage of the cell of 1.18 V is a result of a V_{oc} of 0.8-0.9 V for the amorphous top cell [89], and around 0.3 V for the polycrystalline bottom cell [36]. The short-circuit current density is rather high, and compares well with the short-circuit current density of single-junction amorphous silicon cells. The relatively high initial efficiency of 8.1 % is mainly a result of this high short-circuit current density, which is strongly improved by the internal optical scattering in the polycrystalline intrinsic layer and by the surface texture of the bottom cell [111]. The fill factor, however, is not optimal, due to a high series resistance of 13.2 Ω/cm². This might be a result of the high sheet resistance of the ITO which is used for this cell.

In order to obtain information about current matching in the tandem structure, spectral response measurements were performed. The external collection efficiency of the top cell can be measured by illuminating the tandem cell with red light, which is only absorbed in the bottom cell. As a result, the total current will be limited by

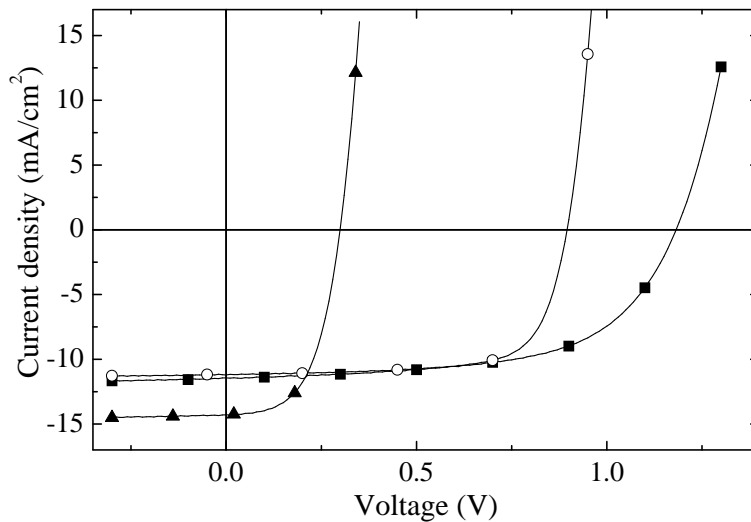


Figure 8.2: *J-V characteristics of the best a-Si:H/poly-Si tandem solar cell (■), together with the AM1.5 characteristics of the single-junction top cell (○) and bottom cell (▲).*

the top cell and therefore this cell is probed. Information about the bottom cell can then be obtained with blue light illumination.

However, in all measurements it appeared that without extra bias voltage only the top cell, and never the bottom cell, was probed. This is shown in figure 8.3, in which the external collection efficiencies measured under different illumination conditions are plotted. Different blue bandpass filters were used to avoid any top cell response, but none of these resulted in a correct signal for the bottom cell. Even without bias light, the bottom cell does not limit the current.

For spectral response measurements it is known from the literature that only under the appropriate combination of light-bias and voltage-bias the response of the top cell will be eliminated [112, 113]. By applying a positive bias voltage the working point of the subcell under investigation is shifted to short-circuit conditions. For the measurement of the bottom cell, blue bias light was applied in combination with a positive bias voltage of 0.81 V, roughly similar to the open-circuit voltage of the top cell under AM1.5 illumination (see section 2.4.2). At this value for the bias voltage, the signal obtained at 650 nm under blue bias light has its maximum. In this case, indeed some response of the bottom cell is measured, as can be seen in figure 8.3. However, the response under blue bias light is still not cut off for short wavelengths, indicating that the signal of the top cell is not completely eliminated, or, i.e., that the

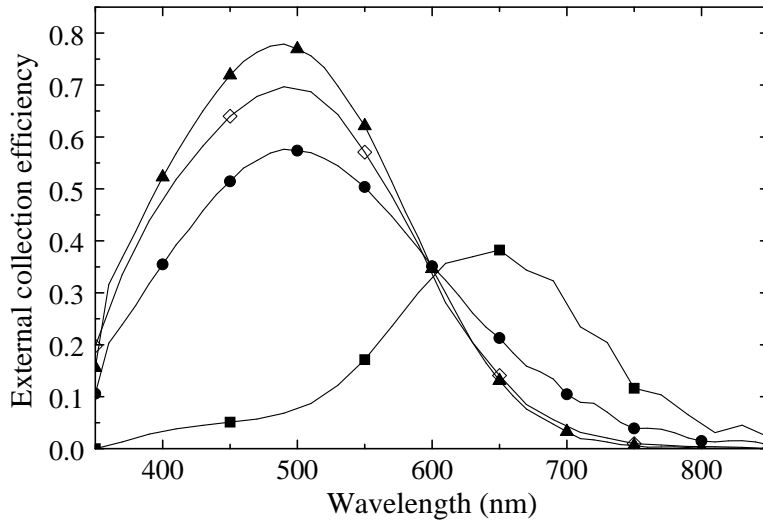


Figure 8.3: External collection efficiency of the *a*-Si:H/poly-Si tandem cell. ▲: Red bias light, bias voltage = 0 V; ◇: no bias light, bias voltage = 0 V; ●: blue bias light, bias voltage = 0 V; ■: blue bias light, bias voltage = 0.81 V.

bottom cell still transfers current from the top cell. The characteristics of most other tandem solar cells with thickness ratios of the top cell and bottom cell ranging from 200/300 nm to 400/750 nm show similar behavior.

If the spectral response measurements are assumed to be correct, a current density of 9.2 mA/cm² is generated in the top cell, while only 5.2 mA/cm² is generated in the bottom cell. These values are rather low compared to the short-circuit current density of the total tandem cell. As these spectral measurements were performed quite some time after deposition of the solar cell, it could be thought that the current generated in the amorphous cell is reduced due to degradation. However, this does not explain the low current density generated in the bottom cell, as this cell is stable as was found from light-soaking experiments. From the external collection efficiency of the bottom cell, it is clear that the (infra)red response of this cell is low and vanishes for wavelengths longer than ~ 900 nm. This loss in red light absorption is mainly caused by the small thickness of the bottom cell. In the (infra)red regime, the external collection efficiency of the bottom cell can be estimated based on the external collection efficiencies $ECE_{a-Si:H}$ and $ECE_{poly-Si}$, and is given by $(1 - ECE_{a-Si:H}) \times ECE_{poly-Si}$. In this case, the amorphous silicon single-junction cell gives a too high response due to the reflection of light by the metal substrate, which is not present in

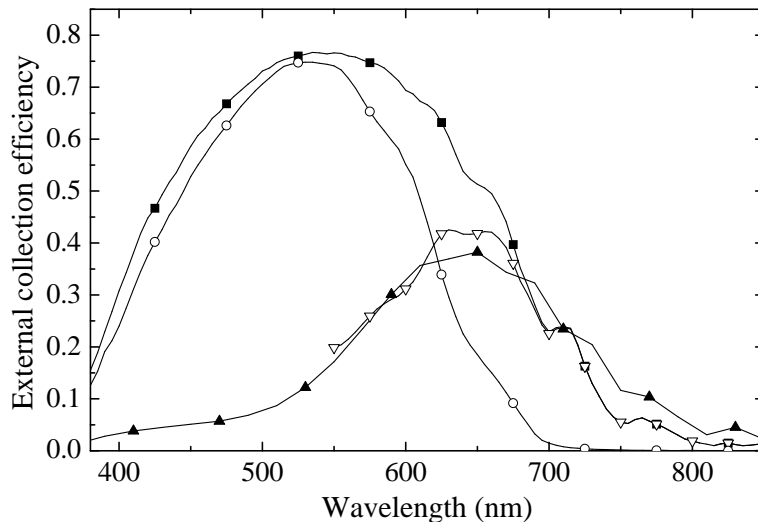


Figure 8.4: External collection efficiency of a single-junction polycrystalline silicon cell (■), a single-junction amorphous silicon cell (○), the bottom cell of an a-Si:H/poly-Si tandem cell (▲), and the minimally expected external collection efficiency of the bottom cell is shown (▽).

a tandem cell. Therefore, the estimation of the external collection efficiency gives a minimum value. Figure 8.4 shows this minimally expected external collection efficiency of the bottom cell, together with spectral response data of a polycrystalline single-junction cell, of an amorphous single-junction solar cell, and of the bottom cell of the tandem cell. In this figure, it can be seen that the expected external collection efficiency of the bottom cell corresponds roughly to the curve measured for this cell. Apparently, the current density generated in the bottom cell is indeed rather low compared to the short-circuit current density of the tandem cell under AM1.5 conditions. This difference can be explained by the further extended light scattering in the tandem cell due to the combination of the texture of the polycrystalline silicon, and the high conductivity of the microcrystalline doped layers and the stainless steel substrate. As more textured layers are present in the tandem cell, the light scattering is strongly enhanced compared to scattering in a single-junction cell. The use of diffuse light, as is used during current-voltage measurements, results in even more light-scattering. As the chopped light used for spectral response measurements has a much lower light intensity than the AM1.5 spectrum, and also because the light is not diffuse, the spectral response measurements of the bottom cell underestimate the external collection efficiency, and thus the generated current of this cell.

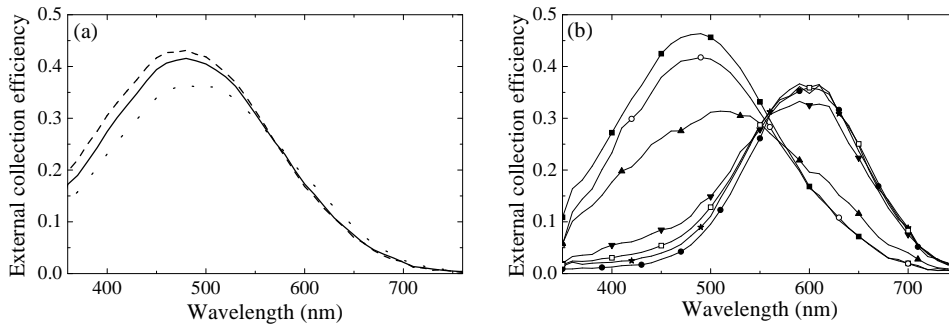


Figure 8.5: (a) External collection efficiency of an $a\text{-Si:H}/a\text{-Si:H}$ $n\text{-i-p}/n\text{-i-p}$ structured solar cell without bias voltage. —: No bias light; ---: red bias light; - - -: blue bias light. (b) External collection efficiency of the same solar cell measured without bias light, for bias voltages of 0 V (■), 0.5 V (○), 0.7 V (▲), 0.9 V (▼), 1.0 V (□), 1.1 V (★), and 1.3 V (●).

In order to improve the red response of the polycrystalline silicon subcell, a new tandem cell was made, in which the thickness of the polycrystalline silicon layer was 1500 nm instead of 750 nm. The cell had a similar structure as shown earlier in figure 8.1, but the thickness of the microcrystalline n -layer in the tunnel-recombination junction was reduced to 30 nm. For this cell structure, the external collection efficiency of the bottom cell could be measured without bias voltage for a number of solar cells. However, in the dark, most of the solar cells behaved similarly as shown in figure 8.3. However, for a few solar cells, it was possible to measure a correct dark external collection efficiency, as the one shown in figure 2.8. From these results, it seems that the thickness of the n -layer in the tunnel-recombination junction is of influence on the behavior of the tandem cells under low-light conditions.

In order to exclude any negative influence on the bottom cell of (atomic) hydrogen dilution during deposition of the top cell, a new $a\text{-Si:H}/\text{poly-Si}$ tandem cell was made. For this cell, the absorbing layer of the top cell was deposited using the plasma-enhanced CVD technique. The substrate temperature during deposition of this layer was 200 °C. Unfortunately, the incorporation of this layer did not lead to different behavior of the bottom cell under low light conditions as used in spectral response measurements.

8.3.2 $a\text{-Si:H}/a\text{-Si:H}$ tandem solar cells

A tandem structure in which the polycrystalline absorbing layer of the bottom cell was replaced by a hot-wire deposited amorphous layer ($a\text{-Si:H}/a\text{-Si:H}$ tandem cell) was briefly discussed in section 4.2.2. A cross section of this cell was shown in fig-

ure 4.6. Unfortunately, the cell showed similar external collection efficiency results as the first tandem cell with a polycrystalline bottom cell. This is shown in figure 8.5(a), in which the external collection efficiencies measured under different illumination conditions are plotted without the use of bias voltage. Ideally, the response without bias light is always limited by one of the two cells. Therefore, the external collection efficiency should be equal to the lowest of the two responses. However, the measurements show that this is not the case, as the bottom cell does not limit the current for short wavelengths. However, by applying a positive bias voltage during spectral response measurements in the dark, the signal of the top cell decreases and the signal of the bottom cell appears, as can be seen in figure 8.5(b). The external collection efficiencies of the top and bottom cell, measured using red and blue bias illumination, are shown in figure 4.7. As was already mentioned in section 4.2.2, also for this cell the current generated in the bottom cell, as measured by spectral response measurements, is lower than the short-circuit current density of the tandem cell. Again, this current is underestimated due to the reduced light-scattering during spectral response measurements.

As a thinner microcrystalline n -layer in the tunnel-recombination junction had a beneficial effect on the spectral response measurements of a -Si:H/poly-Si tandem cells, a new a -Si:H/ a -Si:H tandem cell was made with a 20 nm thick n -layer. For this cell, the spectral response of the bottom cell could again be measured without the use of bias voltage. However, the response in the dark was still not limited by the bottom cell for short wavelengths, as can be seen in figure 8.6. Unfortunately, aged wires were used for the deposition of this cell, and the thicknesses of the absorbing layers were lower than was aimed for. As a result, the current densities generated in the subcells are low ($\sim 4 \text{ mA/cm}^2$). The results on this cell again show that the thickness of the n -layer in the tunnel-recombination junction is of influence on the behavior of the tandem cells under the low-light conditions during spectral response measurements.

8.3.3 a -Si:H/ $\mu\text{c-Si:H}$ tandem solar cells

Also microcrystalline silicon was incorporated in the bottom cell of a multibandgap tandem solar cell. A hydrogen dilution of 0.935 was used during deposition. The cell structure was similar to that of the a -Si:H/poly-Si tandem cell shown in figure 8.1, but the polycrystalline silicon layer was replaced by a $1.5 \mu\text{m}$ thick microcrystalline silicon layer. Furthermore, the thickness of the amorphous silicon absorbing layer of the top cell was 200 nm. Table 8.1 gives an overview of the parameters of the best cell, which had an initial efficiency of 6.1 %. Again, the open-circuit voltage corresponds well to the sum of the open-circuit voltage of the top cell and (a slightly lower value than) the open-circuit voltage of the bottom cell. With the use of a mask, the short-circuit current density decreased by about 10 %. In contrast to expectation,

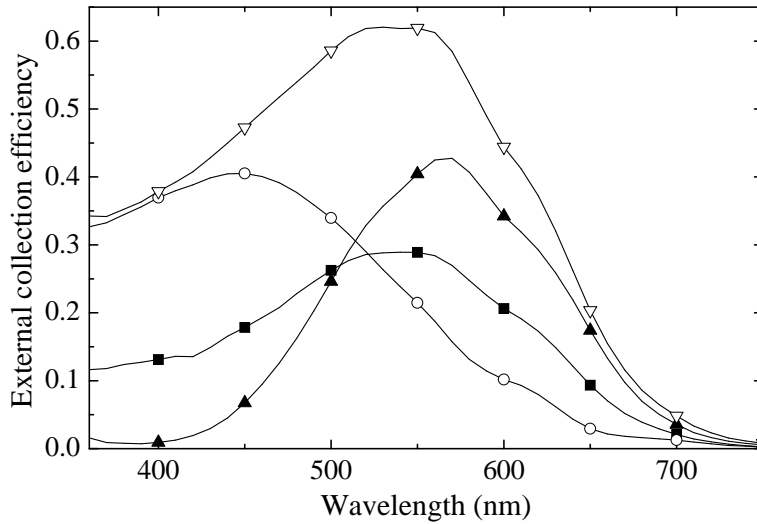


Figure 8.6: External collection efficiency of the best *a*-Si:H/*a*-Si:H *n-i-p/n-i-p* structured tandem solar cell with a 20 nm thick *n*-layer in the tunnel-recombination junction. No bias voltage was used. ■: No bias light; ○: top cell, measured using red bias light; ▲: bottom cell, measured using blue bias light; ▽: total. A current density of 4.1 mA/cm² is generated in the top cell, whereas a current density of 4.4 mA/cm² is generated in the bottom cell.

also the fill factor decreased slightly.

Figure 8.7 shows the results from spectral response measurements. Similarly to the external collection efficiencies of the *a*-Si:H/poly-Si and the *a*-Si:H/*a*-Si:H tandem cells, the application of a bias voltage of 0.94 V was necessary to obtain the response from the bottom cell. From the spectral response measurements, it is calculated that a current density of 7.1 mA/cm² is generated in the top cell, whereas a current density of 6.2 mA/cm² is generated in the bottom cell. The current density generated in the top cell corresponds well with the short-circuit current density of

Table 8.1: Solar cell parameters of the best *a*-Si:H/ μ c-Si:H *n-i-p/n-i-p* structured solar cell, measured both with and without a mask.

Mask	V_{oc} (V)	J_{sc} (mA/cm ²)	FF	η (%)	R_s (Ω cm ²)	R_p (k Ω cm ²)
No	1.31	7.9	0.67	7.0	14	2.2
Yes	1.32	7.2	0.64	6.1	18	2.1

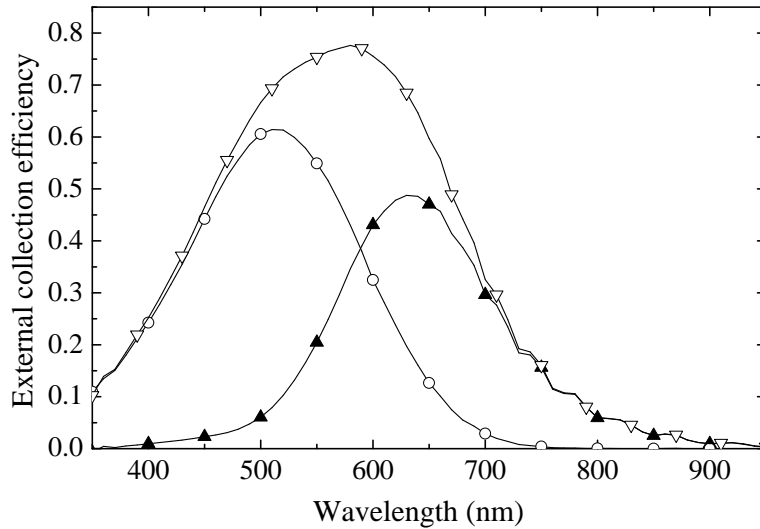


Figure 8.7: External collection efficiency of the best $a\text{-Si:H}/\mu\text{c-Si:H}$ $n\text{-i-p}/n\text{-i-p}$ structured tandem solar cell. ○: Top cell, measured using red bias light; ▲: bottom cell, measured using blue bias light, $V_{\text{bias}} = 0.94$ V; ▽: total. A current density of 7.1 mA/cm^2 is generated in the top cell, whereas a current density of 6.2 mA/cm^2 is generated in the bottom cell.

the total tandem solar cell, measured using a mask. However, the current density generated in the bottom cell is 14 % lower than this value, again indicating that the response of the bottom cell can not be measured properly using the current spectral response setup.

Figure 8.8 shows the dark current-voltage characteristics of different $a\text{-Si:H}/\mu\text{c-Si:H}$ tandem solar cells. It is clear that for three of the cells two plateaus exist in the characteristics. These plateaus correspond to regions where one of the two subcells is limiting the current. At voltages between about 0.9 V and 1.1 V, a different sub-cell is limiting the current than at voltages below 0.5 V. This agrees with the results from spectral response measurements, in which the application of a bias voltage is necessary to obtain a correct response.

8.3.4 $a\text{-Si:H}/\mu\text{c-Si:H}/\mu\text{c-Si:H}$ triple solar cells

Although there are some current leakage paths in the $n\text{-i-p}$ structured tandem solar cells, high open-circuit voltages and fill factors are obtained. To test the concept of absorbing an even larger part of the solar spectrum, hot-wire deposited intrinsic layers

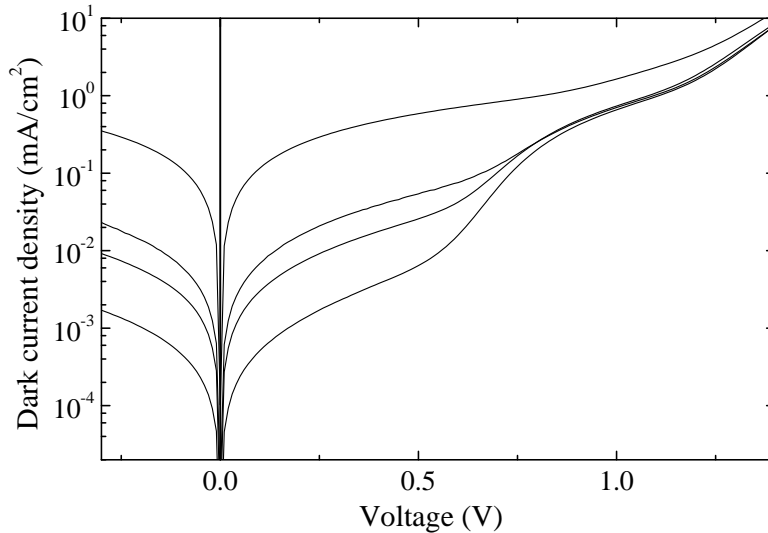


Figure 8.8: Dark current density of several $a\text{-Si:H}/\mu\text{c-Si:H}$ $n\text{-i-p}/n\text{-i-p}$ structured solar cells.

were also applied in a triple-junction solar cell on stainless steel. In the top cell, a 165 nm thick absorbing layer of medium-temperature deposited amorphous silicon was incorporated. The middle and bottom cells consisted of microcrystalline silicon made at a hydrogen dilution of 0.935. The thicknesses of these layers were 660 nm and 1350 nm, respectively. All n -doped layers were made of microcrystalline silicon and had a thickness of 50 nm. Also the p -doped layers were microcrystalline, with a thickness of 20 nm. In both tunnel-recombination junctions, a thin SiO_x -layer was applied between the p - and n -layer. Indium-tin oxide (ITO) and gold grid contacts served as the front electrode. The best triple cell had an open-circuit voltage of 1.73 V, a short-circuit current density of 7.5 mA/cm^2 , and a fill factor of 0.66, resulting in an initial efficiency of 8.5 %. However, it should be noted that these results were obtained from measurements without the use of a mask. Different measurements in which a mask was used yielded strongly varying results, but in all cases a reduction of all solar cell parameters was found.

Figure 8.9 shows the external collection efficiency of the best triple cell without the use of bias light, but with the use of bias voltage. Similar to the characteristics of the $a\text{-Si:H}/a\text{-Si:H}$ tandem cell shown in figure 8.5(b), a strong dependence of the collection efficiency on the bias voltage was found. At low bias voltages, the signal corresponds to the response of the top cell. At higher voltages, a signal arises which resembles the response of the middle cell, and at voltages around 1.4-1.7 V the signal

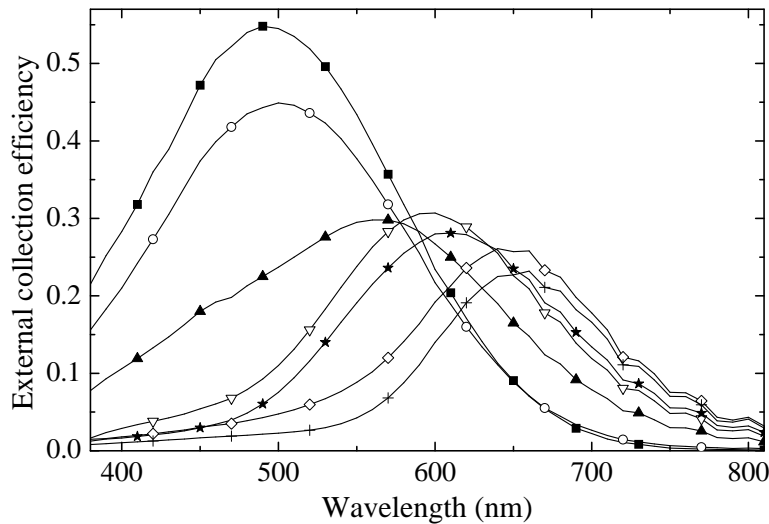


Figure 8.9: External collection efficiency of the best $a\text{-Si:H}/\mu\text{c-Si:H}/\mu\text{c-Si:H}$ multi-bandgap triple-junction solar cell, measured without bias light. The applied bias voltages are 0 V (■), 0.65 V (○), 0.8 V (▲), 1.0 V (▽), 1.2 V (★), 1.4 V (◇), and 1.7 V (+).

resembles the response of the bottom cell. However, as the bias voltages at which the middle cell and the bottom cell should be measured are not known, the exact external collection efficiencies of these cells can not be properly measured. In tandem solar cells, a similar problem exists. However, it turned out that, for these cells, the current density generated in the top cell corresponded well with the short-circuit current density of the entire cell. In the case of the triple-junction cell, the current density generated in the top cell is equal to 6.3 mA/cm^2 , which is about 84 % of the short-circuit current density of the total cell. This difference can be explained by the absence of a mask during the current-voltage measurements.

Based on the results on $n\text{-i-p}$ structured tandem and triple solar cells, some general remarks can be made. Firstly, the open-circuit voltages of all multijunction $n\text{-i-p}$ structured solar cells had a value which was expected based on the open-circuit voltages of the separate subcells. Secondly, in almost all tandem cells the current through the device was limited by the top cell when low bias voltages were used. This means that the current due to low-intensity monochromatic light can leak through the bottom cell, and, in the case of a triple-junction cell, also through the middle cell. Only when a positive bias voltage was used, a response closer to the expected response of the bottom and/or middle cell could be measured. As the same behavior was seen

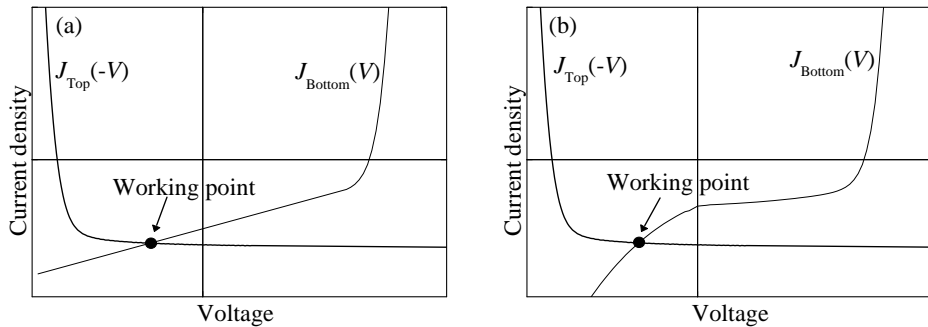


Figure 8.10: Illustration of the effect of different current leakage paths in the bottom cell of a tandem solar cell on the position of the working point during spectral response measurements. No bias voltage is applied and the bottom cell is probed. (a) The bottom cell has a low parallel or shunt resistance. (b) The bottom cell junction “breaks down” at low (negative) voltages.

using polycrystalline silicon, amorphous silicon and microcrystalline silicon bottom cells, it is logical to assume that all current leakage effects in the different solar cells have the same origin.

Fortunately, this effect did not significantly affect the current-voltage characteristics under AM1.5 illumination, as high fill factors were obtained, e.g. 0.71 in the case of an $a\text{-Si:H}/a\text{-Si:H}$ tandem cell. Thus, under high light intensities, the shunting behavior is virtually absent. However, measurements of the external collection efficiency of tandem cells and, especially, of triple cells were ambiguous. To determine conditions necessary for current-matching of the subcells, it is crucial that there is no leakage of current in one of the subcells.

There are several possible explanations for the current leakage in the bottom cell. The first explanation is the presence of a low parallel or shunt resistance in the bottom cell, as is schematically depicted in figure 8.10(a). If this is the case, the current that can flow through the bottom cell depends strongly on the applied voltage. At low voltages, the current in a tandem cell is limited by the top cell, as can be seen in figure 8.10(a). It is possible that this low shunt resistance is only exposed at low light intensities, as used during spectral response measurements, but not under AM1.5 illumination, as used during current-voltage measurements. Another explanation is (reversible) junction breakdown of the bottom cell [114, 115], as is schematically depicted in figure 8.10(b). When a junction “breaks down”, it will conduct a very large current when a sufficiently high electric field is applied. Also this effect results in a limitation of the current by the top cell. In both cases, the bottom cell is limiting the current only if a certain positive bias voltage is applied. Furthermore, for both

explanations the AM1.5 characteristics of the tandem cell are not influenced significantly, which corresponds to the results of the measurements presented earlier in this chapter.

Neither shunting behavior, nor junction breakdown was observed during current-voltage measurements of single-junction *n-i-p* structured solar cells. However, it is possible that (one of) these effects are induced in the bottom cell during deposition of (one of the layers of) the top cell. This can for instance be caused by a too high deposition temperature of one of the layers of the top cell, or by (atomic) hydrogen diffusion during hot-wire deposition of the absorbing layer of the top cell. Furthermore, it turned out that the thickness of the microcrystalline *n*-layer in the tunnel-recombination junction is of influence on the tandem cell behavior. Further investigations were performed on *p-i-n* structured tandem solar cells. Results on these cells are presented in the next section.

8.3.5 Tandem solar cells with *p-i-n/p-i-n* structure

In order to improve the red response of the solar cells, hot-wire deposited silicon thin films were also incorporated in *p-i-n/p-i-n* structured tandem solar cells. Both an *a*-Si:H/*a*-Si:H and an *a*-Si:H/ μ c-Si:H tandem cell were made. Most details on the cell structures are described in section 8.2. In the *a*-Si:H/*a*-Si:H tandem cell, both absorbing layers were made of hot-wire deposited amorphous silicon made at 220 °C. In this case, a filament current of 10.0 A was used. In the top cell, an amorphous silicon carbide *p*-layer and a microcrystalline silicon *n*-layer were applied, with thicknesses of 9 nm and 25 nm, respectively. Between the intrinsic layer and the *n*-doped layer a thin oxide layer was incorporated. The bottom cell contained an amorphous silicon carbide *p*-layer and an amorphous silicon *n*-layer, with thicknesses of 9 nm and 20 nm, respectively. In the *a*-Si:H/ μ c-Si:H tandem cell, the bottom cell contained a microcrystalline absorbing layer, which was deposited at 250 °C, using a hydrogen dilution of 0.952. The amorphous silicon absorbing layer in the top cell was deposited at 220 °C. For this tandem cell, the top cell incorporated an amorphous silicon carbide *p*-layer with a thickness of 9 nm, and a microcrystalline silicon *n*-layer with a thickness of 17 nm. The bottom cell contained a microcrystalline silicon *p*-layer and a microcrystalline *n*-layer, with thicknesses of 20 nm and 17 nm, respectively.

The solar cell parameters of the best cells are given in table 8.2. The amorphous silicon tandem cell had a high open-circuit voltage and a high fill factor, but the short-circuit current density was low. Nevertheless, an initial efficiency of 8.2 % was obtained. In contrast to this, the *a*-Si:H/ μ c-Si:H tandem cell had an extremely high short-circuit current density and efficiency and a very low fill factor. The open-circuit voltage of 1.36 V was expected based on the results of the subcells. The main reason for the extremely high short-circuit current density is the fact that the cell area was not properly defined by back-etching of the contacts. Due to the high conductivity of the

Table 8.2: Solar cell parameters of the best *p-i-n/p-i-n* structured solar cells.

Cell	$d_{i\text{-layers}}$ (nm)	V_{oc} (V)	J_{sc} (mA/cm ²)	FF	η (%)
<i>a</i> -Si:H/ <i>a</i> -Si:H	70/500	1.70	6.7	0.71	8.2
<i>a</i> -Si:H/ μ c-Si:H	170/2000	1.36	(19.0)	0.47	(12.2)

microcrystalline doped layers, carriers that are generated by scattered light can still be collected, which results in a high short-circuit current density. As the doped layers in the amorphous silicon tandem cell are amorphous, this problem occurs less in these cells. Masking of the *a*-Si:H/ μ c-Si:H cell resulted in a large decrease of the short-circuit current density to values around 9 mA/cm². However, the fill factor increased only slightly ($\sim 5\%$), probably indicating that the cells are not well matched.

Figure 8.11 shows the external collection efficiency of the best *a*-Si:H/*a*-Si:H tandem cell, together with the results of a *p-i-n* structured single-junction cell with a 500 nm thick amorphous silicon layer. It is clear that for this tandem cell, the dark response behaves exactly as expected, and is equal to the minimum of the responses of the top and bottom cells. Furthermore, in contrast to *n-i-p* structured tandem solar cells, no bias voltage is needed to measure the response of the bottom cell, indicating an adequately high parallel resistance of this cell. Both the top cell and the bottom cell generate a current density of 6.3 mA/cm², indicating that the cells are well matched. Furthermore, these values correspond well with the short-circuit current density of the tandem cell, given in table 8.2. However, comparing the response of the single-junction cell to the total response of the tandem cell, it turns out that the green response and the (infra)red response of the tandem cell are not optimal. This is probably the result of losses in the tunnel-recombination junction and of a smaller thickness of the bottom cell, respectively. The blue response of the tandem cell is slightly higher than that of the single-junction cell, which is the result of a better collection of charge carriers in the thinner top cell.

In figure 8.12, the external collection efficiency of the best *a*-Si:H/ μ c-Si:H tandem solar cell is shown. Again, both the dark response and the response under blue bias illumination can be measured well, without the use of bias voltage. This result indicates again the sufficiently high shunt resistance of the bottom cell. The top cell generates a current density of 9.1 mA/cm², while the current density generated in the bottom cell is only 8.3 mA/cm². These values correspond with the values for the short-circuit current density measured when a mask is used. However, the difference in current density generated in the bottom cell and that generated in the top cell shows that the subcells are not ideally matched. In order to improve the current generated in the bottom cell, this cell should be made thicker.

The results on *p-i-n/p-i-n* structured tandem solar cells show that it is possible to incorporate hot-wire deposited silicon thin films as the absorbing layer in *p-i-n*

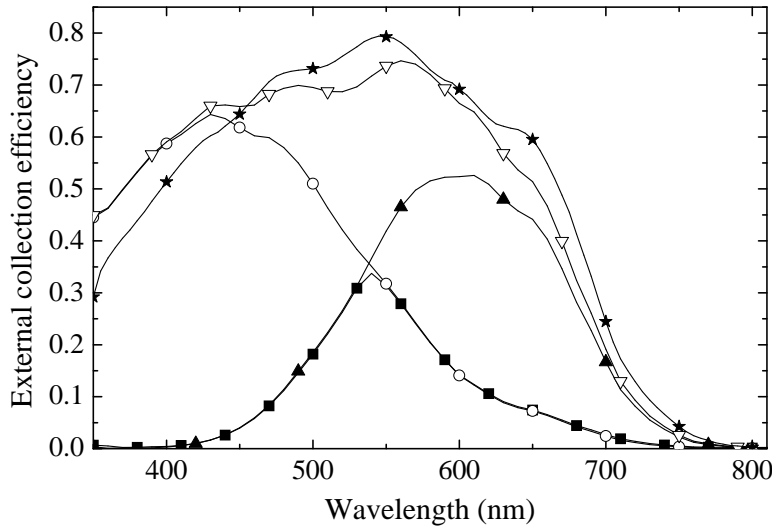


Figure 8.11: External collection efficiency of an $a\text{-Si:H}/a\text{-Si:H}$ $p\text{-i-n}/p\text{-i-n}$ structured solar cell. ■: No bias light; ○: top cell, measured using red bias light; ▲: bottom cell, measured using blue bias light; ▽: total. Also the external collection efficiency of a single-junction amorphous silicon $p\text{-i-n}$ structured solar cell is given (★).

cells. High open-circuit voltages are obtained and, in the case of amorphous silicon tandem cells, also the fill factors are high with values of over 0.7. In the case of an $a\text{-Si:H}/\mu\text{c-Si:H}$ tandem cell, the short-circuit current density and the fill factor are strongly influenced by the fact that the cell area is not properly defined, which could be obtained, e.g., by back-etching of the contacts. In contrast to $n\text{-i-p}/n\text{-i-p}$ structured tandem cells, it is not necessary to apply a bias voltage to perform spectral response measurements on $p\text{-i-n}/p\text{-i-n}$ structured tandem solar cells. Apparently, the current leakage path that is present in the bottom cell of $n\text{-i-p}/n\text{-i-p}$ structured tandem solar cells is not present in $p\text{-i-n}/p\text{-i-n}$ structured tandem cells. This result is especially remarkable for $a\text{-Si:H}/\mu\text{c-Si:H}$ tandem solar cells, as both the $n\text{-i-p}/n\text{-i-p}$ structure and the $p\text{-i-n}/p\text{-i-n}$ structure contained the same doped layers. Only the order of depositions was reversed for the two solar cell structures. In both cases, the absorbing layers of the subcells that were deposited secondly were made at the same deposition temperature (250 °C). Therefore, a too high substrate temperature of the absorbing layer can be excluded as the primary reason for the current leakage in the bottom cell of $n\text{-i-p}/n\text{-i-p}$ structured solar cells.

Based on a similar argument, in combination with the fact that plasma-enhanced

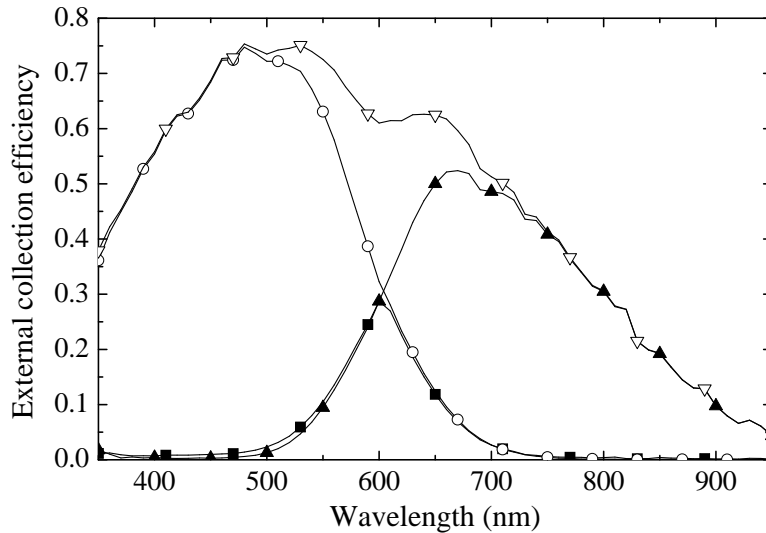


Figure 8.12: External collection efficiency of an $a\text{-Si:H}/\mu\text{c-Si:H}$ $p\text{-i-n}/p\text{-i-n}$ structured solar cell. ■: No bias light; ○: top cell, measured using red bias light; ▲: bottom cell, measured using blue bias light; ▽: total.

deposition of the top cell does not result in proper spectral response measurements, also the effect of (atomic) hydrogen diffusion can be excluded as the main reason for the behavior of $n\text{-i-p}/n\text{-i-p}$ structured tandem solar cells during spectral response measurements. As neither the deposition temperature of the absorbing layer of the top cell, nor the presence of atomic hydrogen during this deposition has significant influence on the solar cell behavior during (dark) spectral response measurements, it is concluded that the current leakage problem is not created during the deposition of this layer.

As it has been excluded that the deposition of the p -layer of the top $n\text{-i-p}$ cell has any influence on the behavior of the bottom cell, it is concluded that the deposition conditions of the n -layer of the top cell or the application of the thin SiO_x layer in the tunnel-recombination junction affects the bottom cell. It seems that the fact that a microcrystalline silicon tunnel-recombination junction works well in $p\text{-i-n}/p\text{-i-n}$ structured tandem cells does not automatically mean that a similar structure works for $n\text{-i-p}/n\text{-i-p}$ cells as well. Possible reasons for the deterioration of the p -layer are intermixing of dopants of the p - and n -layer in the tunnel-recombination junction, boron diffusion into the intrinsic layer during n -layer deposition, damage due to ion bombardment during n -layer deposition, or plasma-induced diffusion. Furthermore, it is clear that the deposition of n -layer has this effect only on the underlying p -layer,

as the results from $p-i-n/p-i-n$ structures show that the deposition of a microcrystalline n -layer directly on an intrinsic layer does not deteriorate the i -layer. Therefore, the optimization of the tunnel-recombination junction is a key issue for further improvement of the energy conversion efficiency of $n-i-p$ structured multijunction solar cells.

8.4 Conclusions

In this chapter, the incorporation of hot-wire deposited amorphous silicon, polycrystalline silicon and microcrystalline silicon as the absorbing layers in multibandgap tandem cells was demonstrated. Both $n-i-p/n-i-p$ and $p-i-n/p-i-n$ structured solar cells were made. For all multijunction solar cells, the open-circuit voltage had a value that can be expected based on the open-circuit voltages of the individual subcells.

In the case of $n-i-p$ structured tandem cells, spectral response measurements revealed that a current leakage path in the dark or under low-light illumination conditions was present in the bottom cell. Somehow, this path is created when the top $n-i-p$ cell is deposited. Fortunately, this effect did not significantly influence the AM1.5 current-voltage characteristics. However, optimization of the current-matching of the subcells is strongly hindered by the presence of this leakage path. From different measurements, it is concluded that an unoptimized tunnel-recombination junction is the main cause for the current leakage.

Furthermore, the short-circuit current densities generated in the bottom cell, as measured during spectral response measurements, were low compared to the short-circuit current densities of the tandem cells. The high light intensities during current-voltage measurements, in combination with the use of diffuse light, resulted in a strong light scattering in a tandem cell. The charge carriers that were generated well outside the cell area could still be collected due to the high conductivity of the doped layers. In contrast to this, spectral response measurements are performed under low-light illumination conditions, without the use of diffuse light. Therefore, spectral response measurements underestimate the external collection efficiency, and thus the generated photocurrent, of the bottom cell. As a result, it is difficult to obtain the real values of the current generated in the bottom cell.

In $p-i-n$ structured tandem cells, no current leakage path was present in the bottom cell. Monobandgap amorphous silicon tandem cells had an open-circuit voltage of 1.7 V and a high fill factor of 0.71, resulting in an initial efficiency of 8.2 %. In the case of $a\text{-Si:H}/\mu\text{c-Si:H}$ tandem solar cells, the short-circuit current density and the fill factor were strongly influenced by the fact that the cell area was not properly defined by the use of a mask and by back-etching of the contacts. The efficiency of $p-i-n/p-i-n$ structured cells can be increased by optimization of the thicknesses of the absorbing layers.

These results demonstrate the large potential of hot-wire deposited intrinsic sili-

con for the application in multibandgap solar cells. It is expected that the optimization of the tunnel-recombination junction, as well as the application of a highly reflective back contact, will result in a significant increase in the (initial) efficiency of *n-i-p* structured multijunction solar cells. For both *n-i-p* and *p-i-n* structured solar cells, further improvement can be achieved by the incorporation of thicker absorbing layers, which results in a higher short-circuit current density. With these improvements, it should be possible to obtain efficiencies of well over 10 % for hot-wire deposited solar cells.

9

General conclusions and perspectives

The hot-wire chemical vapor deposition technique was used for the deposition of high-quality amorphous and microcrystalline silicon layers and solar cells. Using tantalum as filament material, it was possible to reduce the deposition temperature to values around 250 °C, while the device quality of amorphous silicon was maintained. At these low temperatures, the formation of silicides on the filaments is enhanced, which resulted in a deterioration of amorphous silicon material and solar cell quality. By preheating the filaments at elevated temperature before deposition, the silicides were evaporated from the filaments as much as possible, resulting in an improvement of the material quality.

High-quality microcrystalline silicon can be made at moderate temperatures, using a proper hydrogen dilution during deposition. At too low hydrogen dilutions, the layers are amorphous, or the structure is not homogeneous and the crystallinity decreases with thickness. At too high hydrogen dilutions, the layers are porous and oxidize in air. Optimization of the filament properties is necessary for the deposition of homogeneous material.

Application of hot-wire deposited films as the absorbing layer in single-junction *n-i-p* structured solar cells resulted in high initial efficiencies of 7.2 % for amorphous silicon and 4.8 % for microcrystalline silicon. These values were obtained without application of light-trapping features like a back reflector or textured contacts. Furthermore, shunting problems that were present in these devices were solved. The efficiencies of the solar cells can be improved further by the optimization of the TCO/*p*-layer front contact, and by applying a textured back reflector. In this way, both the blue and the red response of the solar cells can be increased.

For eventual production purposes, it is necessary that the thickness uniformity of the deposition is improved. This can be done by choosing a proper filament design, with multiple filaments distributed over a large area. Also the deposition rate has to be increased further. For hot-wire deposition, the deposition rate is mainly determined by the filament temperature. As the substrate temperature is also determined by the filament temperature, a high deposition rate can conflict with low-temperature deposition. This problem may be solved by an increase of the distance between the substrate and the filaments, or by the use of thinner wires.

Preliminary results on *n-i-p/n-i-p* structured tandem solar cells show that it is possible to obtain high open-circuit voltages and high fill factors, but an improvement of the tunnel-recombination junction is necessary for optimization of the current-matching of the subcells. The highest achieved initial efficiency for a tandem cell

was over 8 %. These results show the large potential of hot-wire deposited thin-film silicon for the application in (multijunction) solar cells.

References

- [1] J. Zhao, A. Wang and M. A. Green, *Sol. Energy Mat. and Sol. Cells* **65**, 429 (2001).
- [2] M. J. Powell and S. C. Deane, *Phys. Rev. B* **48**, 10815 (1993).
- [3] D. L. Staebler and C. R. Wronski, *Appl. Phys. Lett.* **31**, 292 (1977).
- [4] R. J. Koval, J. Koh, Z. Lu, L. Jiao, R. W. Collins and C. R. Wronski, *Appl. Phys. Lett.* **75**, 1553 (1999).
- [5] P. Roca i Cabarrocas, *J. Non-Cryst. Sol.* **266-269**, 31 (2000).
- [6] E. Vallat-Sauvain, U. Kroll, J. Meier, A. Shah and J. Pohl, *J. Appl. Phys.* **87**, 3137 (2000).
- [7] R. E. I. Schropp, B. Stannowski, A. M. Brockhoff, P. A. T. T. van Veenendaal and J. K. Rath, *Mater. Phys. Mech.* **1**, 73 (2000).
- [8] D. V. Tsu, B. S. Chao, S. R. Ovshinsky, S. Guha and J. Yang, *Appl. Phys. Lett.* **71**, 1317 (1997).
- [9] R. E. I. Schropp, K. F. Feenstra, E. C. Molenbroek, H. Meiling and J. K. Rath, *Phil. Mag. B* **76**, 309 (1997).
- [10] M. Fonrodona, D. Soler, J. M. Asensi, J. Bertomeu and J. Andreu, *J. Non-Cryst. Sol.* **299-302**, 14 (2002).
- [11] M. Hack and M. Shur, *J. Appl. Phys.* **58**, 997 (1985).
- [12] C. E. Nebel, R. A. Street, W. B. Jackson and N. M. Johnson, *J. Non-Cryst. Sol.* **164-166**, 203 (1993).
- [13] J. Wallinga, W. M. Arnold Bik, A. M. Vredenberg, R. E. I. Schropp and W. F. van der Weg, *J. Phys. Chem. B* **102**, 6219 (1998).
- [14] K. Yamamoto, A. Nakajima, M. Yoshimi, T. Sawada, S. Fukuda, K. Hayashi, T. Suezaki, M. Ichikawa, Y. Koi, M. Goto, H. Takata and Y. Tawada, *Proceedings of the 29th IEEE Photovoltaic Specialists Conference*, New Orleans, USA, May 20-24, 2002.
- [15] S. Guha, *High Efficiency Triple-Junction Amorphous Silicon Alloy Photovoltaic Technology: Annual Technical Progress Report 1998-1999*, NREL/SR-520-26648, July 1999.
- [16] R. S. Crandall and W. Luft, *Prog. Photovolt: Res. Appl.* **3**, 315 (1995).
- [17] A. Matsuda, K. Nomoto, Y. Takeuchi, A. Suzuki, A. Yuuki and J. Perrin, *Surf. Sci.* **227**, 50 (1990).
- [18] R. E. I. Schropp and M. Zeman, *Amorphous and microcrystalline silicon solar cells: modeling, materials and device technology*, Kluwer academic publishers, Boston, 1998.

- [19] F. Finger, U. Kroll, V. Viret, A. Shah, W. Beyer, X.-M. Tang, J. Weber, A. Howling and Ch. Hollenstein, *J. Appl. Phys.* **71**, 5665 (1992).
- [20] R. J. Severens, G. J. H. Brussaard, M. C. M. van de Sanden and D. C. Schram, *Appl. Phys. Lett.* **67**, 491 (1995).
- [21] H. Wiesmann, A. K. Gosh, T. McMahon and M. Strongin, *J. Appl. Phys.* **50**, 3752 (1979).
- [22] H. Matsumura, *J. Appl. Phys.* **65**, 4396 (1989).
- [23] A. H. Mahan, J. Carapella, B. P. Nelson, R. S. Crandall and I. Balberg, *J. Appl. Phys.* **69**, 6728 (1991).
- [24] K. F. Feenstra, R. E. I. Schropp and W. F. van der Weg, *J. Appl. Phys.* **85**, 6843 (1999).
- [25] B. Schröder, U. Weber, H. Seitz, A. Ledermann and C. Mukherjee, *Thin Solid Films* **395**, 298 (2001).
- [26] H. Matsumura, *Jpn. J. Appl. Phys.* **25** (12), L949 (1986).
- [27] B. P. Nelson, E. Iwaniczko, A. H. Mahan, Q. Wang, Y. Xu, R. S. Crandall and H. M. Branz, *Thin Solid Films* **395**, 292 (2001).
- [28] M. Vaněček, A. H. Mahan, B. P. Nelson and R. S. Crandall, in: L. Guimarães, W. Palz, C. De Reyff, H. Kiess and P. Helm (Eds.), *Proceedings of the 11th European Photovoltaic Solar Energy Conference*, Montreux, Switzerland, October 12-16, 1992, p. 96.
- [29] M. Vaněček, Z. Remeš, J. Fric, R. S. Crandall and A. H. Mahan, in: R. Hill, W. Palz and P. Helm (Eds.), *Proceedings of the 12th European Photovoltaic Solar Energy Conference*, Amsterdam, The Netherlands, April 11-15, 1994, p. 354.
- [30] A. H. Mahan, E. Iwaniczko, B. P. Nelson, R. C. Reedy Jr. R. S. Crandall, S. Guha and J. Yang, *Proceedings of the 25th IEEE Photovoltaic Specialists Conference*, Washington, D.C., USA, May 13-17, 1996, p. 1065.
- [31] P. Alpuim, V. Chu and J. P. Conde, *J. Non-Cryst. Sol.* **266-269**, 110 (2000).
- [32] H. Matsumura, *Thin Solid Films* **395**, 1 (2001).
- [33] M. K. van Veen and R. E. I. Schropp, *Appl. Phys. Lett.* **82**, 287 (2003). See also chapter 5.
- [34] K. F. Feenstra, *Hot-wire chemical vapour deposition of amorphous silicon and the application in solar cells*, Ph.D. thesis, Utrecht University, The Netherlands, 1998.
- [35] P. A. T. T. van Veenendaal, O. L. J. Gijzeman, J. K. Rath and R. E. I. Schropp, *Thin Solid Films* **395**, 194 (2001).
- [36] R. E. I. Schropp and J. K. Rath, *IEEE Trans. Electron Dev.* **46**, 2069 (1999).
- [37] S. Tange, K. Inoue, K. Tonokura and M. Koshi, *Thin Solid Films* **395**, 42 (2001).
- [38] H. L. Duan, G. A. Zaharias and S. F. Bent, Extended Abstract for the 2nd International Conference on Cat-CVD (Hot-Wire CVD) Process, Denver, USA, September 10-13, 2002, p. 121. To be published in *Thin Solid Films* (2003).

- [39] D. R. Lide (Ed.), *CRC Handbook of chemistry and physics*, 74th edition, CRC Press, Boca Raton, 1993.
- [40] J. Doyle, R. Robertson, G. H. Lin, M. Z. He and A. Gallagher, *J. Appl. Phys.* **64**, 3215 (1988).
- [41] J. K. Holt, M. Swiatek, D. G. Goodwin and H. A. Atwater, in: J. D. Cohen, J. R. Abelson, H. Matsumura and J. Robertson (Eds.), *Amorphous and Heterogeneous Silicon-Based Films - 2002*, San Francisco, USA, April 1-5, 2002, Materials Research Society Symposium Proceedings 715, p. A23.3.1 (2002).
- [42] P. A. T. T. van Veenendaal and R. E. I. Schropp, *Curr. Op. Sol. State & Mat. Sci.* **6**, 465 (2002).
- [43] M. Koshi and K. Tonokura, Extended Abstract for the 2nd International Conference on Cat-CVD (Hot-Wire CVD) Process, Denver, USA, September 10-13, 2002, p. 23. To be published in *Thin Solid Films* (2003).
- [44] A. M. Brockhoff, W. F. van der Weg and F. H. P. M. Habraken, *J. Appl. Phys.* **89**, 2993 (2001).
- [45] A. Madan, P. Rava, R. E. I. Schropp and B. van Roedern, *Appl. Surf. Sci.* **70/71**, 716 (1993).
- [46] R. E. I. Schropp, K. F. Feenstra, E. C. Molenbroek, H. Meiling and J. K. Rath, *Philos. Mag. B* **76**, 309 (1997).
- [47] C. H. M. van der Werf, A. J. Hardeman, P. A. T. T. van Veenendaal, M. K. van Veen, J. K. Rath and R. E. I. Schropp, *Thin Solid Films* **427**, 41 (2003).
- [48] M. J. van den Boogaard, *Micropores and hydrogen diffusion in hydrogenated amorphous silicon*, Ph.D. thesis, Utrecht University, The Netherlands, 1992.
- [49] J. Tauc, in *Amorphous and liquid semiconductors*, edited by J. Tauc, Plenum Press, London, 1974.
- [50] M. Vaněček, J. Kočka, A. Poruba and A. Fejfar, *J. Appl. Phys.* **78**, 6203 (1995).
- [51] K. Pierz, W. Fuhs and H. Mell, *Philos. Mag. B* **63**, 123 (1991).
- [52] E. H. C. Ullersma, *Network structure and hydrogen diffusion in amorphous silicon carbon alloys*, Ph.D. thesis, Utrecht University, The Netherlands, 1998.
- [53] W. B. Jackson, N. M. Amer, A. C. Boccara and D. Fournier, *Appl. Opt.* **20**, 1333 (1981).
- [54] H. Stiebig, F. Siebke and R. Carius, in: M. Hack, E. A. Schiff, S. Wagner, R. E. I. Schropp and A. Matsuda (Eds.), *Amorphous Silicon Technology - 1996*, San Francisco, USA, April 8-12, 1996, Materials Research Society Symposium Proceedings 420, p. 715 (1996).
- [55] D. Ritter, E. Zeldov and K. Weiser, *Appl. Phys. Lett.* **49**, 791 (1986).
- [56] I. Balberg, *Phys. Rev. B* **44**, 1628 (1991).
- [57] M. Haridim, K. Weiser and H. Mell, *Philos. Mag. B* **67**, 171 (1993).
- [58] I. Balberg and S. Z. Weisz, *Appl. Phys. Lett.* **59**, 1726 (1991).
- [59] E. Hecht and A. Zajac, *Optics*, Addison-Wesley, Reading, 1998.
- [60] M. H. Brodsky, M. Cardona and J. J. Cuomo, *Phys. Rev. B* **16**, 3556 (1997).

- [61] A. A. Langford, M. L. Fleet, B. P. Nelson, W. A. Lanford and N. Maley, *Phys. Rev. B* **45**, 13367 (1992).
- [62] R. A. Street, *Hydrogenated amorphous silicon*, Cambridge University Press, Cambridge, 1991.
- [63] C. Godet, P. Morin and P. Roca i Cabarrocas, *J. Non-Cryst. Sol.* **198-200**, 449 (1996).
- [64] E. Bhattacharya and A. H. Mahan, *Appl. Phys. Lett.* **52**, 1587 (1988).
- [65] D. Beeman, R. Tsu and M. F. Thorpe, *Phys. Ref. B* **32**, 874 (1985).
- [66] Z. Iqbal and S. Vepřek, *Journal of Physics C* **15**, 377 (1982).
- [67] B. D. Cullity, *Elements of X-ray diffraction*, Addison-Wesley, Reading, 1967.
- [68] G. E. N. Landweer, *The application of amorphous silicon in solar cells*, Ph.D. thesis, Utrecht University, The Netherlands, 1990.
- [69] H. M. Branz, *Phys. Rev. B* **59**, 5498 (1999).
- [70] P. V. Santos and W. B. Jackson, *Phys. Rev. B* **46**, 4594 (1992).
- [71] H. Meiling, *Deposition of amorphous silicon thin films and solar cells*, Ph.D. thesis, Utrecht University, 1991.
- [72] J. Thiesen, E. Iwaniczko, K. M. Jones, A. H. Mahan and R. S. Crandall, *Appl. Phys. Lett.* **75**, 992 (1999).
- [73] C. H. M. van der Werf, P. A. T. T. van Veenendaal, M. K. van Veen, A. J. Harde- man, M. Y. S. Rusche, J. K. Rath and R. E. I. Schropp, Extended Abstract for the 2nd International Conference on Cat-CVD (Hot-Wire CVD) Process, Den- ver, USA, September 10-13, 2002, p. 185. To be published in *Thin Solid Films* (2003).
- [74] A. H. Mahan, A. Mason, B. P. Nelson and A. C. Gallagher, in: R. W. Collins, H. M. Branz, S. Guha, H. Okamoto and M. Stutzmann (Eds.), *Amorphous and Heterogeneous Silicon Thin Films - 2000*, San Francisco, USA, April 24- 28, 2000, Materials Research Society Symposium Proceedings 609, p. A6.6.1 (2000).
- [75] D. Levi, B. P. Nelson and R. Reedy, Extended Abstract for the 2nd International Conference on Cat-CVD (Hot-Wire CVD) Process, Denver, USA, September 10-13, 2002, p. 29. To be published in *Thin Solid Films* (2003).
- [76] C. Kittel and H. Kroemer, *Thermal physics*, W. H. Freeman and Company, New York, 1995.
- [77] E. A. G. Hamers, A. Fontcuberta i Morral, C. Niikura, R. Brenot and P. Roca i Cabarrocas, *J. Appl. Phys.* **88**, 3674 (2000).
- [78] E. C. Molenbroek, A. H. Mahan and A. Gallagher, *J. Appl. Phys.* **82**, 1909 (1997).
- [79] S. Guha, J. Yang, S. J. Jones, Y. Chen and D. L. Williamson, *Appl. Phys. Lett.* **61**, 1444 (1992).
- [80] B. P. Nelson, E. Iwaniczko, R. E. I. Schropp and A. H. Mahan, in: R. Hill, W. Palz and P. Helm (Eds.), *Proceedings of the 12th European Photovoltaic Solar Energy Conference*, Amsterdam, The Netherlands, April 11-15, 1994, p. 679.

- [81] S. Bauer, B. Schröder, W. Herbst and M. Lill, in: J. Schmid, H. A. Ossenbrink, P. Helm, H. Ehmann and E.D. Dunlop (Eds.), Proceedings of the 2nd World Conference on Photovoltaic Solar Energy Conversion, Vienna, Austria, July 6-10, 1998, p. 363.
- [82] K. F. Feenstra, J. K. Rath, C. H. M. van der Werf, Z. Hartman and R. E. I. Schropp, in: J. Schmid, H. A. Ossenbrink, P. Helm, H. Ehmann and E. D. Dunlop (Eds.), Proceedings of the 2nd World Conference on Photovoltaic Solar Energy Conversion, Vienna, Austria, July 6-10, 1998, p. 956.
- [83] G. E. N. Landweer, C. H. M. van der Werf, R. W. Stok, J. W. Metselaar and R. E. I. Schropp, in: R. Hill, W. Palz and P. Helm (Eds.), Proceedings of the 12th European Photovoltaic Solar Energy Conference, Amsterdam, The Netherlands, April 11-15, 1994, p. 1284.
- [84] J. K. Rath and R. E. I. Schropp, Sol. Energy Mat. and Sol. Cells **53**, 189 (1998).
- [85] F. A. Rubinelli, J. K. Rath and R. E. I. Schropp, J. Appl. Phys. **89**, 4010 (2001).
- [86] R. E. I. Schropp, J. Daey Ouwens, G. E. N. Landweer, M. B. von der Linden and C. H. M. van der Werf, in: R. Hill, W. Palz and P. Helm (Eds.), Proceedings of the 12th European Photovoltaic Solar Energy Conference, Amsterdam, The Netherlands, April 11-15, 1994, p. 699.
- [87] R. E. I. Schropp, Thin Solid Films **403-404**, 17 (2002).
- [88] A. Masuda and H. Matsumura, Thin Solid Films **395**, 112 (2001).
- [89] M. K. van Veen and R. E. I. Schropp, J. Appl. Phys. **93**, 121 (2003). See also chapters 3 and 4.
- [90] S. Morrison and A. Madan, J. Vac. Sci. Technol. A **19**, 2817 (2001).
- [91] P. A. T. T. van Veenendaal, *Hot-wire chemical vapor deposition of polycrystalline silicon*, Ph.D. thesis, Utrecht University, The Netherlands, 2002.
- [92] C. Kirk, Phys. Rev. B **38**, 1255 (1988).
- [93] P. John, I. Odeh, M. Thomas, M. Tricker and J. Wilson, Phys. Stat. Sol. B **105**, 499 (1981).
- [94] E. Bardet, J. E. Bourée, M. Cuniot, J. Dixmier, P. Elkaim, J. Le Duigou, A. R. Middy and J. Perrin, J. Non-Cryst. Sol. **198-200**, 867 (1996).
- [95] R. W. Collins and A. S. Ferlauto, Curr. Op. Sol. State & Mat. Sci. **6**, 425 (2002).
- [96] D. Soler, M. Fonrodona, C. Voz, J. M. Asensi, J. Bertomeu and J. Andreu, Extended Abstract for the 2nd International Conference on Cat-CVD (Hot-Wire CVD) Process, Denver, USA, September 10-13, 2002, p. 211. To be published in Thin Solid Films (2003).
- [97] J. Bailat, E. Vallat-Sauvain, L. Feitknecht, C. Droz and A. Shah, J. Non-Cryst. Sol. **299-302**, 1219 (2002).
- [98] S. Klein, J. Wolff, F. Finger, R. Carius, H. Wagner and M. Stutzmann, Jpn. J. Appl. Phys. **41**, L10 (2002).

- [99] R. E. I. Schropp, Y. Xu, G. A. Zaharias and A. H. Mahan, in: J. D. Cohen, J. R. Abelson, H. Matsumura and J. Robertson (Eds.), *Amorphous and Heterogeneous Silicon-Based Films - 2002*, San Francisco, USA, April 1-5, 2002, Materials Research Society Symposium Proceedings 715, p. A26.3.1 (2002).
- [100] S. Klein, F. Finger, R. Carius, O. Kluth, L. Baia Neto, H. Wagner and M. Stutzmann, in: B. McNelis, W. Palz, H. A. Ossenbrink and P. Helm (Eds.), *Proceedings of the 17th European Photovoltaic Solar Energy Conference*, Munich, Germany, October 22-26, 2001, p. 2965.
- [101] J. E. Bourée, C. Niikura, Y. Poissant and J. P. Kleider, in: B. McNelis, W. Palz, H. A. Ossenbrink and P. Helm (Eds.), *Proceedings of the 17th European Photovoltaic Solar Energy Conference*, Munich, Germany, October 22-26, 2001, p. 2857.
- [102] M. Fonrodona, A. Gordijn, M. K. van Veen, C. H. M. van der Werf, J. Bertomeu, J. Andreu and R. E. I. Schropp, Extended Abstract for the 2nd International Conference on Cat-CVD (Hot-Wire CVD) Process, Denver, USA, September 10-13, 2002, p. 181. To be published in *Thin Solid Films* (2003).
- [103] A. Ledermann, U. Weber, C. Mukherjee and B. Schröder, *Thin Solid Films* **395**, 61 (2001).
- [104] J. H. Zhou, K. Ikuta, T. Yasuda, T. Umeda, S. Yamasaki and K. Tanaka, *J. Non-Cryst. Sol.* **227-230**, 857 (1998).
- [105] J. K. Rath, F. D. Tichelaar, H. Meiling and R. E. I. Schropp, in: R. E. I. Schropp, H. M. Branz, M. Hack, I. Shimizu and S. Wagner (Eds.), *Amorphous and Microcrystalline Silicon Technology - 1998*, San Francisco, USA, April 14-17, 1998, Materials Research Society Symposium Proceedings 507 (1998), p. 879.
- [106] J. Meier, S. Dubail, R. Flückiger, D. Fischer, H. Keppner and A. Shah, *Proceedings of the IEEE First World Conference on Photovoltaic Energy Conversion*, Waikoloa, USA, December 5-9, 1994, p. 409.
- [107] B. Rech, T. Roschek, J. Müller, S. Wieder and H. Wagner, *Sol. Energy Mat. and Sol. Cells* **66**, 267 (2001).
- [108] J. Meier, S. Dubail, S. Golay, U. Kroll, S. Fay, E. Vallat-Sauvain, L. Feitknecht, J. Dubail and A. Shah, *Sol. Energy Mat. and Sol. Cells* **74**, 457 (2002).
- [109] A. R. Middy, J. Guillet, J. Perrin, A. Lloret and J. E. Bourée, in: W. Freiesleben, W. Palz, H. A. Ossenbrink and P. Helm (Eds.), *Proceedings of the 13th European Photovoltaic Solar Energy Conference*, Nice, France, October 23-27, 1995, p. 1704.
- [110] M. K. van Veen, C. H. M. van der Werf, J. K. Rath and R. E. I. Schropp, Extended Abstract for the 2nd International Conference on Cat-CVD (Hot-Wire CVD) Process, Denver, USA, September 10-13, 2002, p. 71. To be published in *Thin Solid Films* (2003). See also chapter 6.

-
- [111] P. A. T. T. van Veenendaal, J. K. Rath and R. E. I. Schropp, in: H. Scheer, B. McNelis, W. Palz, H. A. Ossenbrink and P. Helm (Eds.), Proceedings of the 16th European Photovoltaic Solar Energy Conference, Glasgow, United Kingdom, May 1-5, 2000, p. 458.
- [112] D. L. King, B. R. Hansen, J. M. Moore and D. J. Aiken, Proceedings of the 28th IEEE Photovoltaic Specialist Conference, Anchorage, USA, September 15-22, 2000, p. 1197.
- [113] R. Beckert, M. Meusel, G. Siefer, W. Warta and A. W. Bett, Technical Digest of the 12th International Photovoltaic Science and Engineering Conference, Cheju Island, Korea, June 11-15, 2001, p. 577.
- [114] J. Bruns, M. Choudhury and H. G. Wagemann, in: W. Freiesleben, W. Palz, H. A. Ossenbrink and P. Helm (Eds.), Proceedings of the 13th European Photovoltaic Solar Energy Conference, Nice, France, October 23-27, 1995, p. 230.
- [115] S. M. Sze, *Physics of semiconductor devices*, John Wiley & Sons, New York, 1981.

Summary

In this thesis, the application of the hot-wire chemical vapor deposition (HWCVD) technique for the deposition of silicon thin films is described. The HWCVD technique is based on the dissociation of silicon-containing gasses at the catalytic surface of a hot filament. Advantages of this technique compared to commonly used techniques are the high deposition rates that can be achieved, the low equipment costs, and the scalability. The main goal of this thesis is the optimization of the material properties of both hydrogenated amorphous silicon and microcrystalline silicon. As these materials have different bandgaps, they can be incorporated as the absorbing layers in single-junction and multijunction solar cells. Therefore, the material properties of both amorphous silicon and microcrystalline silicon were characterized and improved.

The thesis starts with a general introduction on thin-film materials and solar cells in chapter 1. In chapter 2, the experimental system for deposition of the layers is described, and the setups and techniques for characterization of the material and solar cell properties are described.

Chapter 3 gives an overview of the material properties of amorphous silicon, deposited using the HWCVD method. The influence of specific deposition parameters on the material quality was investigated. With the use of tantalum filaments, the deposition temperature could be decreased from 430 °C to 250 °C, while the (electronic) properties of the amorphous silicon improved and the defect density decreased. Amorphous silicon, made at a temperature of 250 °C, was attractive for application in solar cells, because of its high ambipolar diffusion length (160 nm), and high photoresponse (10^6). For this material, the deposition rate was 1.0 nm/s. However, at these low filament temperatures the silicide formation at the filaments was strongly enhanced. The presence of silicides on the filaments resulted in a decrease in the deposition rate and a deterioration of the material quality, as the nature of the created radicals was changed. For extreme silicide formation, even epitaxial growth was observed. It is likely that the changed nature of the primary radicals and the reduced deposition rate play a role in this. By preheating the filaments at elevated temperature before deposition, the influence of silicide formation could be minimized, which resulted in an improvement in the reproducibility of the material quality.

In chapter 4, the incorporation of amorphous silicon in *n-i-p* structured solar cells is described. Solar cells, in which the absorbing layer was made at a temperature of 250 °C, had high open-circuit voltages and high fill factors. The best cell had an open-circuit voltage of 0.89 V, and a fill factor of 0.72, resulting in an initial efficiency of

7.2 %. This value again indicates the device quality of hot-wire deposited amorphous silicon, deposited at moderate temperature. The solar cell efficiency can be improved further by the use of a highly reflecting back contact and by optimization of the ITO/*p*-layer front contact. The incorporation of amorphous silicon in *p-i-n* structured cells with a textured front contact resulted in a higher short-circuit current density. As a result, also the initial efficiency was higher than that of *n-i-p* structured cells. For *p-i-n* structured solar cells, care had to be taken that the deposition temperature was sufficiently low and that the hydrogen dilution during deposition was kept low.

Although the *n-i-p* structured solar cells could have high efficiencies, it turned out that the reproducibility of these results was not straightforward. Occasionally, many cells showed severe shunting problems. In chapter 5, this effect is explained. It turned out that the number of working cells was directly correlated to the age of the filaments, that were used for the deposition. The presence of silicides on the wires resulted in a deterioration of the material quality. As a result, it was possible that shunting paths were created in the material, through which current could leak. This problem could be solved in two ways. By preheating the filaments at elevated temperature before deposition, most silicon was evaporated from the filaments, and the influence of the silicides was minimized. Another method to avoid shunting paths was to incorporate a thin amorphous silicon buffer layer between the *n*-layer and the intrinsic layer. The presence of this buffer layer changed the sticking probability of adverse radicals. The nature of the deposited radicals changed, which reduced the formation of shunting paths. Filament preheating also had a beneficial effect on the quality of *p-i-n* structured solar cells.

Chapter 6 describes two materials with a narrow bandgap, namely polycrystalline silicon and microcrystalline silicon. Polycrystalline silicon is a material with a high crystalline fraction. The material consists of columnar crystals, which are oriented in the (220) direction. The material can be deposited only at high temperatures (~ 500 °C), which makes application of this material in solar cells difficult. Microcrystalline silicon has a lower crystalline fraction, and it is deposited at a substrate temperature of 250 °C. The influence of the hydrogen dilution of the silane gas on the microcrystalline silicon material properties was investigated. Crystalline growth occurred at high hydrogen dilutions. Microcrystalline layers, which were made using different hydrogen dilutions, were incorporated as the absorbing layer in *n-i-p* structured solar cells. The best cells were made with material that was deposited at the edge of the transition from the microcrystalline to the amorphous regime. The deposition rate of this material was more than 2 Å/s. The best cell had an open-circuit voltage of 0.57 V and a fill factor of 0.70, resulting in an initial efficiency of 4.8 %. However, it turned out that this material was not homogeneously structured along the growth direction, as the crystalline fraction in the material decreased with the layer thickness. This effect was caused by (small) changes in the filament properties during deposi-

tion. Microcrystalline silicon, which was made using higher hydrogen dilutions, had a homogeneous structure and is also suitable for solar cells.

As the HWCVD technique has turned out to be suitable for the deposition of device quality intrinsic silicon layers, it was investigated whether the technique could also be used for the deposition of n -doped layers. Results on hot-wire deposited microcrystalline n -layers are presented in chapter 7. For this, a special hot-wire assembly was designed, which can be inserted in the chamber that is normally used for plasma-enhanced deposition of n -type layers. The influence of the hydrogen dilution, the phosphine dilution, and the filament current on the electronic properties of the layers was investigated. The material with the highest conductivity (~ 13 S/cm) was deposited at a substrate temperature of 230 °C, using a high hydrogen dilution. The presence of the hot-wire assembly did not influence the quality of the plasma-enhanced deposited layers. Application of hot-wire deposited n -layers in $n-i-p$ structured solar cells resulted in similar open-circuit voltages, but lower short-circuit current densities compared to solar cells with a plasma-enhanced deposited n -layer. Further optimization of the hot-wire n -layers is necessary.

In chapter 8, the different intrinsic layers were incorporated in tandem solar cells. For $n-i-p/n-i-p$ structured solar cells, the open-circuit voltages were equal to the sum of the open-circuit voltages of the separate subcells. Also it was possible to obtain high fill factors. However, spectral response measurements were difficult to perform, as it turned out that the low current that is generated during these measurements easily leaked through the bottom cell. As a result, optimization of the tandem cells via spectral response measurements was impossible. Application of the hot-wire absorbing layers in $p-i-n/p-i-n$ structured tandem cells also resulted in high open-circuit voltages and fill factors. In this case, no current was lost during spectral response measurements. These results indicated that the order, in which the layers were deposited, determined the quality of the solar cells. More specifically, the order in which the p - and n -layer in the tunnel-recombination junction were deposited was crucial for the device performance. This junction needs further optimization in $n-i-p$ structured tandem solar cells. By optimizing the thicknesses of the subcells, the solar cell efficiency can be improved further. Based on the achieved efficiencies for amorphous and microcrystalline solar cells on untextured stainless steel, it should be possible to obtain efficiencies of well over 10 %.

Samenvatting

Sinds de erkenning van het bestaan van het broeikas-effect is de aandacht voor duurzame energiebronnen sterk toegenomen. Het voornaamste kenmerk van deze energiebronnen is dat ze in nagenoeg ongelimiteerde hoeveelheden aanwezig zijn, en dat er geen broeikasgassen vrijkomen bij het gebruik ervan. Voorbeelden van duurzame energie zijn windenergie, hydrodynamische energie en zonne-energie. Met name zonne-energie is een serieuze kandidaat om op grote schaal gebruikt te worden, maar op het moment zijn de toepassingen beperkt vanwege de hoge kosten. De omzetting van zonne-energie in elektrische energie gebeurt met behulp van zonnecellen. Het principe van deze energie-omzetting is gebaseerd op het fotovoltaïsche (PV) effect: indien de energie van een inkomend foton groter is dan de bandafstand van een halfgeleider, dan kan een elektron vanuit de valentieband geëxciteerd worden naar de geleidingsband. Hierbij blijft er een gat achter in de valentieband. Aldus worden ladingsdragers gecreëerd, die in een extern circuit gecollecteerd kunnen worden, zodat de elektrische energie gebruikt kan worden.

Op het moment is (multi)kristallijn silicium het meest gebruikte materiaal om zonnecellen van te maken. Met dit materiaal is het mogelijk gebleken om in het laboratorium een energie-omzettingsrendement van bijna 25 % te halen. Een groot nadeel van (multi)kristallijn silicium is echter de lage lichtabsorptie. Om veel zonlicht te kunnen absorberen zijn dikke lagen nodig, waardoor de materiaalkosten van dit type zonnecel hoog zijn. Als alternatief wordt de laatste tijd dan ook veel onderzoek gedaan aan dunne-film zonnecellen, die gemaakt worden door middel van depositie op een substraat. De productiekosten van dunne-film zonnecellen zijn lager dan die van (multi)kristallijne cellen, maar over het algemeen is ook de efficiëntie lager. Typische dunne-film materialen zijn cadmiumtelluride, koperindiumdiselenide en dunne-film silicium. Van deze materialen krijgt silicium de meeste aandacht, vanwege het feit dat het veelvoorkomend en niet giftig is. Door de depositie-omstandigheden van dunne-film silicium aan te passen, kunnen materialen gemaakt worden, waarvan de orde of kristalliniteit verschilt. Deze materialen worden aangeduid als amorf silicium, microkristallijn silicium of polykristallijn silicium, afhankelijk van de kristallijne fractie in het materiaal.

Dunne-film zonnecellen van silicium bestaan uit een aantal lagen, waarvan de intrinsieke of absorberende laag de belangrijkste is. In deze laag wordt het zonlicht geabsorbeerd en worden ladingsdragers gecreëerd. Aan weerszijden van deze intrinsieke laag zijn dunne *n*-type of *p*-type lagen aangebracht, die tezamen een elektrisch veld over de cel genereren. Nadat de ladingsdragers van elkaar zijn gescheiden, worden ze onder invloed van dit elektrische veld getransporteerd en in de contacten van

de zonnecel gecollecteerd. De totale lichtabsorptie in de zonnecel wordt grotendeels bepaald door de bandafstand van de gebruikte materialen. Voor amorf silicium is de bandafstand ongeveer 1.8 eV. Dit houdt in dat licht met een energie lager dan 1.8 eV niet wordt geabsorbeerd in een zonnecel van amorf silicium en dus verloren gaat. Dit verlies kan verkleind worden door het stapelen van meerdere zonnecellen, waarin de bandafstand van de verschillende subcellen varieert. Het licht dat door de eerste cel niet wordt geabsorbeerd kan dan alsnog geabsorbeerd worden door de onderliggende cel(len). Hierdoor wordt een groter gedeelte van het zonnespectrum benut, wat resulteert in een hoger energie-conversierendement. Deze stapelcellen worden tandem-zonnecellen genoemd, indien twee cellen gestapeld zijn, en triple-zonnecellen, indien drie cellen gestapeld zijn.

De meest gebruikte methode om dunne-film materialen en zonnecellen te deponeren is via chemische damp-depositie vanuit een plasma ("PECVD"). Hierbij wordt een siliciumhoudend gas (meestal silaan, SiH_4) ontleed in een radiofrequent plasma. De reactieproducten worden gedeponerd op een substraat, waar de laag gevormd wordt. Een nadeel van deze depositietechniek is de lage groeisnelheid. Een alternatieve depositiemethode is de zogenaamde "Hot-Wire Chemical Vapor Deposition"- of "HWCVD"-techniek, waarbij een siliciumhoudend gas katalytisch ontleed wordt aan een hete draad. Grote voordelen van deze techniek zijn de hoge depositiesnelheden die gehaald kunnen worden, de lage kosten voor depositie-apparatuur, en de opschaalbaarheid. Nog onopgeloste kwesties zijn de controle van de substraattemperatuur tijdens depositie en het verouderen van de draden.

Dit proefschrift beschrijft de (voortgaande) ontwikkeling van zowel amorf silicium als microkristallijn silicium met behulp van de HWCVD-techniek, met als doel de toepassing in tandemzonnecellen. Hiervoor werden eerst de materiaaleigenschappen gekarakteriseerd en verbeterd. Het proefschrift begint dan ook, na een algemene inleiding in hoofdstuk 1, met een algemene beschrijving in hoofdstuk 2 van het depositiesysteem waarin de lagen gemaakt werden. Ook worden in dit hoofdstuk de experimentele opstellingen en technieken beschreven waarmee de lagen gekarakteriseerd werden.

Hoofdstuk 3 geeft een overzicht van de materiaaleigenschappen van amorf silicium, dat gemaakt is met de HWCVD-methode. De invloed van verschillende depositie-omstandigheden op de kwaliteit van het materiaal zijn onderzocht. Met het gebruik van tantaaldraden kan de depositietemperatuur verlaagd worden van 430 °C naar 250 °C, terwijl de (elektrische) eigenschappen van het amorf silicium verbeteren en de defectdichtheid omlaag gaat. Amorf silicium, dat gemaakt is bij 250 °C, is aantrekkelijk voor toepassing in zonnecellen vanwege de hoge ambipolaire diffusielengte (160 nm), en de hoge fotorespons (10^6). De depositiesnelheid van dit materiaal is 1.0 nm/s. Bij deze lage draadtemperaturen wordt silicidevorming aan de draad echter versterkt. De aanwezigheid van siliciden op de draad resulteert uiteindelijk

in een verlaging van de depositiesnelheid en in een verslechtering van het materiaal, aangezien de aard van de gecreëerde radicalen verandert. Bij zeer vergaande silicidatie is epitaxiale groei waargenomen. De veranderde samenstelling van primaire radicalen en de verlaagde depositiesnelheid spelen hierbij een rol. Door de draden op hoge temperatuur uit te stoken voor de depositie, kan de invloed van siliciden op de draad geminimaliseerd worden en kunnen lagen reproduceerbaar worden gedeponeerd.

In hoofdstuk 4 wordt de toepassing van amorf silicium in zonnecellen beschreven. Hiervoor wordt de *n-i-p*-structuur gebruikt, waarin eerst de *n*-laag wordt gedeponeerd, gevolgd door de intrinsieke (*i*-) en de *p*-laag. Het voordeel van deze depositievolgorde is dat de *n*-laag minder gevoelig is voor hoge temperaturen dan de *p*-laag. Bij depositie in de omgekeerde volgorde (*p-i-n*-structuur) treedt namelijk vaak het probleem op dat de *p*-laag en/of de onderliggende transparante geleider worden aangetast, waardoor de efficiëntie van de zonnecellen negatief beïnvloed wordt. Flexibel roestvrij staal is gebruikt als substraat van de *n-i-p*-zonnecellen. Cellen, waarin de intrinsieke laag gemaakt is bij 250 °C, hebben een hoge open-klemspanning en een hoge vulfactor. De beste cel heeft een open-klemspanning van 0.89 V en een vulfactor van 0.72, wat resulteert in een initieel energie-conversierendement van 7.2 %. Deze efficiëntie is een verbetering van de waarde die voorheen bij hoge depositietemperatuur werd bereikt, waarmee opnieuw de kwaliteit van het amorf silicium, gemaakt bij 250 °C, is aangetoond. Dit rendement kan verder verbeterd worden door het gebruik van een getextureerde reflecterende laag aan het achtercontact en door optimalisatie van het voorcontact, waar het licht de cel binnenkomt. Toepassing van amorf silicium in *p-i-n*-cellen met getextureerd voorcontact resulteert in een hogere kortsluitstroom, waardoor het initieel rendement van deze cellen hoger is dan dat van *n-i-p*-gestructureerde cellen. Voor dit type cel is het echter van cruciaal belang dat de depositietemperatuur niet te hoog is en dat de waterstofverdunding tijdens depositie laag is.

Alhoewel de *n-i-p*-gestructureerde cellen een hoog rendement kunnen hebben, blijkt dat de reproduceerbaarheid van dit resultaat niet eenvoudig was. Af en toe bleken veel zonnecellen een lage parallelweerstand te hebben, waardoor stroom wegleekt. In hoofdstuk 5 wordt dit gedrag verklaard. Het blijkt dat het aantal werkende cellen direct gerelateerd is aan de ouderdom van de draden, die tijdens de depositie gebruikt zijn. Silicidvorming op de draden heeft tot gevolg dat de kwaliteit van de gedeponeerde laag achteruitgaat. Hierdoor kunnen paden in het materiaal ontstaan, waardoor stroom kan weglekken. Dit probleem is op twee manieren te voorkomen. Door de draden voor de depositie op hoge temperatuur uit te stoken, wordt het meeste silicium van de draden verdampt, zodat dit geen invloed meer heeft op de kwaliteit van het materiaal. Een andere methode om een lage parallelweerstand te voorkomen is het aanbrengen van een dunne bufferlaag tussen de *n*-laag en de intrinsieke laag.

Deze bufferlaag zorgt voor een vermindering in de waarschijnlijkheid, dat radicalen aan het siliciumoppervlak blijven plakken. Hierdoor verandert het soort radicalen dat bijdraagt aan de groei, wat de vorming van lekpaden vermindert. Ook op de kwaliteit van *p-i-n*-gestructureerde cellen heeft het uitstoken van de draden een positief effect.

Hoofdstuk 6 beschrijft twee materialen met een kleine bandafstand, namelijk polykristallijn en microkristallijn silicium. Polykristallijn silicium is een materiaal met een grote kristallijne fractie, waarbij de kristallen in de (220)-richting gegroeid zijn. Het materiaal kan echter alleen bij hoge temperaturen (~ 500 °C) gedeponeerd worden, waardoor het gebruik in een aantal toepassingen moeilijk is. Microkristallijn silicium heeft een lagere kristallijne fractie dan polykristallijn silicium en wordt gedeponeerd bij een temperatuur van 250 °C. De invloed van de verdunning van silaan met waterstof op de materiaaleigenschappen is onderzocht. Het blijkt dat microkristallijne groei optreedt bij hoge waterstofverduunningen, en dat de kristalletjes in het materiaal willekeurig georiënteerd zijn. Microkristallijne siliciumlagen, die gemaakt zijn bij verschillende waterstofverduunningen, zijn toegepast in *n-i-p*-gestructureerde zonnecellen op roestvrij staal. De beste cellen zijn gemaakt met materiaal dat gedeponeerd is met een waterstofverduunning dicht bij de overgang van het microkristallijne naar het amorphe regime. De groeisnelheid van dit materiaal is meer dan 2 Å/s. De beste cel heeft een open-klemspanning van 0.57 V, en een vulfactor van 0.70, wat resulteert in een initieel rendement van 4.8 %. Uit diverse metingen blijkt echter dat dit materiaal niet homogeen gestructureerd is in de groeirichting, aangezien de kristallijne fractie in het materiaal afneemt met toenemende dikte. Dit effect wordt veroorzaakt door (kleine) veranderingen in de draadeigenschappen tijdens de depositie. Materiaal dat gemaakt is met een hogere waterstofverduunning is wel homogeen van structuur en ook geschikt voor toepassing in zonnecellen.

Nadat gebleken is dat de HWCVD-techniek uitstekend geschikt is voor het deponeren van intrinsieke siliciumlagen, is in hoofdstuk 7 onderzocht of de techniek ook gebruikt kan worden voor de depositie van *n*-type lagen. Hiervoor is een speciale draadhouder ontworpen, die in een depositiekamer geplaatst kan worden waarin normaal gesproken plasmadepositie plaatsvindt. De invloed van de waterstof- en fosfineverduunning, en van de draadstroom op de elektrische eigenschappen van de *n*-lagen is onderzocht. Het materiaal met het hoogste geleidingsvermogen (~ 13 S/cm) wordt gedeponeerd bij een temperatuur van 230 °C en een hoge waterstofverduunning. De aanwezigheid van de draden in de plasma-depositiekamer heeft weinig invloed op de kwaliteit van de plasma-gedeponeerde lagen. Toepassing van de HWCVD-gedeponeerde *n*-lagen in zonnecellen resulteerde in vergelijkbare waarden voor de open-klemspanning, maar lagere waarden voor de kortsluitstroom ten opzichte van cellen met een plasma-gedeponeerde *n*-laag. Verdere optimalisatie van de *n*-lagen is nodig.

In hoofdstuk 8 worden verschillende intrinsieke lagen toegepast in tandemzon-

necellen. Indien de $n-i-p/n-i-p$ -structuur gebruikt wordt, blijkt dat de cellen hoge open-klemspanningen hebben, waarvan de waarde ongeveer gelijk is aan de som van de open-klemspanningen van de subcellen. Ook is het mogelijk hoge vulfactoren te verkrijgen. Spectrale responsmetingen zijn echter niet eenvoudig uit te voeren, omdat de lage stroom die bij de gebruikte lage lichtintensiteiten wordt gegenereerd makkelijk blijkt weg te lekken. Optimalisatie van de tandemcellen via spectrale responsmetingen wordt hierdoor onmogelijk gemaakt. Toepassing van de HWCVD-lagen in $p-i-n/p-i-n$ -gestructureerde cellen resulteert ook in hoge open-klemspanningen en vulfactoren. In dit geval lekt er echter geen stroom weg door een van de cellen. Dit resultaat geeft aan dat de volgorde van de depositie van belang is voor de kwaliteit van de cel. In het bijzonder blijkt dat de volgorde, waarin de p - en n -lagen van de tunnel-recombinatieverbinding worden gedeponerd, van belang is en dat deze verbinding verdere optimalisatie behoeft in $n-i-p$ -gestructureerde tandemzonnecellen. Door ook de diktes van de subcellen te optimaliseren is het, op grond van de behaalde resultaten voor microkristallijne en amorfe zonnecellen op slecht reflecterend roestvrij staal, mogelijk om rendementen van ruim boven de 10 % te halen.

List of publications

Publications related to this thesis:

M. K. van Veen, C. H. M. van der Werf, J. K. Rath and R. E. I. Schropp, *Incorporation of amorphous and microcrystalline silicon in n-i-p solar cells*, accepted for publication in Thin Solid Films (2003).

M. Fonrodona, A. Gordijn, M. K. van Veen, C. H. M. van der Werf, J. Bertomeu, J. Andreu and R. E. I. Schropp, *Shutterless deposition of phosphorous doped microcrystalline silicon by Cat-CVD*, accepted for publication in Thin Solid Films (2003).

C. H. M. van der Werf, P. A. T. T. Van Veenendaal, M. K. van Veen, A. J. Hardeman, M. Y. S. Rusche, J. K. Rath and R. E. I. Schropp, *The influence of the filament temperature on the structure of hot-wire deposited silicon*, accepted for publication in Thin Solid Films (2003).

C. H. M. van der Werf, A. J. Hardeman, P. A. T. T. van Veenendaal, M. K. van Veen, J. K. Rath and R. E. I. Schropp, *Investigation of scaling-up issues in hot wire CVD of microcrystalline silicon*, Thin Solid Films **427**, 41 (2003).

M. K. van Veen and R. E. I. Schropp, *Understanding shunting behavior in Hot-Wire deposited amorphous silicon solar cells*, Applied Physics Letters **82**, 287 (2003).

M. K. van Veen and R. E. I. Schropp, *Beneficial effect of a low deposition temperature of hot-wire deposited intrinsic amorphous silicon for solar cells*, Journal of Applied Physics **93**, 121 (2003).

M. K. van Veen, P. A. T. T. van Veenendaal, C. H. M. van der Werf, J. K. Rath and R. E. I. Schropp, *a-Si:H/poly-Si tandem cells deposited by hot-wire CVD*, Journal of Non-Crystalline Solids **299-302**, 1194 (2002).

Marieke K. van Veen and Ruud E. I. Schropp, *Amorphous silicon deposited by hot-wire CVD for application in dual junction solar cells*, Thin Solid Films **403-404**, 135 (2002).

R. E. I. Schropp, C. H. M. van der Werf, M. K. van Veen, P. A. T. T. van Veenendaal, R. Jimenez Zambrano, Z. Hartman, J. Löffler and J. K. Rath, *Thin film a-Si/poly-Si multibandgap tandem solar cells with both absorber layers deposited by hot wire*

CVD, in: M. Stutzmann, J. B. Boyce, J. D. Cohen, R. W. Collins and J. Hanna (Eds.), *Amorphous and Heterogeneous Silicon-Based Films - 2001*, San Francisco, USA, April 16-20, 2001, Materials Research Society Symposium Proceedings **664**, p. A15.6.1 (2001).

Marieke K. van Veen and Ruud E. I. Schropp, *Higher efficiency of n-i-p solar cells by hot-wire CVD at moderate temperatures*, in: M. Stutzmann, J. B. Boyce, J. D. Cohen, R. W. Collins and J. Hanna (Eds.), *Amorphous and Heterogeneous Silicon-Based Films - 2001*, San Francisco, USA, April 16-20, 2001, Materials Research Society Symposium Proceedings **664**, p. A11.2.1 (2001).

J. K. Rath, B. Stannowski, P. A. T. T. van Veenendaal, M. K. van Veen and R. E. I. Schropp, *Application of hot-wire chemical vapor-deposited Si:H films in thin film transistors and solar cells*, Thin Solid Films **395**, 320 (2001).

Other publications:

Jaap van der Weerd, Marieke K. van Veen, Ron M. A. Heeren and Jaap J. Boon, *Identification of pigments in paint cross sections by reflection visible light imaging microspectroscopy*, Analytical Chemistry **75**, 716-722 (2003).

B. Stannowski, M. K. van Veen and R. E. I. Schropp, *Towards an all-hot-wire TFT: silicon nitride and amorphous silicon deposited by hot-wire chemical vapor deposition*, in: M. Stutzmann, J. B. Boyce, J. D. Cohen, R. W. Collins and J. Hanna (Eds.), *Amorphous and Heterogeneous Silicon-Based Films - 2001*, San Francisco, USA, April 16-20, 2001, Materials Research Society Symposium Proceedings **664**, p. A17.3.1 (2001).

Dankwoord

Met het verschijnen van dit proefschrift komt er een einde aan een onderzoeksperiode van vier jaar, een periode die ik (meestal) als zeer plezierig en leerzaam heb ervaren. En alhoewel dit proefschrift maar één auteursnaam telt, zijn er vele mensen die hebben meegeholpen met het totstandkomen ervan. Bij deze wil ik graag een aantal mensen voor hun bijdrage bedanken.

Als eerste natuurlijk mijn promotor Ruud Schropp. De afgelopen vier jaar heb ik veel vrijheid gehad om mijn onderzoek in te richten, maar bij Ruud kon ik altijd terecht voor vragen, ideeën en wetenschappelijke discussies. De discussies met Jatin Rath gaven vaak een andere kijk op de verkregen resultaten, wat meestal leidde tot een beter inzicht in de fysische processen. Frans Habraken, Jaap Dijkhuis (Debye Instituut) en Wim Sinke (ECN) dank ik voor het kritisch lezen van mijn manuscript. I would like to thank Harv Mahan (NREL, Golden, Co) for the critical reading of my manuscript. De Nederlandse Organisatie voor Energie en Milieu (NOVEM) wil ik bedanken voor de financiële steun.

Zonder samples zou dit proefschrift erg dun zijn geworden. Karine van der Werf dank ik dan ook voor het deponeren van ongeveer 250 (!) siliciumlagen en zonnecellen. Ik zal maar niet uitrekenen hoeveel tijd daarvoor in totaal nodig was... Gelukkig hebben de meeste samples dit proefschrift wel gehaald! Jeroen Francke bedank ik voor het deponeren van een aantal siliciumlagen in de ASTER. Gert Hartman, Jochen Löffler, Raul Jimenez Zambrano en Mariëlle Rusche hebben een groot gedeelte van de ITO-deposities voor hun rekening genomen.

Soms hadden ook de meetopstellingen hun dag niet. In zo'n geval stonden Ruurd Lof, Wim de Kruif, Juriaan Adams en Bert Slomp paraat om het hele zaakje weer aan de gang te krijgen of om de optische opstellingen opnieuw uit te lijnen. Dirk Knoesen (University of the Western Cape, ZA) heeft vele X-TEM- en SEM-foto's gemaakt, die vaak zeer onverwachte resultaten gaven. Margot Snel (Debye Instituut) bedank ik voor de AFM-metingen aan de metalen substraten.

De samenwerking met Patrick van Veenendaal was altijd erg gezellig. Helaas zijn de polykristallijne lagen nooit echt verbeterd, maar dat heeft wel tot vele gegevens over microkristallijn silicium geleid. Marta Fonrodona (University of Barcelona) started the work on hot-wire deposited *n*-doped layers. I would like to thank her for performing XRD and Raman measurements on these samples. Wim Arnold Bik heeft geholpen met ERD-metingen. Monica Brinza and Guy Adriaenssens (KU Leuven) performed time-of-flight measurements on the hot-wire deposited amorphous silicon layers. Robert Stolk verschaftte de resultaten van de HWCVD-gedeponeerde triple-zonnecel. Ik heb er alle vertrouwen in dat er in de toekomst betere resultaten aan triple-zonnecellen zullen volgen!

Een onderdeel van het aio-schap is natuurlijk het geven van onderwijs. Joost van Hoof, Gijs Bardelmeijer en Wim Westerveld wil ik bedanken voor de goede samenwerking bij het begeleiden van de natuurkundepractica. Daarnaast ben ik ook een tijd lid geweest van de Debye aio-commissie. Graag wil ik alle co-organisatoren van de Debye Winterschool 2002 (Frans Habraken, Peter van der Straten, Bert Weckhuysen en Arnout Imhof) en van de DO!-dagen 2001 (Gijsje Koenderink, Jeroen Bakker, Harm Dijkstra en Anne Arink), en natuurlijk ook alle (oud-)DAC-leden bedanken voor de goede en gezellige samenwerking.

Bij Riny de Haas kan iedereen altijd binnenlopen voor een gezellig praatje en drop. Verder wil ik iedereen bedanken voor de (wetenschappelijke) discussies en gezelligheid tijdens diverse conferenties, workshops en een zomerschool in Seč, Barcelona, San Francisco, Nice, Salerno en Denver. Mijn (oud-)kamergenoten Bernd Stannowski, Ronald Franken, Marta Fonrodona, Robert Stolk en Paula Bronsveld dank ik voor de gezellige tijd. Verder wil ik natuurlijk ook alle andere (oud-)collega's bedanken voor de goede samenwerking en plezierige werksfeer.

Natuurlijk zijn er ook een aantal mensen buiten de natuurkunde die ik wil bedanken voor het brengen van de nodige ontspanning. De klaverjasavonden met Martina en Vera zijn altijd erg gezellig en, ondanks het morele verlies, altijd voor herhaling vatbaar. Ook met Petra en Detlef is het goed spelletjes spelen. Helaas zal dat de komende tijd waarschijnlijk wat minder vaak worden, maar wie weet? Mijn ouders en familie wil ik bedanken voor hun steun en interesse in mijn onderzoek. Tot slot wil ik Freek bedanken voor alle steun en liefde. Samen gaan we vast een gezellige tijd in Zwitserland tegemoet!

Curriculum vitae

De schrijfster van dit proefschrift werd geboren op 25 augustus 1976 te Vught. In 1994 haalde zij haar diploma aan het Gymnasium Beekvliet te Sint-Michielsgestel. In september van hetzelfde jaar begon ze met de studie natuurkunde aan de Universiteit Utrecht. Tijdens haar studie volgde ze keuzevakken op het gebied van materiaalfysica, vaste-stoffysica en fysische informatica en deed ze een klein onderzoek bij de groep grenslaagfysica. Het afstudeeronderzoek werd uitgevoerd aan het FOM-instituut voor Atoom- en Molecuulfysica te Amsterdam bij de groep Macromoleculen. De eindschrift had als titel "A new setup for spectral imaging with visible light of embedded paint cross-sections". Het doctoraalexamen werd in april 1999 afgelegd (met genoegen).

Per 1 juni 1999 trad zij in dienst als assistent in opleiding (aio) bij het programma Surfaces, Interfaces and Devices binnen het Debye Instituut van de Universiteit Utrecht. De resultaten van het verrichte onderzoek staan beschreven in dit proefschrift en werden op diverse internationale conferenties gepresenteerd. Tijdens de promotieperiode begeleidde ze practica voor eerste- en tweedejaars natuurkundestudenten. Tevens was zij tijdens haar promotieperiode actief binnen het Debye Instituut, onder meer als secretaris van de aio-commissie.